Numerical modelling of hydrodynamic and solute transport processes in shallow water environment

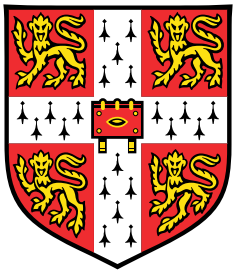

Fan YANG

University of Cambridge

This thesis is submitted for the degree of

Doctor of Philosophy

Churchill College September 2020

Declaration

I hereby declare that

- this dissertation is the results of my own work and includes nothing which is the outcome of work done in collaboration except as declared in the Preface and specified in the text;
- this dissertation is not substantially the same as any that I have submitted, or, is being concurrently submitted for a degree or diploma or other qualification at the University of Cambridge or any other University or similar institution except as declared in the Preface and specified in the text. I further state that no substantial part of my dissertation has already been submitted, or, is being concurrently submitted for any such degree, diploma or other qualification at the University of Cambridge or any other University or similar institution except as declared in the Preface and specified in the text;
- this dissertation contains fewer than 65,000 words including appendices, bibliography, footnotes, tables and equations and has fewer than 150 figures, and therefore, it does not exceed the prescribed word limit.

Fan YANG

September 2020

Numerical modelling of hydrodynamic and solute transport processes in shallow water environment

Fan Yang

Abstract

This thesis studies the numerical modelling of a range of hydrodynamic, solute transport and biochemical reaction processes in shallow water environment, combining both Euler and Lagrangian techniques. The research consists of two parts: the rapid flow modelling and the solute transport modelling.

In the rapid flow modelling, the research is focused on demonstrating the impact of modifying the Boussinesq coefficient when simulating rapid flows in various situations. The traditional Alternating Direction Implicit (ADI) scheme has been proven to be incapable of modelling trans-critical flows. Its inherent lack of shock-capturing capability results in spurious oscillations and computational instabilities. However, the ADI scheme is still widely adopted in flood modelling software, and various special treatments have been designed to stabilise the computation. Modification of the Boussinesq coefficient to adjust the amount of fluid inertia is a numerical treatment that allows the ADI scheme to be applicable to rapid flows. A comprehensive study has been undertaken to examine the impact of this numerical treatment over a range of flow conditions. A shock-capturing TVD-MacCormack model is used to provide reference results.

In the solute transport modelling, a mesh-free, depth-averaged and highly robust random walk model has been developed for simulating the two-dimensional solute transport processes. The development of the random model consists of two stages. In the first stage, extensive parametric studies have been undertaken to investigate the influences of the number of particles, the size of time steps and the technique of sampling processes used in the random walk model. The model is then applied to investigate the solute oscillation along a tidal estuary subject to extensive wetting and drying during tidal oscillations. The flow velocities are interpolated from the grid-based TVD-MacCormack flow solver. Finally, the model is applied to investigate wind-induced chaotic mixing in a circular shallow basin. The effect of diffusive processes on the chaotic mixing is investigated. The results of the first stage research provide a guideline for properly presenting the outputs of the random walk method for scientific analyses. In the second stage, the random-walk model is further developed to investigate the advection, diffusion and reaction processes of non-conservative materials. First, several classical test cases are presented to showcase the capability of the random walk model in addressing the problem of continuous release of non-conservative

substances. Then, the method is applied to model the BOD-DO balance along a hypothetical river. The numerical results are in good agreement with the analytical solution. Finally, the developed scheme is used to study the pollutant transport in Thames Estuary. The current model is illustrated to be able to accurately predict the interaction between multiple pollutants in real-world situations with uneven bathymetry and extensive intertidal floodplains.

I would like to dedicate this thesis to my beloved parents.

Acknowledgement

First, I am deeply indebted to my supervisor, Dr Dongfang Liang, who has always been able to provide instrumental suggestions. This thesis would not have been possible without his tremendous support, thoughtful advice, considerable encouragement and effective supervision. Dr Liang is patient, kind and knowledgeable expert in the field of hydraulics. His vast knowledge has helped me tremendously over the past four years. I especially thank him for consistently maintaining regular meetings with me and helping me improve my academic writing, no matter how busy he is. Those help has been crucial in my study. Second, I would like to gratefully thank my advisor, Professor Allan McRobie, for his invaluable advice on my study. I also thank Dr Xuefei Wu for her kind help in answering my questions about Fortran code. In particular, I am very grateful for having the wonderful colleagues working together in the geotechnical research office and miss terribly the tea and cake moments that we use to have together. I also wish to thank all the other wonderful people that I have been working with throughout the years in Cambridge. I am extremely lucky to meet Lynn, Xuezi, Xiaoxiao, Dudu, Hao, Jun and Benshuai in Cambridge. They have made this journey enjoyable and worthwhile. Last, but in no way the least, my deepest thanks go to my loving parents, who have been constantly supporting me to pursue my dream for more than 20 years. Their constant care, love and especially understanding are the best gifts for me during my pursuing the Doctor degree.

Contents

List of Figures

List of Figures

List of Figures

Nomenclature

Roman terms

A	cross-sectional area	m^2
A_x	cross-sectional area in the x direction	m^2
Δb	minimum size of the sampling bins	m
C	Chézy roughness coefficient	$m^{1/2}/s$
D	diffusion coefficient	m^2/s
D_s	streamwise diffusion coefficient	m^2/s
D_t	transverse diffusion coefficient	m^2/s
E	relative error	1
g	gravitational acceleration	m/s^2
K	first-order rate coefficient	1/s

Nomenclature

K_a	re-oxygenation rate	1/s
K_r	deoxygenation rate	1/s
H	total water column depth	m
H_{min}	minimum water depth	m
H_{mean}	mean water depth	m
I	mass source term	m/s
M	total mass	kg
M_0	total amount of solute material at time zero	kg
$\dot{M}$	mass discharge rate	kg/s
$\dot{M}_0$	constant mass discharge rate	kg/s
m	mass assigned to each particle	kg
m_p^0	initial value of particle's mass	kg
n	Manning coefficient	$s/m^{1/3}$
N	total number of particles	1
O_s	sources term in 1-D advective-diffusion equation	kg/ms
P	number of particles	1
P_0	constant number of particles	1
Q	discharge rate	m^3/s
q_s	sources and sinks term	kg/m^2s

Nomenclature

q_x	volumetric discharge per unit width in x direction	m^2/s
q_y	volumetric discharge per unit width in y direction	m^2/s
R_0	radius of the lake	m
r_i	independent random number	1
r_s	independent random number in streamwise direction	1
r_t	independent random number in transverse direction	1
S	depth-integrated solute concentration	kg/m^2
s	depth-averaged solute concentration	kg/m^3
S_0	bed slope	1
S_f	friction slope	1
$S_{analytical}$	analytical solution	mg/l
$S_{predicted}$	predicted solution	mg/l
S_{BOD0}	original BOD concentration	mg/l
S_{DO0}	original DO concentration	mg/l
S_{DOsat}	saturated DO concentration in water	mg/l
T	time period	s
t	time	s
t_s	storm duration	s
Δt	time step	s

U	modified advective velocities along x direction	m/s
u	velocities along x direction	m/s
u_*	shear velocity	m/s
$\bar{U}$	time-averaged velocity along x direction	m/s
U_s^d	diffusion-related streamwise velocity	m/s
U_x^d	diffusion-related velocity along x direction	m/s
V	modified advective velocity along y direction	m/s
v	velocities along y direction	m/s
V_{ai}	theoretical value	m/s
V_i	ADI-predicted value	m/s
$\bar{V}$	time-averaged velocity along y direction	m/s
V_t^d	diffusion-related transverse velocity	m/s
V_y^d	diffusion-related velocity along y direction	m/s
x	Cartesian coordinate	m
y	Cartesian coordinate	m
z_0	roughness height of the bed	m
z_b	the height of bed above the datum	m

Greek terms

β	Boussinesq coefficient	1
θ	angle between x direction and local flow direction	rad
ε_s	dimensionless streamwise dispersion constant	1
ε_t	dimensionless transverse dispersion constant	1
κ	von Kármán's constant	1
μ	dimensionless storm duration parameter	1
η	water surface elevation above the datum	m
ρ	water density	kg/m^3
τ	particle release time	s
τ_w	wind shear stress	kg/ms^2
τ_{wx}	wind shear stress along x direction	kg/ms^2
τ_w	wind shear stress along y direction	kg/ms^2
ψ	stream function of the velocity field	m^2/s

Acronyms and Abbreviations

1-D	One-dimensional
2-D	Two-dimensional
ADI	Alternating Direction Implicit
BOD	Biochemical Oxygen Demand
CFL	Courant–Friedrichs–Lewy
DEM	digital elevation model
DNS	Direct Numerical Simulation
DO	Dissolved Oxygen
GIS	geographic information system
RANS	Reynolds Averaged Navier-Stokes equations
SWEs	Shallow Water Equations
TDMA	Tri-Diagonal Matrix Algorithm
TVD	Total Variation Diminishing
USEPA	US Environmental Protection Agency

Chapter 1

Introduction

1.1 Background

Water has been a vital resource to human civilization for thousands of years. However, water security has now become a major and growing challenge for both developing and developed countries. According to the World Bank (2017a), water scarcity affects more than 40% of the population across the globe. Water-related disasters account for 70% of all deaths related to natural disasters.

The situation is worsening in three aspects. First, the demand for fresh water is increasing rapidly. In many countries, growing population and extensive urbanisation during the recent decades have driven the fresh-water demand in livelihood, agricultural and industrial sectors. It is estimated that the world will face a 40% shortage between projected demand and available

water supply by 2030 according to current practices (World Bank 2017b). Second, climate change makes a great impact on hydrological cycle. Global warming is worsening, and extreme rainfall events become more and more unpredictable. The intensity and frequency of floods and droughts are seen much more frequently (see Figure 1.1 for example). It is estimated that the annual damage caused by the floods is at least $120 billion in property losses (Ivan Maddox 2014). Last not the least, aging drainage infrastructure increases the flooding risk significantly. A lot of the sewerage network is old, and its condition is unknown, making the existing drainage systems unreliable. In addition, demographic shifts and urbanisation have put a considerable strain on existing drainage systems, increasing the likelihood of them being overwhelmed. In short, chronic water scarcity, extreme weather events and hydrological uncertainty are considered as the greatest threats to global prosperity and stability.

Figure 1.1 Severe floods engulf eastern China in July 2020 (BBC, 2020)

Water security faces great challenges not only because of water shortage or flooding, but also because of deteriorating water quality. The continuous agricultural and industrial developments demand increasingly high water quality; the water quality on the other hand, is deteriorating. This is often caused by the unsupervised introduction of pollutants into water bodies, as shown in Figure 1.2. For example, sewage waste and heat in industrial and agricultural production are discharged into rivers, lakes, oceans and groundwater without adequate treatment. Part of pollutant substances in the freshwater are mixed and diluted with the water flow, and then degraded by chemical and biological interactions. The rest of the pollutants will join the hydrological circle and seriously affect water quality.

Figure 1.2 Discharge of wastewater into a reservoir (Francesca 2016)

The deteriorating water quality leads to many severe consequences. One typical consequence is eutrophication. The phenomenon of eutrophication is characterized by excessive plant and algal growth in rivers, lakes and oceans.

This is caused by the growing availability of limiting factors needed for photosynthesis (Schindler 2006), such as carbon dioxide, oxygen and nutrient fertilizers. Human activities have accelerated the speed and degree of eutrophication through both point source discharge and non-point source discharge of nutrients (such as nitrogen and phosphorus). It is estimated that the annual cost of damage mediated by eutrophication in the U.S. alone is approximately $2.2 billion (Dodds et al. 2009). Another evident consequence caused by contaminated water is waterborne diseases. Pathogens in contaminated waters are responsible for the spread of many waterborne diseases, which kill around 2.2 million people globally each year, most of which being children in developing countries (WHO 2020).

In order to leave the present and future generations an adequate, reliable and sustainable water supply, it is necessary to establish stable and efficient mathematical models that can accurately predict surface flooding evolutions, pollutant transports and biochemical interactions etc. Key parameters predicted by these mathematical models, such as water elevations, velocities, and the range of pollutant spread, are vital for effective water resources management. These supports can inform policy makers about sustainable water supply, reasonable flood control and timely rescue strategies, which is of great importance to the safety and welfare of future generations.

1.2 Objectives

Among natural water bodies, many can be described as shallow water, such as estuarine, coastal and inland flows. The horizontal scale of these flows is much larger than its depth. Consequently, it can often be assumed that the solute is well-mixed vertically over the water column, allowing a depth-integrated approach to investigate the solute transport processes. Accordingly, this thesis will focus on the hydrodynamic and solute transport processes in shallow water environment specifically. The depth-averaged computational fluid dynamics models will be deployed to achieve a detailed understanding of the rapidly varying flooding flows and the solute transport characteristics in various flow conditions. To achieve this objective, the research is split into the following three parts:

- Demonstrate the influence of the Boussinesq coefficient on the numerical modelling of rapidly varying flows

In the hydrodynamic modelling, the difficulty lies in the simulation of rapidly varying flooding flows. It is well-known that the traditional numerical schemes are unable to resolve shocks, such as hydraulic jumps and bores. Some widely adopted numerical treatments are available for stabilising the traditional schemes so as to deal with these trans-critical and supercritical flows. The first is to introduce artificial diffusion, the second is to modify the Boussinesq coefficient, and the third is to use robust numerical methods, such as Riemann solvers. These treatments can partly mitigate the inherent instability of numerical models when simulating rapid flows. However, these treatments may result in serious deviations from the correct solutions to the

original governing equations. The aim of the research in this part is to demonstrate the impact of modifying the Boussinesq coefficient over a range of flow conditions.

- Develop a depth-averaged and highly robust random walk model for simulating the two-dimensional (2-D) solute transport processes

In the solute transport modelling, most of the previous research is based on Eulerian approaches to solve the standard advection-diffusion equation. However, these grid-based methods have proven to be deficient in addressing steep concentration gradients and tend to produce numerical diffusion. The Lagrangian methods are better suited for the simulation of complex situation involving high contamination gradients. The random walk model is based on the particle tracking approach, which is a representative of the Lagrangian approaches. The research in this part adopts the random walk model and aims to examine its performance for 2-D solute transport modelling.

- Refine the random walk model for modelling the advection, diffusion and reaction processes of non-conservative materials

Most previous random walk methods only consider inert materials, without taking into account the biochemical reactions. In addition, only the instantaneous release problems with a fixed number of particles in the computational domain are examined. Thus, the research in this part aims to bridge the gap and improve the random walk model to simulate more complex phenomena that involve the transport of non-conservative materials in real-world situations.

1.3 Outline of the thesis

The rest of this thesis is structured as follows:

Chapter 2 reviews previous modelling approaches in the general field of hydro-environmental modelling. The emphasis is given to the numerical methods for predicting the rapidly varying flows, moving boundaries, conservative and non-conservative solute transport related problems.

Chapter 3 describes the governing equations employed for the shallow flows and relevant computational techniques. The explanation of certain assumptions and simplifications and special numerical treatments are introduced in detail.

Chapter 4 demonstrates the impact of modifying the Boussinesq coefficient when simulating rapid flows in various situations. The test cases include one-dimensional (1-D) and two-dimensional (2-D), steady and unsteady, sub-, super- and trans-critical flows. The shock-capturing TVD-MacCormack model is used as reference.

Chapter 5 presents the theoretic basics and details of the governing equations employed for solute transport modelling and the explanations of the random walk method. Interpolation technique and boundary treatments are explained in detail.

Chapter 6 carries out extensive parametric studies on the influences of the number of particles, the size of time steps and the technique of sampling processes used in the random walk model. The test cases involve steady and

unsteady flows, flat and uneven beds, rectangular and circular computational domains.

Chapter 7 selects several classical test cases to showcase the capability of the random walk model in addressing the problem of continuous release of non-conservative substances. Details of the verifications of the model against the analytical solutions are provided. The proposed algorithms are applied to a real-world case of the Thames Estuary and the results are compared with published results obtained using the traditional mesh-based method.

Chapter 8 provides a summary of the study and the main conclusions drawn from this research. This is followed by plans of further research.

Chapter 2

Literature review

Hydro-environmental problems have been studied intensively since they can give rise to a series of serious environmental problems and cause significant economic loss. The existing research related to the numerical modelling of both hydrodynamic and solute transport processes will be reviewed in this chapter. First, a brief summary in the general field of the environmental hydraulics will be given to provide an outline of the background, development and current status of the research topic. This is followed by the review of different numerical models involved in the study and the advantages and disadvantages of the relevant methods. Then, the emphasis will be put on the numerical studies of shallow water environment in the two sub-model classification: hydrodynamic modelling and solute transport modelling. The basic fluid mechanisms, governing equations and

numerical methods will be summarised to form the theoretical base for this research. Finally, the gaps and limitations of existing literature will be discussed.

2.1 Environmental hydraulics

Environmental hydraulics, a comprehensive research topic, studies environmentally related hydraulic problems. Unlike traditional hydraulics, it is not only focused on the movement of water flow itself, but also on the movement and interaction of the substances contained in the water body. It involves a wide range of disciplines, such as hydraulics, hydrology, hydrochemistry, hydrobiology, ecology, oceanography, physical limnology and sedimentology, etc. Since Taylor (Taylor, 1922) first proposed the turbulent diffusion theory of the water flow in 1922, this research topic has a history of nearly 100 years. At the beginning, it went through a slow early stage of development until the late 1960s. The subject was limited to the study of the diffusion, transport and transformation of non-living substances in water. Then, with the highlight of ecological problems such as water eutrophication, its research object has extended to aquatic organisms such as algae, zooplankton, fish and benthos (Hunt 1999). The flow conditions, boundary conditions, interactions between abiotic components and biological components, and food chain relationships among aquatic biological components became important factors in environmental hydraulics (Koelmans et al. 2001). The content of environmental hydraulics has been continuously enriched and updated until now (Zeng et al. 2021).

Thanks to the advanced computing techniques, many mathematical models have been established to solve environmentally related hydraulic problems, such as flooding prediction, pollutant transport, river erosion and siltation, sediment transport and so on (Chapra, 2008). Accordingly, a high-quality comprehensive water environmental model usually consists of several sub-models, including hydrodynamic model, solute transport model, sediment migration model, toxic substance migration model, etc. In general, these models are particularly focused on three factors:

(1) Physical factors

Physical factors concerned in the hydro-environmental models include hydrodynamic features, sediment transport and topographic conditions. These physical processes describe the movement of pollutants or solute by fluid motion. This is primarily by the action of advection, the fluid moving, and diffusion, the motion of molecules and turbulent fluctuations in the fluid. In practice, the behaviour of the fluid is assumed to be unaffected by the pollutant and can be calculated independently of the pollutant transformations. This assumption is not suitable for salt and heat transport and highly concentrated sediment transport.

(2) Chemical factors

Chemical factors in the hydro-environmental modelling include conservative and non-conservative material transmission processes. These processes involve the reaction of two or more compounds with each other to form one or more different compounds. Materials that are not transformed chemically while being transported are termed conservative substances,

otherwise they are non-conservative substances. For example, dissolved salts are conservative as they do not interact with other substances. Nitrogen, in its ionic state will undergo chemical, physicochemical and biological transformation in a water body.

(3) Biological factors

Biological factors involve interactions between different organisms in the food chain, including consumption, growth, mortality and respiration from organisms. Biochemical processes are a result of chemical transformations taking place within a biological organism, such as bacterial decomposition of organic material and photosynthesis (Zoppou 2001).

Due to the earlier urbanisation process, developed countries in Europe and the United States have established many hydro-environmental models since the 1960s (Crawford and Linsley, 1966). These models can be classified according to the specific research object solved, or according to the dimension of the governing equation used, from very simple lumped models to complex hydraulic models.

Lumped models try to find a relationship between historical inputs and outputs instead of using physical laws of mass and energy transfer. This transformation process can be described by a relatively simple, intuitive model or a complex, statistical time-series procedure. In both cases, the model can be calibrated by establishing a statistical regression relationship between the input and output. These models provide very little details of the behaviour of the flow or pollutant. In general, these models are used to provide long-term averages or peak values.

Statistical models used for estimating both water quality and quantity characteristics are usually based on regression principles. The principles used in these models include simple linear, multiple linear, semi-log transform and the log-log transform (Bidwell, 1971; Jewell and Adrian, 1981). The statistical relationships are developed from a given set of data reflecting a particular spatial arrangement. The limitations of such models are that if there are any different spatial patterns and processes, new data must be collected, and a new statistical relationship must be developed. Therefore, the statistical approach can be used only for crude analysis.

Empirical models involve a functional relationship between a dependent variable and variables that are considered germane to the process. These variables are chosen from knowledge of the physical processes involved and from empirical measurements. For example, the rational formula is a typical approach for empirically estimating surface flooding processes. The rational method is a simple relationship between flow rate, the catchment area and the rainfall intensity. However, the real processes are quite complex, and the concepts combine and gloss over many different mechanisms. It can only provide peak flooding volumes rather than produce detailed information which is insufficient for accurate prediction.

The distributed models are based on differential equations that allow the flow rate and water level to be computed as functions of space and time, rather than of time alone as in the lumped models. These equations involve the continuity and the conservation of momentum. The differences between distributed and lumped models are how the model treats spatial variability. A

lumped model takes no account of the spatial distribution of the input, whereas distributed models include spatial variability.

Hydrologic models usually satisfy the continuity equation only, while hydraulic models solve simultaneously the continuity and dynamic equations. At early stage, hydraulic method is seldom used due to the complexity of the process and the lack of a reliable and valid solution (Chiu and Huang, 1970; Pilgrim, 1976). However, in consideration of its ability to offer a decent prospect about a detailed process, scholars have made some valuable explorations in the past few decades.

The hydraulic methods are considered as the most accurate modelling approach to study the hydro-related problems. A range of hydrodynamic and solute transport models using computational fluid dynamics techniques have already been applied extensively for research and practical purposes in the field of hydro-environmental modelling. These models can be classified into one-, two- and three-dimensional models. For example, HEC-RAS is one typical example of 1-D models (Brunner, 2002). The DIVAST (Falconer, et al, 2001) can be classified into 2-D models. The TRIVAST (Lin and Falconer, 1997) is regarded as a three-dimensional model. The Danish Hydraulic Institute (DHI, 2018) has been developing a series of MIKE commercial software products for more than 25 years. They are mainly based on the finite-difference technique and available in one-, two- and three-dimensions. The open TELEMAC-MASCARET system is an integrated modelling tool for applications in the field of free-surface flows, managed by Artelia (France), Bundesanstalt für Wasserbau (Germany), Daresbury Laboratory (UK), and HR Wallingford (UK) etc. The system is mainly based on the finite-element

technique, written in the programming language FORTRAN 90 (Matta, 2018). The Delft3D Flexible Mesh Suite developed by the Deltares institute is a commercial software package. It includes one-, two- and three-dimensions modules and is capable of simulating wind-, tides- and density-induced flows (Waldman et al. 2017). These models have made great contributions to solving problems of water supply, flood control, irrigation, drainage, water quality, power generation and wildlife propagation.

2.2 Hydrodynamic modelling

It is widely accepted that natural water falls into the category of Newtonian fluids and their motion can be described by partial differential equations. As they are incompressible fluids, turbulent flows in natural waters are governed by the incompressible Navier-Stokes equations. Solving the full Navier-Stokes equations numerically without any simplification is called Direct Numerical Simulation (DNS). This means that the entire range of temporal and spatial scales of the turbulence must be numerically solved in the computational mesh. However, the computer speed and the storage capacity are still not sufficient to resolve practical applications when using such scheme. Based on reasonable assumptions, some simplifications for the Navier-Stokes equations have been established. One of the typical examples is the Reynolds Averaged Navier-Stokes equations (RANS), which is first proposed by Osborne Reynolds in 1895 (Reynolds, 1895). Shallow Water Equations (SWEs) are another widely-accepted simplified form of the Navier-Stokes equations. The horizontal scale of rivers, lakes and oceans is usually much larger than the

vertical scale. This type of free surface flow problem can be mathematically described by the SWEs. These equations can be derived from the depth integration of the three-dimensional incompressible Navier–Stokes equations or RANS under the assumptions of hydrostatic pressure distribution and negligible vertical velocity. With the appropriate initial conditions and boundary conditions, these nonlinear equations can be solved numerically. The Saint-Venant equations are 1-D form of SWEs. In complete form, the Saint Venant equations can be expressed as following:

Continuity equation:

$$\frac{\partial A}{\partial t} + \frac{\partial Q}{\partial x} = 0 \qquad [2.1]$$

Momentum equation:

$$\frac{1}{A}\frac{\partial Q}{\partial t} + \frac{1}{A}\frac{\partial (Q^2/A)}{\partial x} + g\frac{\partial \eta}{\partial x} - g(S_0 - S_f) - \frac{\tau_w}{H\rho} = 0 \qquad [2.2]$$

where A is the cross-sectional area, Q is the discharge rate; x is the distance, t is the time, g is the acceleration due to gravity, η is the water surface elevation, τ_w is the wind shear stress, ρ is the water density, H is the total water column depth, S_0 is the bed slope, S_f is the friction slope. In the momentum equation, the first term from the left side is the local acceleration term; the second term is called the convective acceleration term; the third term is the pressure force term; the fourth term is the gravity force term and the fifth is the friction force term. These equations are hyperbolic, and the solution of the equations is computationally demanding. This restricts the high-resolution simulation over a large area. As a consequence, various approximations have been more commonly used in the past. The kinematic and the diffusion wave equations

are simplified versions of the Saint-Venant equations. The kinematic wave model ignores the influences of backwater and assumes that the local and convective acceleration and the pressure terms are relatively small compared to the bed slope. The diffusion wave equations assume that the local and convective acceleration terms can be neglected in the momentum equation. This assumption is valid for overland flow or on very steep channels only. The kinematic wave speed can be obtained by differentiating the functional form of the monotonic relationship between Q and A. The kinematic wave does not experience any attenuation, but it does steepen with time. In practical problems, this equation is solved numerically. The numerical scheme introduces numerical diffusion, which results in attenuation of the simulated hydrodynamic features. This diffusion has no physical justification. It is dependent on the computational time and distance steps used in the model. A major advantage with this and other approximations to the SWEs is that detailed information on the computational catchment is not required. Only the kinematic wave speed is required, which can be calculated from channel properties or estimated from observed data. Since this approximation possesses one system of characteristics, then only one boundary condition is required for its solution. With the development of computing technologies, the simulation of 2-D unsteady flow has become mature today.

Researchers have developed various numerical methods to solve the SWEs over the past few decades, including the finite-difference method (Casulli 1990; Bates et al. 2010), finite-element method (Hervouet 2007) and finite-volume method (Song et al. 2011; Costabile 2012). For these methods either structured or unstructured grid can be used (Hou et al. 2013; Hou et al.

2014; Pavan et al. 2015), while time marching schemes can be explicit, implicit or semi-implicit. There also exists an ongoing development of robust and high-resolution numerical methods (Hinkelmann et al. 2015; Simons 2020). These robust numerical methods can handle arbitrary complex applications and provide accurate results for cases with varying topography.

The Alternating Direction Implicit (ADI) scheme is one of traditional methods which is still widely used. This scheme was first proposed by Peaceman and Rachford (1955), after which Leendertse combined the ADI scheme and a staggered grid and developed a computational model for 2-D flows. The stability domain of this scheme is relatively large, and the balance between computational cost and accuracy is attractive (Leendertse and Gritton, 1971). Two established approaches are suitable for resolving shocks, such as hydraulic jumps and bores, in the solution, i.e. shock-fitting and shock-capturing methods. Shock-capturing methods are preferable since they utilize a universal strategy over the whole domain without treating the shocks separately. As for most explicit schemes, time steps for shock-capturing schemes are restricted by the Courant–Friedrichs–Lewy (CFL) condition. The ADI scheme is widely used in practice to solve the SWEs. By adopting the implicit schemes alternately, the growth of the computation error is restricted to increase the stability of the computation. At the same time, the computation is highly efficient with the deployment of the Tri-Diagonal Matrix Algorithm (TDMA). However, this scheme has been proved to be incapable of predicting flows with steep water levels and large velocity gradients (Meselhe and Holly, 1997, Liang et al., 2006a). The lack of shock-capturing capability makes this scheme unable to predict accurately the rapidly varying flows containing

sudden hydraulic jumps, drops and bores. Some numerical treatments can partly mitigate the inherent instability of the ADI model when solving for trans-critical flows. For example, one way is to introduce artificial diffusion, another way is to modify the Boussinesq coefficient. The effect of artificial viscosity on the computational results has been extensively studied, the influence of the Boussinesq coefficient is not well understood yet.

2.3 Solute transport modelling

Water quality problems have detrimental impacts on the environment, which may cause potential risks on human health and result in significant economic losses. Accurate and efficient water quality estimation is essential for establishing a control strategy for environmental protection (Benkhaldoun et al. 2007). In the past few decades, increasing emphasis has been put on the numerical modelling of pollutant transport and biochemical reaction processes. At the early stage, Streeter and Phelps are the first to establish the relationship between the decay of an organic waste measured by the Biochemical Oxygen Demand (BOD) and Dissolved Oxygen (DO) resources of the river in 1925. The concentration of the DO is an essential indicator for analysing the nutrient cycle in flows (Jha et al. 2007). The ability to maintain an adequate DO concentration is important for determining the waste assimilative capacity. This simple BOD-DO bilinear system model is also called the Streeter-Phelps model. This model focuses on oxygen balance and one-order decay of BOD and they are 1-D steady-state models. After that, many researchers modified and further developed the Streeter-Phelps models. Since 1970, water quality models made a rapid progress based on further studies on multidimensional coefficient

estimation of BOD-DO models (Wang et al. 2013). For example, the US Environmental Protection Agency (USEPA) developed the first version of QUAL model in 1970. QUAL models are suitable for dendritic river and non-point source pollution, including 1-D steady-state or dynamic models (Grenney et al. 1978). In water quality modelling, pollution from industrial and sewage treatment plants is called point source pollution. Nonpoint source pollution comes from diffuse sources. For example, pollution caused by rainfall or snowmelt moving over and through the ground is called nonpoint source pollution. Overland flows pick up and carry away these natural and artificial pollutants and then deposit them into lakes, rivers, wetlands, coastal waters and ground waters. The WASP model was also developed by the USEPA in 1983. The WASP model is suitable for water quality simulation in rivers, lakes, estuaries, coastal wetlands, and reservoirs, including one-, two-, or three-dimensional models (Ambrose et al. 1988). Whitehead established the QUASAR model in 1997. QUASAR model is suitable for dissolved oxygen simulation in larger rivers, and it is a 1-D dynamic model (Sincock et al. 2002). Denmark Hydrology Institute developed the MIKE model (Vázquez et al. 2002), which is suitable for water quality simulation in rivers, estuaries, and tidal wetlands, including one-, two-, or three-dimensional models. These surface water quality models are still widely applied worldwide and are continually updated.

The transport of pollutants is modelled using a mass conservation equation, which includes the two fundamental transport processes, advection and diffusion. As shown in the Figure 2.1, advection is the transportation of a substance by a fluid due to the fluid's bulk motion. In this process, we assume

that the solute material exactly follows the flow. Diffusion is the process whereby mass transports from higher concentration to lower concentration in flow due to random movements. It is assumed that the diffusive substances would not affect the motion of flows. In other words, the flow field is independent of the existence of the diffusive materials.

Diffusion is the transportation of pollutants in the direction of decreasing gradient by molecular motion or turbulent fluctuations in the water. Molecular motion is defined as the movement of constituent particles or molecules in a certain direction. The molecular motions are affected by heat and temperature. This is because the temperature is the measurement of the average kinetic energy of the molecules. The rate of molecular motion is quite slow. Turbulent diffusion is another diffusion process that is relatively faster. In general, turbulent diffusion is much larger than molecular diffusion. It is well known that turbulence significantly enhances the transport and mixing of flows. It consequently plays a significant role in determining the flow velocity, distributing heat and dissolving substances such as salt and oxygen (Castanedo et al. 2005). Consequently, a critical factor for the success of shallow water simulations is to adequately take the effects of turbulence into consideration. Most models in practical use today address this issue by using the Boussineq eddy-viscosity concept, which assumes that turbulent stresses are related to the velocity field in a similar manner as the molecular viscosity. An effective viscosity therefore consists of two parts, one from the molecular and the other form the turbulence, where the latter is often much larger. Cea et al. (2007) compared different turbulence models for shallow flow simulations and concluded that complex turbulence models (such as mixing length, k-ε and

k-ω models) give the same eddy viscosity as simple ones in the extremely shallow flow simulation.

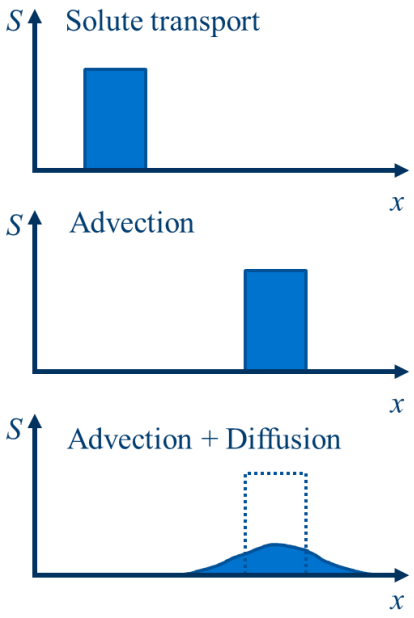

Figure 2.1 Advection and diffusion processes.

The 1-D conservative advective-diffusion equation is the basic equation that incorporates the advection processes and diffusion processes. This equation can be used to describe the behaviour of a pollutant in a 1-D stream.

$$\frac{\partial(A_x s)}{\partial t} + \frac{\partial}{\partial x}(uA_x s) = \frac{\partial}{\partial x}(A_x D_x \frac{\partial s}{\partial x}) \pm O_S \qquad [2.3]$$

in which s is the thermal energy or constituent concentration, x is distance, u is the advection velocity, A_x is the cross-sectional area in the x direction, D_x is the diffusion coefficient and O_S represents all sources and sinks in this 1-D situation. This equation includes the advection of pollutant by the flowing water, diffusion of pollutant in the stream, constituent reactions, interactions

and sources and sinks. Assuming that A_x and D_x are constant and using the flow continuity equation. Then the equation is:

$$\frac{\partial(A_x s)}{\partial t} + \frac{\partial}{\partial x}(uA_x) = 0 \quad [2.4]$$

$$\frac{\partial s}{\partial t} + u\frac{\partial s}{\partial x} = D_x\frac{\partial^2 s}{\partial x^2} \pm O_s \quad [2.5]$$

For non-conservative pollutants, it can include a production or loss of a pollutant, with or without interaction with another pollutant. This is known as a kinetic process, including the chemical and physicochemical processes. Generally kinetic processes are adequately described by first-order relationships. Some pollutants are usually coupled. With one pollutant decaying another may be formed or degrade. This will lead to a set of simultaneous equations. The advantage of first-order processes, which are coupled, is that the overall first-order rate coefficient is the sum of the first-order rates for the individual pollutants. This is a common approach adopted in many water quality models.

2.4 Eulerian approach and the Lagrangian approach

Basically, numerical methods used in both hydrodynamic modelling and solute transport modelling can be classified into two categories; one is the Eulerian approach and the other one is the Lagrangian approach. Each of them has its own pros and cons.

The Eulerian approach is often regarded as the grid-based approach. It develops the conservation equations on a control volume basis and divides the computation domain into grid systems. The grid or mesh system sets up the

domain and the shape for the simulation. In general, two grid types are widely used in the numerical modelling: one is the structured grid system and the other one is the unstructured grid system. Structured grid system offers a simple and efficient approach for the solution of the governing equations. The rectangular grid is one of the most widely used structured grid. For example, the rectangular grid is used in DIVAST (Falconer et al., 1999). However, the rectangular grid systems are unable to resolve local features of a complicated geometric domain. By contrast, unstructured grid systems provide geometric flexibility and simplicity in which the grid can be adapted according to the local topographic and flow features. Common types of unstructured grid systems include the classical triangular or tetrahedral grids, quadrilateral or hexahedral grids, prismatic grids or mixed grids. (Casulli and Walters, 2000; Begnudelli et al. 2006). Previously, most of numerical models rely on mesh-based Eulerian methods to solve the standard SWEs and advection-diffusion equations using finite-difference, finite-element or finite-volume techniques (Lin and Falconer, 1997; Mingham et al. 2001; Benkhaldoun and Mohammed, 2007). Due to the limited computation power, the Lagrangian approach was thought to be computational expensive. It has been widely known that these Eulerian approaches tend to produce artificial diffusion when addressing steep concentration gradients and are sensitive to the grid. The results presented in the chapter 4 also demonstrate non-physical oscillations and inefficiency in the traditional mesh-based method. Thanks to advanced computing techniques, increasing level of attention has been paid to Lagrangian approaches, which have higher stability and simplicity than mesh-based methods. (Pu et al. 2016; Kazemi et al. 2017; Zheng et al. 2017)

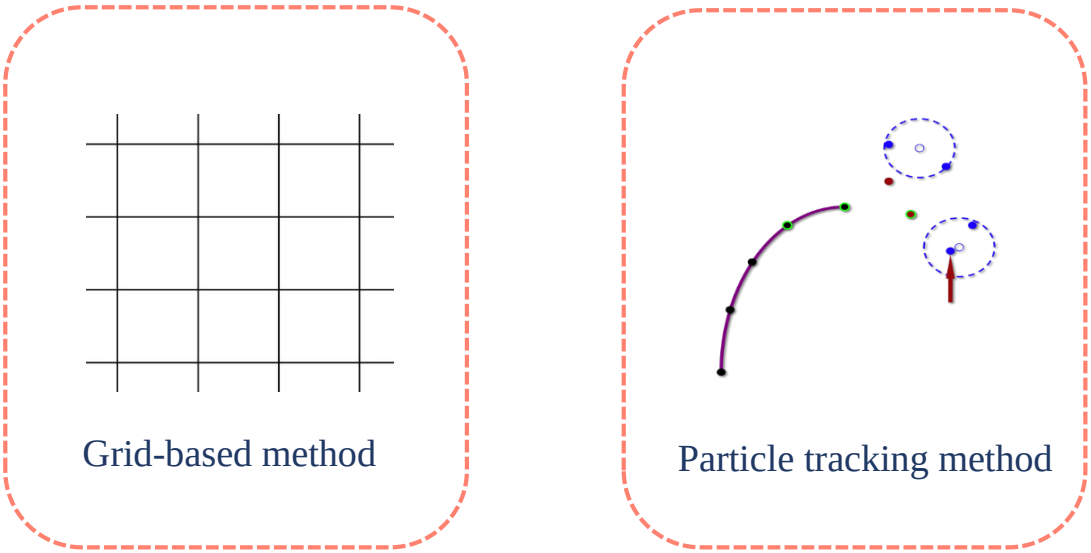

Figure 2.2 General concept of the Eulerian approach and the Lagrangian approach

The Lagrangian approach uses particles as discrete phases and tracks the pathway of each individual particle. By studying the statistics of particle trajectories, the Lagrangian approach is able to calculate the concentration of particles or other phase data (Zhang and Chen, 2007). The random walk method is a typical mesh-free approach for modelling pollutant transport (e.g. Israelsson et al. 2005; Liang and Wu 2014). It originates from statistical physics and has been applied in many disciplines such as finance, biology and hydrology. In modelling solute transport, the random walk method tracks the movement of discrete particles, which serve as indicators to represent the pollutant cloud.

Israelsson et al. (2005) summarised the strengths and weaknesses of three Lagrangian techniques and concluded that the random walk method is most

accurate and flexible. Wu and Liang (2019) proved that the random walk method can achieve higher accuracy than Eulerian models and is better suited to the situation with high contamination gradients. This method is attractive opposed to Eulerian grid-based methods for several reasons. First, they are inherently mass conservative by the definition. Secondly, discrete particles can more easily represent sub-grid scale processes without suffering from numerical dispersion. Thirdly, the approach is efficient when pollutant clouds only occupy a small area of the computational domain. Last but not least, the method offers advantages with certain types of boundary conditions and is useful for visualizing transport pathways. However, it is worth mentioning that the random walk method does have some limitations. For example, there is some artificial diffusion when interpolating the particle tracking results to a grid and the number of particles is unknown a priori and must be determined by trial and error.

The relative computational efficiency between the Lagrangian and Eulerian models depends on the studied problems. The computational cost of the random walk model depends on the number of particles and the time step. Because a large number of particles are needed to obtain smooth concentration distributions, the random walk method is often thought to require significant computing resources. The computational cost of the traditional mesh-based model depends on the mesh resolution and the time step, with the latter often limited by the CFL condition. However, the mesh-based methods often suffer from numerical diffusion unless extremely fine mesh is used. Therefore, if such extremely fine mesh is used, then the random walk method can be more efficient as it is free from numerical diffusion and the computation is restricted

to regions where pollutant clouds exist. In practice, however, the mesh-based model has to adopt coarse meshes for the computational time to be affordable. The dispersion and diffusion coefficients are specified by calibrating the computational results against measurements, and their values take into account the effect of numerical diffusion rather than truly reflect the physical processes. When taking such a strategy, the mesh-based model is often more efficient than the random walk method.

In short, the Lagrangian method has become more and more popular recently, and Euler's method can still be supplemented to some extent in many aspects. To choose the Eulerian method or the Lagrangian method for certain problems depends highly on the objective and characteristics of the problem under examination.

2.5 Chapter summary

In this chapter the development of different hydro-environmental models involved in the study and the advantages and disadvantages of the relevant hydro-environmental models are reviewed. Then, basic theories and the numerical methods according to the two sub-model classification, the hydrodynamic modelling and the solute transport modelling, are summarised. In the past few decades, increasing emphasis has been put on the numerical modelling of hydrodynamic and water quality characteristics in estuarine, coastal and river waters. In the hydrodynamic modelling, the SWEs are the governing equations to the free surface water modelling. Traditional numerical

schemes are found to be unable to accurately predict the rapidly varying flows containing sudden hydraulic jumps, drops and bores. In the solute transport modelling, the advection—diffusion equations are employed for mass transport processes. The increasing level of attention has been paid to Lagrangian approaches to solve the solute transport problems.

Chapter 3

Hydrodynamic modelling

As mentioned in chapter 2, hydrodynamic features in estuarine, coastal and rivers can be mathematically described by the SWEs. These equations are derived from the depth integration of the three-dimensional incompressible Navier–Stokes equations under the assumptions of hydrostatic pressure distribution and negligible vertical velocity. Due to the much greater horizontal extent of the surface than the water depth, the application of this depth-averaged modelling approach is appropriate. Saint-Venant equations have been discussed in Chapter 2, which are the 1-D form of SWEs. Here, the 2-D form of SWEs is presented.

Chapter 3

3.1 2-D Shallow water equations

Navier-Stokes equations and the three-dimensional Reynolds averaged continuity can be integrated over the water column when the three assumptions are utilized:

1) The vertical depth scale is much smaller than the horizontal scale:

If the changes in physical parameters along the water depth are much smaller than those in the horizontal direction, the acceleration along the water depth can be approximately ignored. In addition, the shear stress and advective acceleration generated by the velocity components in the depth direction can also be ignored, which greatly simplifies the problem.

2) Hydrostatic pressure distribution is assumed:

In the shallow water environment, the vertical advection is much smaller than the pressure gradient and gravitational acceleration. The velocity gradient in the depth direction can be regarded as zero, which satisfies the condition of hydrostatic pressure distribution.

3) The influence of Coriolis forces and air pressure gradient are ignored:

The influence of Coriolis forces needs to be considered only if the flow field is in an area with a large difference in latitude, while that of air pressure gradient is important only for large-scale ocean modelling. Water flow considered here, however, is assumed to be mainly driven by gravity, friction and hydrostatic pressure, and as a result their influences are neglected.

The resulting depth-integrated equations are referred as the SWEs. Once given the appropriate initial conditions and boundary conditions, these nonlinear problems can be solved numerically. The standard 2-D SWEs can be simplified in the following form:

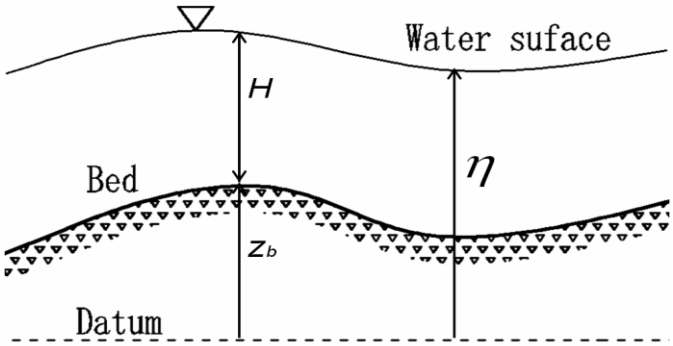

Figure 3.1 Coordinates for shallow water equations

Continuity equation:

$$\frac{\partial \eta}{\partial t} + \frac{\partial q_x}{\partial x} + \frac{\partial q_y}{\partial y} = I \qquad [3.1]$$

Momentum equation in x direction:

$$\frac{\partial q_x}{\partial t} + \frac{\partial\left(\frac{\beta q_x^2}{H}\right)}{\partial x} + \frac{\partial\left(\frac{\beta q_x q_y}{H}\right)}{\partial y} = -gH\frac{\partial \eta}{\partial x} - \frac{g q_x\sqrt{q_x^2+q_y^2}}{H^2C^2} + \upsilon\left[2\frac{\partial^2 q_x}{\partial x^2} + \frac{\partial^2 q_x}{\partial y^2} + \frac{\partial^2 q_y}{\partial x \partial y}\right] + \frac{\tau_{wx}}{\rho} \qquad [3.2]$$

Momentum equation in y direction:

$$\frac{\partial q_y}{\partial t} + \frac{\partial(\frac{\beta q_y^2}{H})}{\partial y} + \frac{\partial(\frac{\beta q_x q_y}{H})}{\partial x} = -gH\frac{\partial \eta}{\partial y} - \frac{g q_y\sqrt{q_x^2+q_y^2}}{H^2C^2} + \upsilon\left[\frac{\partial^2 q_y}{\partial x^2} + 2\frac{\partial^2 q_y}{\partial y^2} + \frac{\partial^2 q_x}{\partial x \partial y}\right] + \frac{\tau_{wy}}{\rho} \qquad [3.3]$$

where t is time; η represents the the height of the water surface above the datum in Figure 3.1; q_x and q_y are the volumetric discharge per unit width in the x and y directions respectively, as shown in Equation [3.4]; I represents the mass source term due to injection and abstraction of water; H $(= -z_b + \eta)$ is the total water column depth, in which z_b is the height of the bed above the datum; g is the gravitational acceleration; β is called the Boussinesq coefficient – a momentum-correction factor for the non-uniform vertical velocity profile; ν is the kinematic eddy viscosity; τ_{wx} and τ_{wy} are the wind stress components; ρ is the water density;C represents the Chezy roughness coefficient which is determined from the Manning formula n.

$$q_x = \int_{z_b}^{\eta} u dz,\ q_y = \int_{z_b}^{\eta} v dz \qquad [3.4]$$

$$C = \frac{1}{n} H^{1/6} \qquad [3.5]$$

Equations [3.1-3.3] are not in a conservative formulation of the SWEs. As a set of hyperbolic equations, the SWEs admit discontinuities in their solutions. In order to maintain the correct motion of the shocks in numerical prediction, the conservative form of the SWEs should be deployed to ensure the exact mass and momentum conservation in the numerical discretization (Toro, 2001; Liang et al. 2006a). Therefore, these equations are rearranged into the following conservative forms. The water free surface gradient terms on the right-hand side of Equations [3.2] and [3.3] can be transformed as (viscous terms are neglected):

$$-gH\frac{\partial \eta}{\partial x} = -\frac{\partial\left(\frac{g\eta^2}{2} + gz_b\eta\right)}{\partial x} + g\eta\frac{\partial z_b}{\partial x} \qquad [3.6]$$

$$-gH\frac{\partial \eta}{\partial y} = -\frac{\partial\left(\frac{g\eta^2}{2}+gz_b\eta\right)}{\partial y} + g\eta\frac{\partial z_b}{\partial y} \quad [3.7]$$

Thus, the momentum Equations [3.2] and [3.3] can be re-written as:

$$\frac{\partial q_x}{\partial t} + \frac{\partial\left(\frac{\beta q_x^2}{H}+\frac{g\eta^2}{2}+gz_b\eta\right)}{\partial x} + \frac{\partial\left(\frac{\beta q_x q_y}{H}\right)}{\partial y} = g\eta\frac{\partial z_b}{\partial x} - \frac{gq_x\sqrt{q_x^2+q_y^2}}{H^2C^2} + \frac{\tau_{wx}}{\rho} \quad [3.8]$$

$$\frac{\partial q_y}{\partial t} + \frac{\partial\left(\frac{\beta q_y^2}{H}+\frac{g\eta^2}{2}+gz_b\eta\right)}{\partial y} + \frac{\partial\left(\frac{\beta q_x q_y}{H}\right)}{\partial x} = g\eta\frac{\partial z_b}{\partial y} - \frac{gq_y\sqrt{q_x^2+q_y^2}}{H^2C^2} + \frac{\tau_{wy}}{\rho} \quad [3.9]$$

Equations [3.8] and [3.9] are the conservative formulation of the momentum equations. Liang et al. (2006a) have shown that this reformulation of momentum equations into Equations [3.8] and [3.9] gives smaller imbalances in the predicted discharges compared with other conservative formulations. As for flows over flat frictionless beds, the right-hand sides of Equations [3.8] and [3.9] vanish and the right-hand sides of the equations can be regarded as the source terms. Therefore, a set of balanced equations composed of Equations [3.2, 3.8-3.9] form the eventual governing equations for the current SWEs solver. They specify the conservations of flow mass and momentum, not only when the solution is smooth but also when the solution contains discontinuities. Their deployment enables the numerical model to track the correct movement of the shock in the computational domain.

3.2 Boussinesq coefficient

As shown in Equations [3.1-3.3], the Boussinesq coefficient β is a momentum-correction factor for the non-uniform vertical velocity profile. For the dam-break flows, flash floods and other rapid flow phenomena, the fluid

inertia, pressure force and bed friction are often the dominant factors influencing the flow, whereas the influence of viscosity is generally insignificant. Assuming the flow is along the x direction, then the Boussinesq coefficient can be defined as:

$$\beta = \frac{\int_{z_b}^{\eta} u^2 dz}{U^2 H} \qquad [3.10]$$

where the flow velocity u is a function of the vertical coordinate z, and U is the depth-averaged velocity. This momentum correction factor depends on the velocity distribution over the depth and should be always greater than unity. It increases with the increasing non-uniformity of the velocity distribution over the depth. For a logarithmic velocity profile, the momentum correction factor can be expressed as (Goldstein, 1938):

$$\beta = (1 + \frac{g}{C^2 \kappa^2}) \qquad [3.11]$$

where κ is von Kármán's constant. From the above equation, it can be seen that the value of β increases with the decrease of the Chézy coefficient, which signifies an increase in the bed roughness, vertical shearing and velocity non-uniformity. Alternatively, an assumed seventh-power law velocity profile leads to a constant value for β of 1.016. The wind generated velocity profiles in semi-enclosed coastal domains can give a value for β of 1.2. This value is based on a parabolic velocity distribution assumption for wind generated flow field according to Koutitas and Gousidou-Koutita (1986) and Falconer and Chen (1991).

In many practical modelling studies, the momentum correction factor is simply set to unity, assuming a uniform velocity distribution. On the other hand, because β appears in the advective acceleration term in Equations [3.2] and [3.3], it can also be used to adjust the amount of fluid inertia to be considered in the computer simulations. Some researchers adjust the Boussinesq coefficient to improve the stability of the ADI-based models, following an idea similar to the adjustment of the viscosity coefficient in the numerical simulations. In such cases, the value of β should be treated as purely artificial, just as the artificial viscosity coefficient. Physically, the value of β should never be smaller than unity according to the Equation [3.11]. However, in the numerical modelling, the advective acceleration can be completely ignored by setting the value of β to be zero.

3.3 Numerical methods

Researchers have developed various numerical models to solve SWEs over the past few decades. In order to ensure that the numerical schemes are capable of capturing discontinuities, two approaches have been employed i.e. shock-fitting and shock-capturing methods. Shock-capturing methods are preferable since they utilize a universal strategy over the whole domain without treating shocks separately. Most shock-capturing schemes fall into one of two major categories. The first category corresponds to the Godunov-type scheme, in which discontinuities are compensated by employing Riemann solver to determine the flux across the interface between two grid cells. The second category is concerned with the combination of the 1st order and second order upwind schemes.

3.3.1 TVD-MacCormack scheme

There are numerous shock-capturing numerical schemes. In this study, the TVD-MacCormack scheme is adopted as a typical one. This scheme is a modification of the widely-used MacCormack scheme by adding an extra step according to the Total Variation Diminishing (TVD) principle. Based on the operator-splitting technique, the solution of the 2-D SWEs can be decomposed into the solution of two sets of 1-D equations in each time step (Roger et al., 2003; Liang et al. 2006, 2007, 2011). The explicit discretization is achieved by a uniform rectangular grid system. By adding an extra term after the corrector step, the TVD-MacCormack scheme enhances the standard MacCormack scheme. In this way, the numerical oscillations are removed theoretically near the sharp-gradient regions and the numerical solution therefore is equipped with the TVD property. The whole scheme has second-order accuracy in both time and space, but it introduces right amount of diffusion to remove numerical oscillations near any steep gradients. Since its development, extensive verifications and applications have been made to demonstrate its accuracy and efficiency, together with many refinements (e.g., Liang et al., 2007.2016; Wang et al. 2016).

3.3.2 ADI scheme

The ADI scheme is one traditional method which is still widely used to solve SWEs. This scheme was first proposed by Peaceman et al. (1955), after which Leendertse modified this model by combining it with the alternating

grid and using it to calculate 2-D flows (Leendertse et al. 1971). In the ADI scheme, each time step is divided into two half time steps. In the first half time step, the x direction terms and derivatives are solved using the implicit scheme, while the explicit scheme is used to solve the y direction terms and derivatives. Conversely, the second half time step is solved using the implicit scheme in the y direction approximation, while the explicit scheme is used in the x direction approximation. By using the implicit alternating operation steps, the growth of the computation error can be restricted. Liang et al. (2006a) showed that the ADI scheme is unable to predict trans-critical and supercritical flows. Currently, the ADI scheme is still widely used in a lot of commercial and research software, such as Flood Modeller (www. floodmodeller.com) and HEC-RAS (www.hec.usace.army.mil). Two widely-adopted numerical treatments are available for stabilising the ADI scheme in simulating rapid flows. One is to introduce artificial diffusion, and the other is to modify the Boussinesq coefficient. These treatments can partly mitigate the inherent instability of the ADI model when solving trans-critical flows.

3.4 Chapter summary

In this chapter, the 2-D conservative formulation of the SWEs has been presented, which are derived from the depth integration of the three-dimensional incompressible Navier–Stokes equations. The physical meaning of the Boussinesq coefficient has been explained. Once given the appropriate initial conditions and boundary conditions, these nonlinear equations can be solved numerically. The shock-capturing scheme, TVD-MacCormack scheme, and the traditional ADI scheme have been introduced. It has been pointed out

that the numerical treatment of modifying the Boussinesq coefficient can partly mitigate the inherent instability of the ADI model when solving for trans-critical flows. However, their results may seriously deviate from the correct solutions to the original SWEs where the Boussinesq coefficient takes the physically based values of around 1.0. Although the effect of artificial viscosity on the computational results has been extensively studied, the influence of the Boussinesq coefficient is not well understood. The research on the hydrodynamic modelling part focuses on demonstrating the impact of changing the Boussinesq coefficient when simulating rapid flows in various situations. The results of this research will be discussed in detail in the Chapter 4.

Chapter 4

Influence of the Boussinesq coefficient on the numerical modelling of rapid flows

In the last chapter, it has been pointed out that the ADI scheme is incapable of modelling trans-critical flows. Its inherent lack of shock-capturing capability often results in spurious oscillations and computational instabilities. However, the ADI scheme is still widely adopted in flood modelling software, and various special treatments have been designed to stabilise the computation. Modification of the Boussinesq coefficient to adjust the amount of fluid inertia is a numerical treatment that allows the ADI scheme to be applicable to rapid flows. However, the impacts of changing this coefficient are not yet well understood. The knowledge of these would be useful for accessing the stability and accuracy of the results calculated from the ADI scheme together with a modified coefficient, which are commonly found in flooding simulations. In this chapter, the impact of this numerical treatment in a range of flow conditions has been comprehensively examined. The test cases include 1-D and

2-D, steady and unsteady, sub-, super- and trans-critical flows. The shock-capturing TVD-MacCormack model mentioned in Chapter 3 is used as the reference.

4.1 Unsteady flow over frictionless bed

Dam break problems have attracted the attention of many researchers in the past few decades. Although the construction of the dam has brought huge economic benefits, the failure of the dam is life-threatening. In the past, many serious losses were caused by dam-break disasters. The upstream and downstream of hydropower stations generally have very large water level differences. Once a dam-break occurs, it will cause devastating disasters. The most significant dam-break disaster in history occurred in the Huaihe River Basin in 1975. In addition to economic losses of up to 10 billion dollars, this dam-break also caused very serious casualties. It is estimated that 10 million people were affected, more than 26000 people died and 30 cities with 12000 km^2 farmland flooded. Moreover, rivers and adjacent areas are heavily polluted, and local crops, fish, turtles and other animals are affected, severely damaging the local ecological environment. Therefore, it is of great significance to attach importance to the safety of hydropower dams, and it is necessary to establish an effective and stable mathematical model to simulate the evolution of dam-break floods.

The dam-break flows are typically rapid varying flows which contain sudden hydraulic jumps, drops and bores. Therefore, it is regarded as a perfect test case to check the capability of numerical models in solving complex situations with high contamination gradients involved. In this section both the

one- and 2-D dam-break problems are considered as test cases. The bed friction is ignored in both scenarios. The analytical solution for the 1-D idealised dam-break problem has been known (Chanson 2005). The solutions predicted by a TVD-MacCormack model and experimental data are used as references.

4.1.1 1-D dam-break problem

A simple and classical 1-D dam-break problem is considered. A side view of the computational setup is demonstrated in Figure 4.1, where h_1 and h_0 represent the water depths of the upstream headwater and downstream tail-water, respectively. The dam is assumed to be located at $x = 500\,m$ with the initial upstream water depth of 10 m and the downstream water depth of 2 m. The grid spacing was 10 m and the Courant number was 0.04. This situation is considered as a 1-D dam-break problem because the dam is assumed to collapse altogether. Conversely, if the dam is only partially ineffective, it needs to be considered as a 2-D problem, which will be discussed in the section 4.1.2.

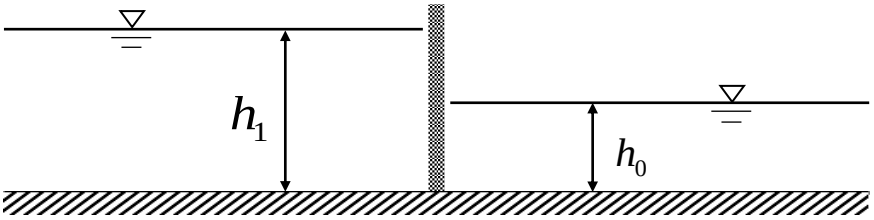

Figure 4.1 Dam-break problem illustration

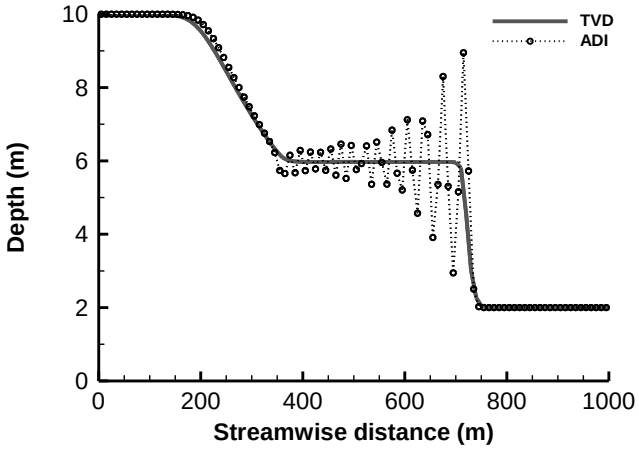

(a) $\beta = 0.5$

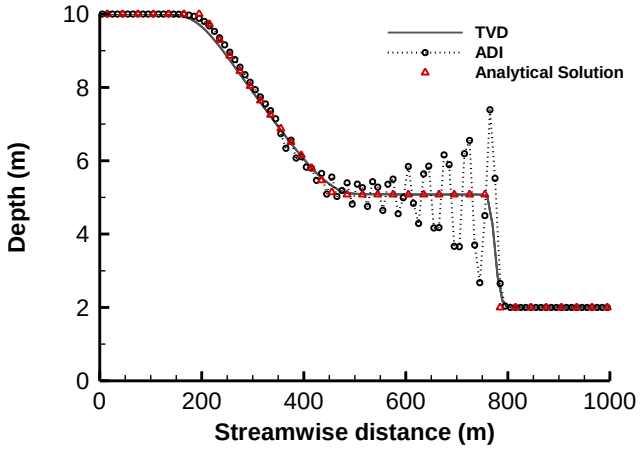

(b) $\beta = 1.0$

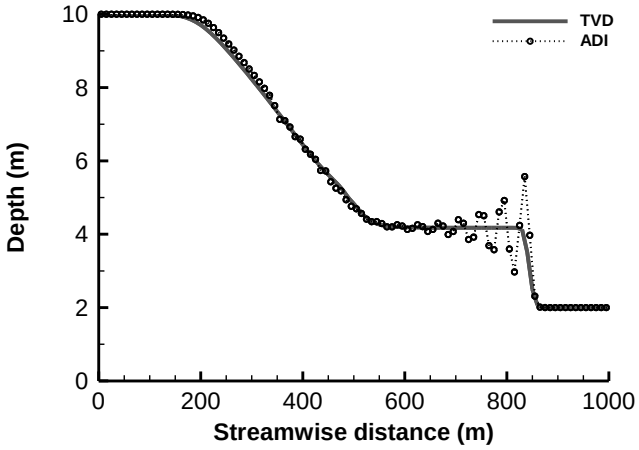

(c) β = 1.5

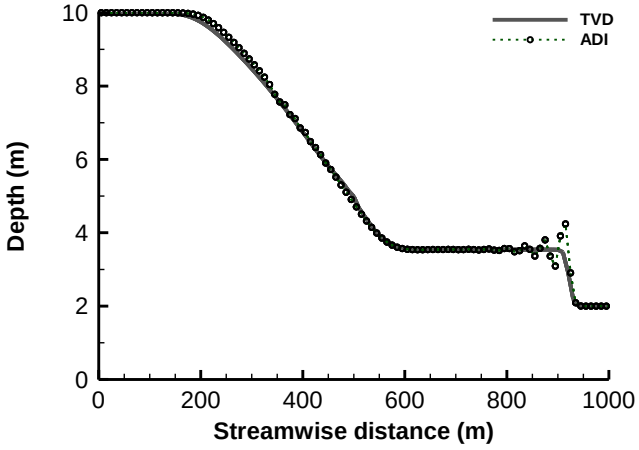

(d) β = 2.0

Figure 4.2 Comparison between ADI model and TVD-MacCormack model.
(a) β = 0.5; (b) β = 1.0; (c) β = 1.5; (d) β = 2.0

Figure 4.2 shows the water surface elevation at 18s after the dam failure, produced by the ADI model and the TVD-MacCormack model, respectively, with four β values, β = 0.5, β = 1.0, β = 1.5 and β = 2.0. The solid lines represent the results predicted by the TVD-MacCormack model, while the dotted lines

represent the numerical solutions for the ADI model. As mentioned in chapter 3, it is estimated that the theoretic value of the β is around 1.016. Therefore, the values of β in the range of 0.2 to 2.0 are mainly studied. In general, the significant difference between the solutions of the two numerical schemes is the occurrence of spurious oscillation or not in the discontinuous region. It is worth noting that when the value of β is relatively large, as shown in Figure 4.2 (d), the oscillation reduces significantly. This can be attributed to a decrease in the height of the flood front, which induces the drop in the amplitude of the oscillation.

It should be noted that artificially modifying the value of β introduces systematic errors to the simulations. The theoretical solution corresponds to the β value of 1.0, which is taken to be the correct solution to this problem. Although increasing β reduces the numerical oscillations in the ADI modelling, the ADI results still deviate from the theoretical solution by predicting the wrong water depth and propagation speed of the flood front. The L_2- norm between the theoretical and ADI-predicted values is defined as:

$$L_2 = \sqrt{\sum_{i=1}^{N}(V_a - V_{ai})^2} \qquad [4.1]$$

where N is the total number of grid points, V_{ai} and V_i and are the theoretical and ADI-predicted values, respectively. These quantities may be either the water depth or the velocity. As seen in Figure 4.3, the minimum L_2-norm is still observed at β = 1.0, in spite of the numerical fluctuations as shown in Figure 4.2 (b). In terms of the propagating speed of the flood, the solutions using the ADI scheme are consistent with the solutions using the TVD scheme. In

addition, the height of flood fronts predicted by the two schemes is shown to decrease as β increases.

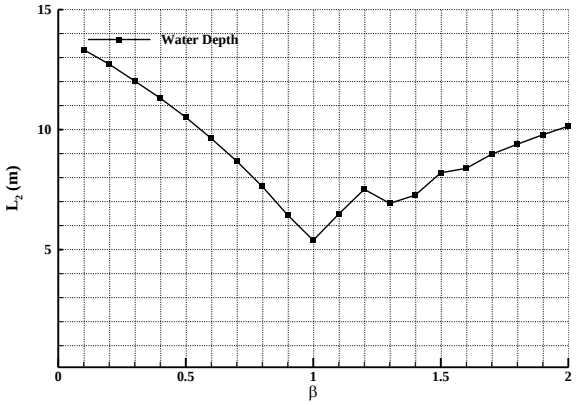

(a) Water depth

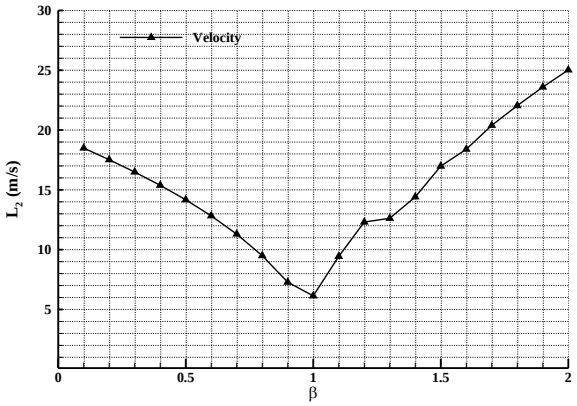

(b) Velocity

Figure 4.3 L_2-norm between the theoretical, with $\beta = 1.0$, and ADI-predicted results. (a) Water depth; (b) Velocity

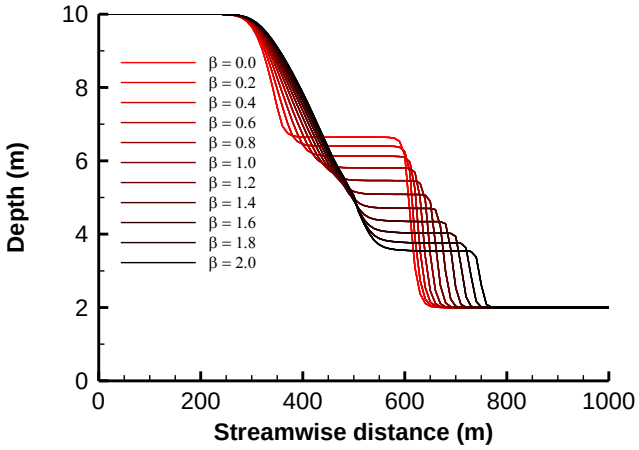

(a) Water depth

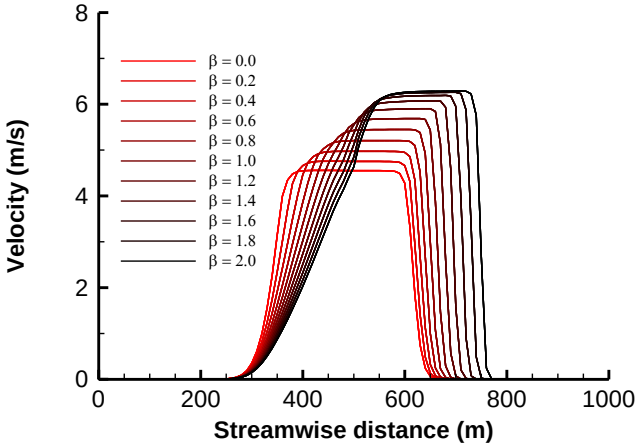

(b) Velocity

Figure 4.4 Predicted results at 18 s after the dam failure by using TVD-MacCormack model. The gradation of colour indicated the increase in β value. (a) Water depth; (b) Velocity

Figure 4.4 (a) and (b) demonstrate the trend of the variation with β using the TVD results alone. The gradation of color indicates the changing value of β. It can be seen that a lower flood-front height and faster flood-front propagation

are associated with a larger β. The faster propagation of the flood front with a larger β can be explained by the eigenvalues of the SWEs. When neglecting the bed friction and fluid viscosity, it can be easily calculated that the eigenvalues of the 1-D SWEs along the x direction are:

$$\lambda_1 = \beta U - \sqrt{(\beta^2 - \beta)U^2 + gH} \quad [4.2]$$

$$\lambda_2 = \beta U + \sqrt{(\beta^2 - \beta)U^2 + gH} \quad [4.3]$$

Hence, the speed of the downstream travelling characteristic, λ_2, increases with the increase of β. Special values of λ_2 are at $\beta = 1$. A smaller β value generally leads to a smaller velocity in the frictionless unsteady flows. The flow velocity determines the water depth through the conservation of mass. As seen in Figure 4.4 (b), a smaller β value then results in a higher water depth at the flood front and a smaller water depth in the reservoir.

4.1.2 2-D dam-break problem

The test case considered in this section is an instantaneous 2-D dam-break flood over a frictionless and flat bed. The dam located at $x = 1$ m divided the whole domain (3 m × 2 m) into two parts. As seen in the Figure 4.5, the water was still in the left reservoir at the beginning, with a depth of 0.64 m, while the floodplain on the right was dry. At the boundaries of the floodplain, a zero gradient condition was specified so that water could escape from the domain freely. In the present simulations, the spatial step was set to be 0.04 m and the Courant number was 0.8. The same symmetrical dam-break

experiment over a flat floodplain was performed by Fraccarollo *et al*. (1995) and their experimental data are referred to in this section for comparison purposes.

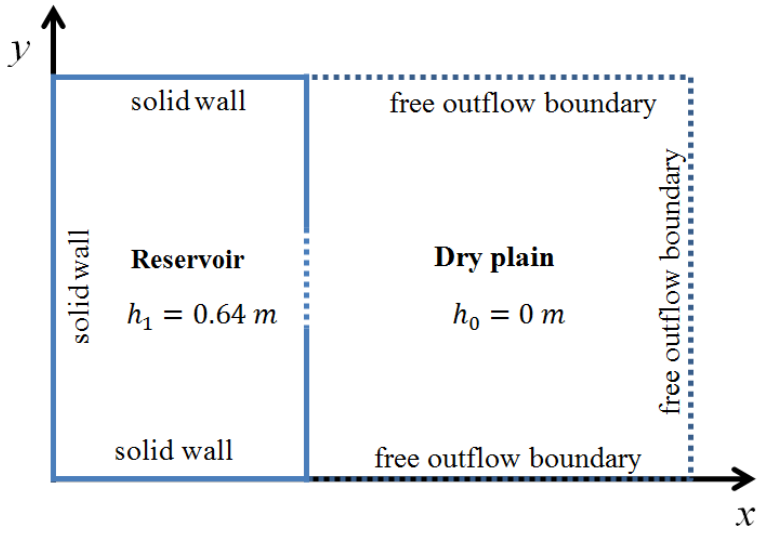

Figure 4.5 Initial conditions for the 2-D dam-break problem

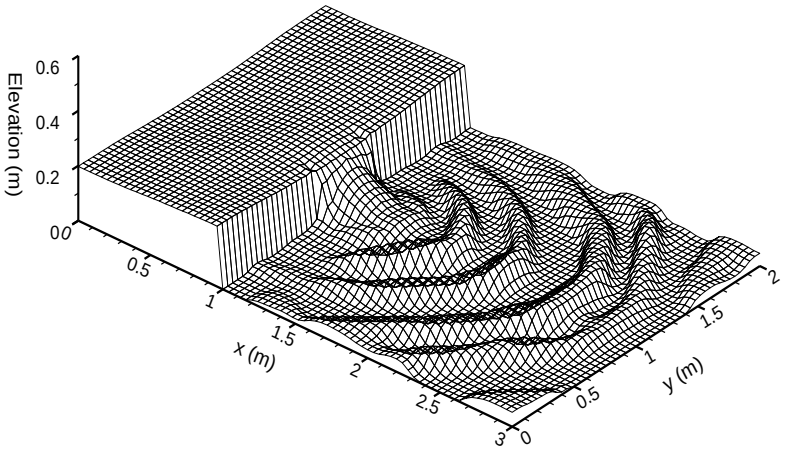

(a) $\beta = 0.6$

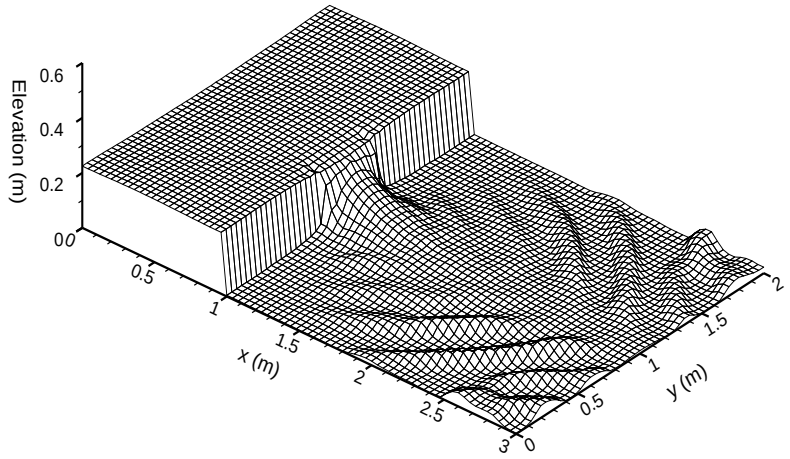

(b) $\beta = 0.8$

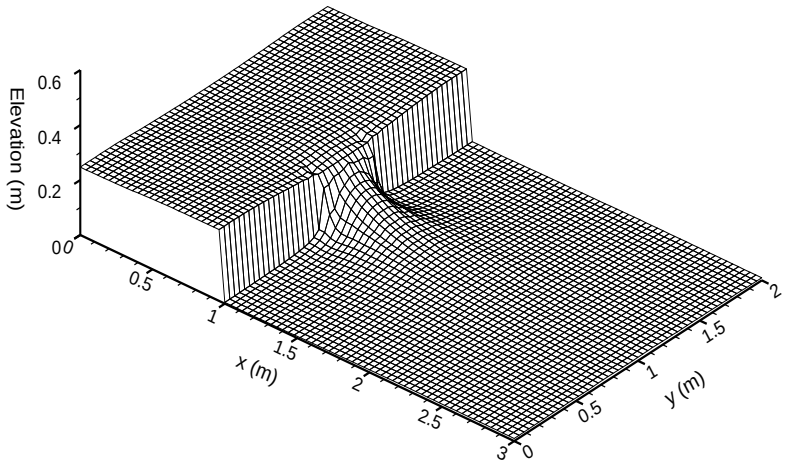

(c) $\beta = 1.0$

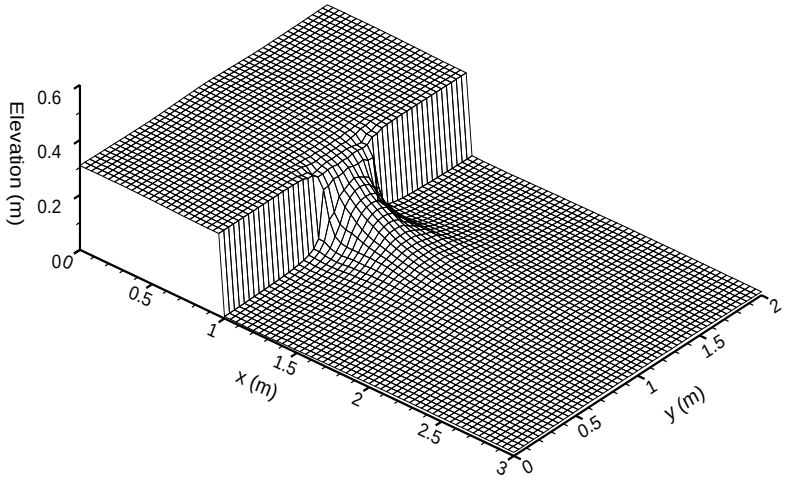

(d) $\beta = 2.0$

Figure 4.6 Snapshots of the water surface elevations for the 2-D dam-break simulation at 5 s. (a) $\beta = 0.6$; (b) $\beta = 0.8$; (c) $\beta = 1.0$; (d) $\beta = 2.0$

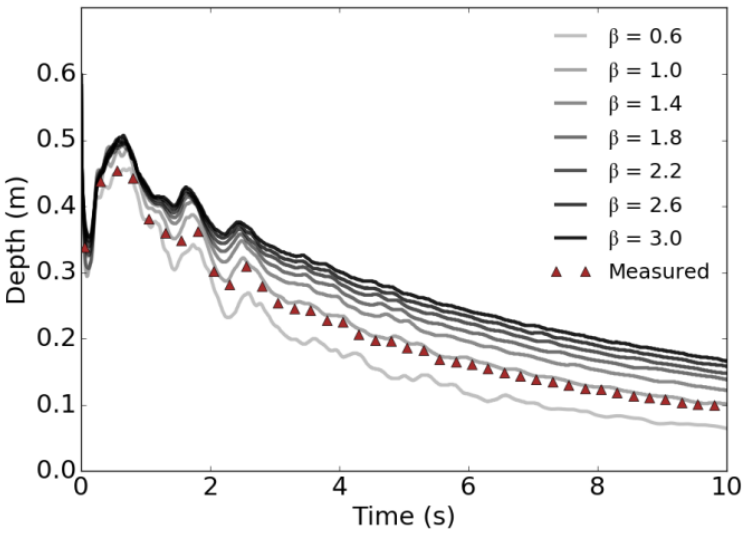

(a) $x = 1$ m, $y = 1$ m

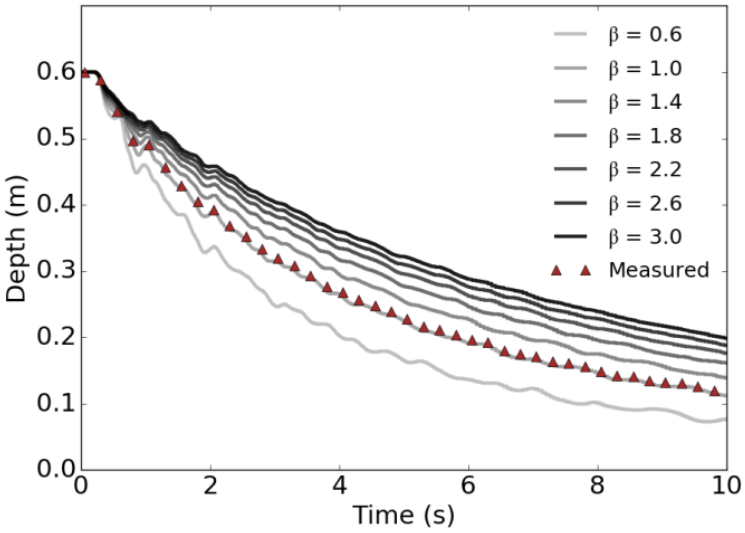

(b) $x = 0.2$ m, $y = 1$ m

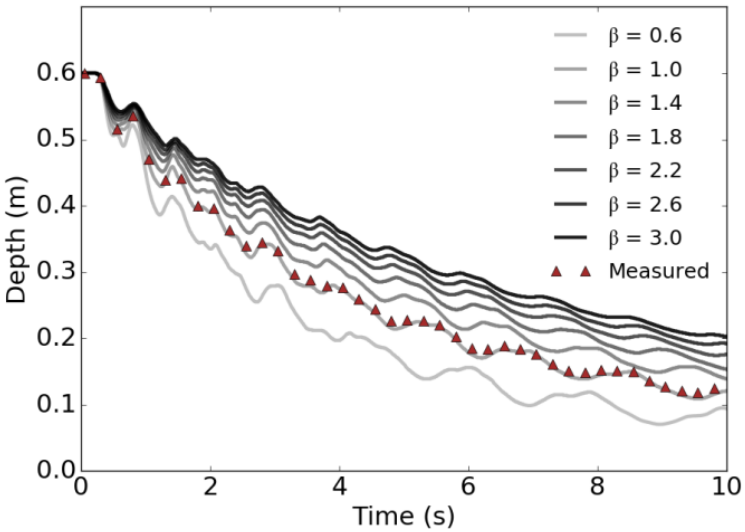

(c) $x = 0.48$ m, $y = 0.4$ m

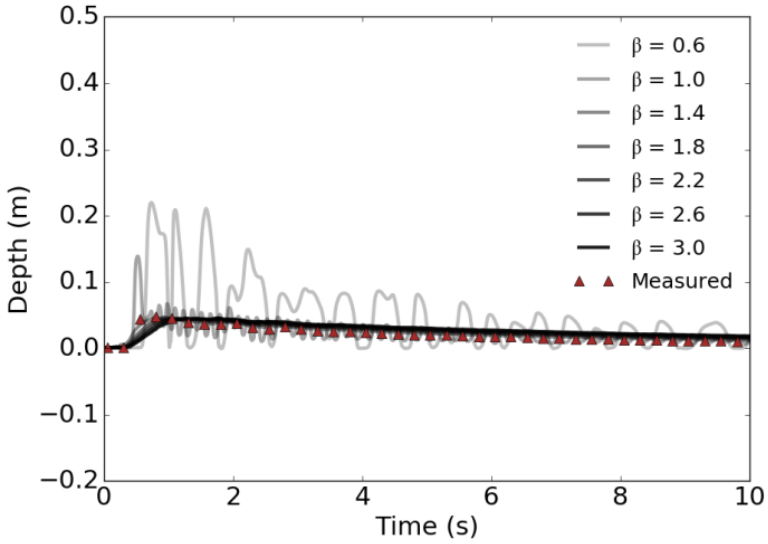

(d) x = 1.8 m, y = 1.44 m

Figure 4.7 Water depth variations at four locations in the 2-D dam-break simulation. (a) x = 1 m, y = 1 m; (b) x = 0.2 m, y = 1; (c) x = 0.48 m, y = 0.4 m; (d) x = 1.8 m, y = 1.44 m

Figure 4.6 shows four snapshots of the overall water surface variations with different values of β at 5 s after the dam failure. For all the results to be shown, grid independence studies have been conducted to ensure that proper grid convergence is achieved. Generally, it can be seen that the stability of predicted results increases with a larger β value. In the downstream region, the number of the bore waves grows as the β value increases, with the height of these waves decreasing. As shown in Figure 4.6 (a) and (b), the bore waves are allowed to move out of the domain, which verifies the validity of the transmissive boundary condition implemented in the simulation. In the upstream

region, the water depth decreases with the decrease of the β value, indicating higher flow rates from the reservoir to the floodplain.

Figure 4.7 compares the predicted and measured water depth histories at four locations, together with an ensemble of the results with different β values. The darker grey lines represent results with larger values of β. The value of β is increased from 0.6 to 3.0. Although there are no theoretical solutions available to this problem, the experimental data performed by Fraccarollo *et al*. (1995) are presented as triangle symbols in Figure 4.7 for comparison purposes. For the point located at (x = 1 m, y = 1 m), as shown in the figure 4.7 (a), the water depth starts at 0.6 m and then fluctuates between 0.3 m and 0.5 m. The numerical oscillations are more obvious with the decrease in the β value. Similar results are found in point (x = 0.2 m, y = 1.0 m) and point (x = 4.8 m, y = 1.4 m). For the two points, as seen in Figure 4.7 (c) and (d), the water depth starts at 0.6 m and then decreases gently with time. It can be seen that a higher β value not only prevents the oscillations but also delays the drop of the water elevations. For the point located at (x = 1.8 m, y = 1.44 m), as shown in the Figure 4.7 (d), the water depth increases to about 0.04 m at the first second and then slowly drops to the initial level. The numerical oscillations are most pronounced in the results predicted by the value of β lower than 1.0. In short, two features are obvious in these plots. One is that a higher β value prevents oscillations as previously noted. The measured data is close to the numerical results when the value of β is close to 1.0. Numerical oscillations are most pronounced in the result for the point located at the downstream region when the value of β is relatively small, as shown in Figure 4.7 (d), while the largest β value produces the smoothest curve. The second feature is that the

predicted water depth in the reservoir increases with the growth of β. Differences in the simulated water depth are biggest at point (x = 1 m, y = 1 m), up to 0.18 m, while this difference is smallest at point (x = 1.8 m, y = 1.44 m), only a 0.02 m difference over the range of β from 0.0 to 2.0.

4.2 Steady flow over frictional bed

The flow conditions considered in this section are similar to those that might occur in mountain rivers. In this situation, the flow rate changes rapidly under several transitions between subcritical and supercritical regimes. Therefore, it is also a severe test for numerical schemes.

4.2.1 1-D case

The scenario considered here was the trans-critical flow over an irregular channel bed. Figure 4.8 shows the topography of the channel bottom, with the exact bed coordinates given in Tseng *et al.* (2004). In this case, the bed profile was unchanged in the direction normal to the page to provide a 1-D analysis. The total length of the channel was 1600 m, with a grid size of 8 m. The Manning roughness coefficient considered here was 0.033 $s/m^{1/3}$. A constant unit-width-discharge of either 1.18 m^2/s or 0.59 m^2/s was imposed at the upstream boundary and the water depth was fixed at the end of downstream at 0.42 m. The conditions of the flow are similar to what might arise in a mountainous river, where the terrain is complex and varied. The flow over this kind of bed profile varies rapidly with several transitions between

sub-critical and super-critical regimes so that the case is a challenging test for numerical schemes.

Figure 4.8 compares the predicted water surface elevations and respective Froude numbers between the two numerical models. In Figure 4.8 (a), the Froude number is mostly less than unit when β is set to be 1.0 and the flow rarely experiences supercritical flow. The two models predict almost identical results. However, differences are quite noticeable for the case in which β is set to be 2.0. As shown in Figure 4.8 (b), the notable discrepancies are found at a few supercritical locations. For example, at 480 m, 1080 m and 1350 m and other locations when the Froude number exceeds 1.0, the two models give different results. Some oscillations appeared at these positions in the ADI model's results, indicating its lack of shock-capturing capability, while results of the TVD model do not demonstrate these oscillations. Hence, the increase in β value promotes the generation of spurious oscillations in ADI modelling, which is opposite to the finding previously obtained for the frictionless case study.

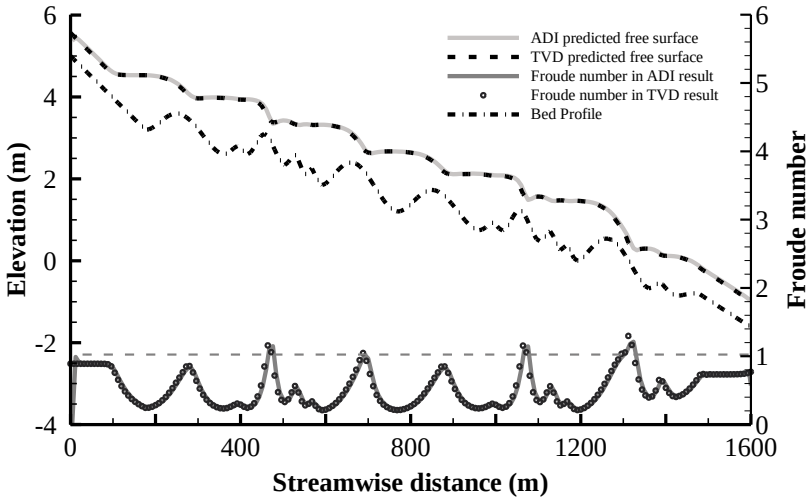

(a) $\beta = 1.0$

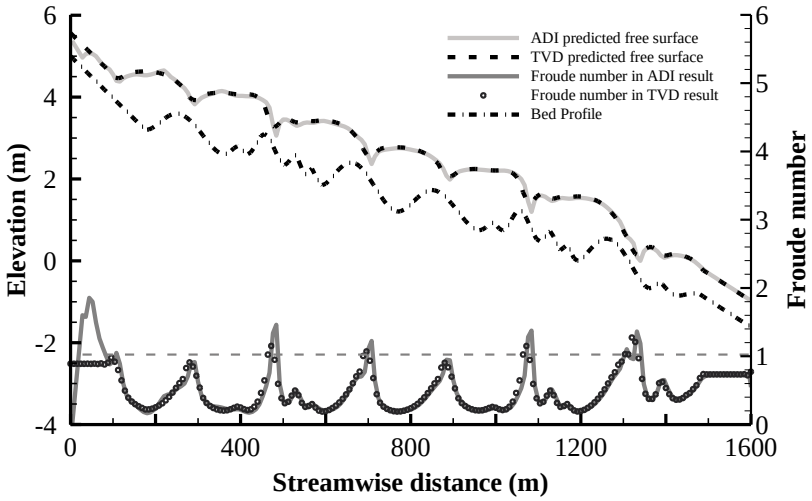

(b) $\beta = 2.0$

Figure 4.8 Trans-critical flow over an irregular channel bed. (a) $\beta = 1.0$; (b) $\beta = 2.0$

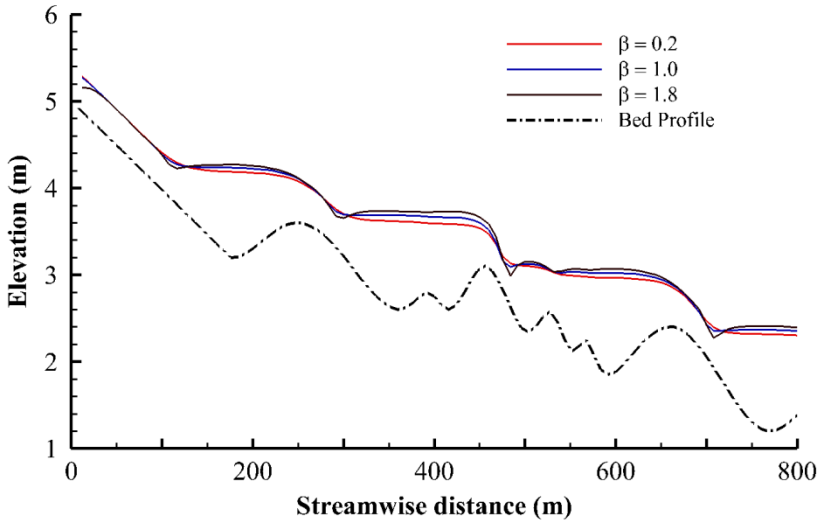

(a) Predicted by ADI model

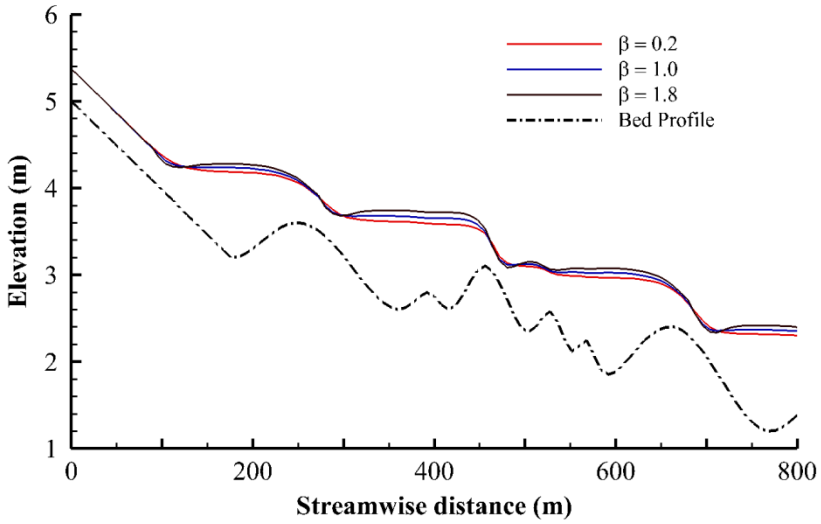

(b) Predicted by TVD-MacCormack model

Figure 4.9 Trans-critical flow over an irregular channel bed with unit-width-discharge being 0.59 m^2/s

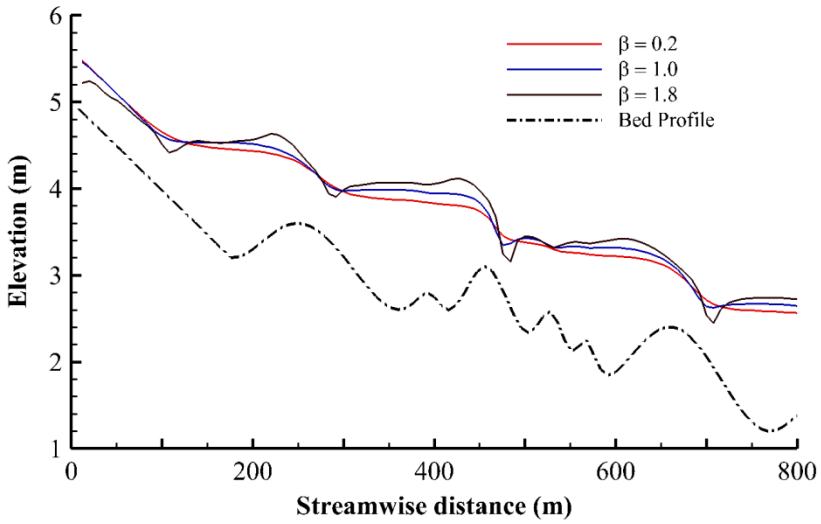

(a) Predicted by ADI model

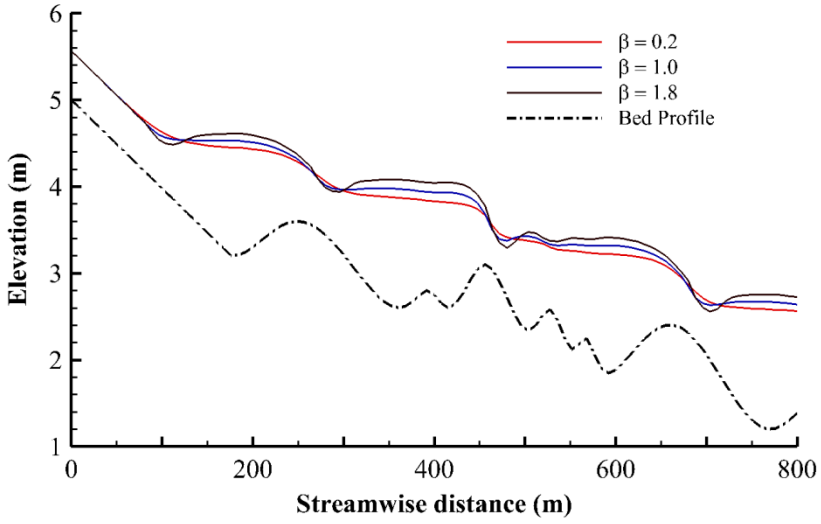

(b) Predicted by TVD-MacCormack model

Figure 4.10 Trans-critical flow over an irregular channel bed with unit-width-discharge being 1.18 m^2/s

Figures 4.9 and 4.10 show the magnitude of a range of water elevations predicted by the two models corresponding to three different β values. The comparison of the two figures can also reveal how different unit-width discharges lead to the different behavior of each model. In general, the water elevations predicted by the ADI model are sensitive to the varying β value in terms of the oscillation generation, apart from the change in the average water levels. With the increase of β, noticeable spikes in predicted water elevations occur at the steep falls of the riverbed. Oscillations are most pronounced in the results when β is 1.8 in the current study. This indicates that the reduction of β value can improve the computational stability effectively and inhibit the unwanted oscillations in the ADI model. Another general pattern is that a smaller β value results in a lower water depth in the simulation and a larger flow rate leads to bigger water depth variation. For example, the larger β results in more significant spurious oscillations at x = 480 m and positions near the upstream boundary, which can be seen in Figure 4.10 (a). When the unit-width discharge is 0.59 m^2/s, the water depth at 400 m increases by 0.13 m with the β ranging from 0.00 to 1.80. At the unit-width discharge of 1.18 m^2/s, the water depth at 400 m increases by 0.21 m with the β ranging from 0.00 to 1.80.

Unlike the unsteady flow over a frictionless bed studied in the previous section, where the fluid inertia is balanced by the water surface gradient, the main influencing factors are bed friction and the water surface gradient in steady flow over a frictional bed. Because a larger β value generally leads to a larger velocity, which then leads to a larger impact of bed friction, the water

surface gradient should be increased to overcome the bed friction, which attributes to the increased water level as β increases in Figure 4.9 and 4.10.

4.2.2 2-D case

4.2.2.1 Study site and data availability

The 2-D test case considered in this section is based on the real-world terrain. Boscastle is a small fishing port in Cornwall, UK, situated on the intersection of the River Valency and River Jordan, which continues into the Celtic Sea, as shown in Figure 4.11. The port's location and regional climate have left Boscastle inherently vulnerable to flooding. Among notable floods that occurred in the past few decades, the 2004 flood was the most severe flood ever recorded by the village (Roseveare and Trapmore, 2008). It was estimated that the flood event in 2004 had only a 1 in 400 years chance of recurring. There are three factors that exacerbated the 2004 flood in Boscastle. Firstly, the capacity of the River Valency was limited. The capacity of the River Valency was designed to only against a 1 in 10 chance of the recurring storm so that the river boundaries are exceeded detrimentally. Secondly, the channel and bridge were blocked by obstructions. Trees at the upstream of the village and cars from the eastern car park were washed away and carried into the river channel. These debris and cars filled the river and became jammed at the central bridge. The debris prevented any further flow underneath the bridge, which was therefore diverted over the top of the bridge and into the village centre. Thirdly, the channel's capacity was further reduced by the sediment from the upstream. The storm has resulted in the deposition of a large amount of sediment from upstream. The high flows moved the sediment downstream of the River Jordan

outfall. Last but not least, the catchment of Boscastle has a very steep topography. There was only a very thin layer of soil above impermeable rock in the catchment. These factors together lead to huge and rapid runoff of any rainfalls, making the village very vulnerable to flash floods, especially in strong and short-term storms.

HR Wallingford has undertaken extensive data collection from photos, observations and residual evidence of the flood that occurred in 2004. Due to the wealth of evidence availability, this event has been an excellent study case for assessing flood simulation software (Wallingford, 2005). With the help of the Environment Agency, a digital elevation model (DEM) was extracted for the Boscastle area. The background digital terrain model was obtained by filtering out the buildings and vegetation of the LiDAR elevation data, which is a laser-based technology. Due to low water levels in both rivers during normal conditions, the DEM specifies an initial water depth and flow velocities only at the mouth of River Valency by the Celtic Sea. Then, buildings and bridges were added using geographic information system (GIS) technology software according to the ordinance survey maps. GIS is a special information system in which the data source is a spatially distributed function and process database used to collect, store, retrieve, analyze and display geographic data. The key element of information is its position relative to other geographic features and objects (Shami, 2002). It combines the spatial location and its corresponding various information.

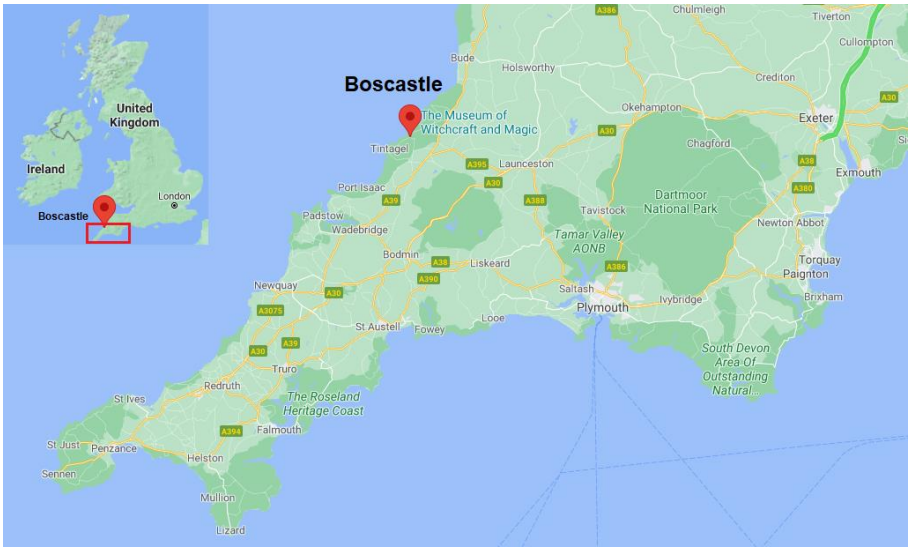

(a) Geographic location of Boscastle village (photo source: Google map)

(b) Aerial view of Boscastle village, superimposed with the centerlines of the River Valency (running leftwards) and River Jordan (running upwards)

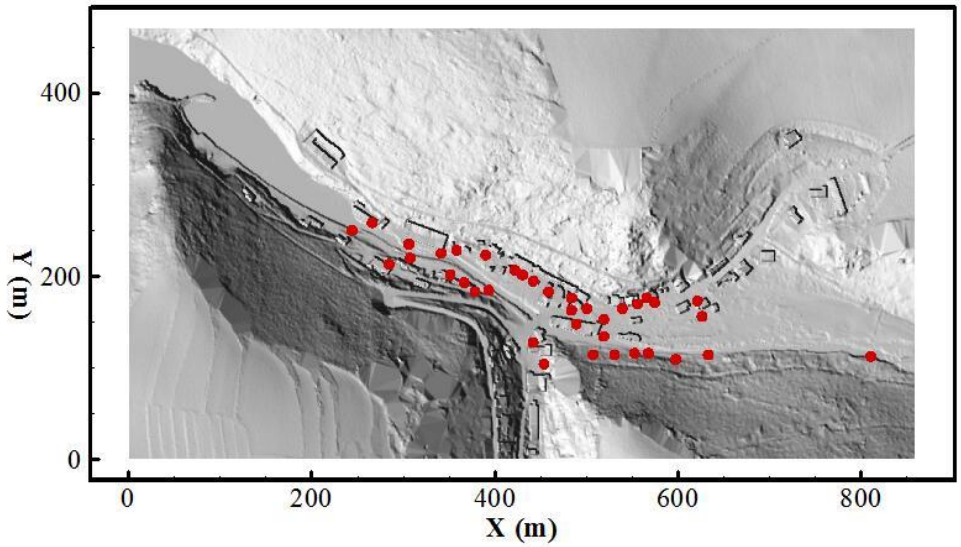

(c) DEM of Boscastle village and the locations of gauging stations

Figure 4.11 Geographic information of Boscastle village

During the 2004 floods, the bridge openings were blocked by debris and cars; thus, it would be reasonable to include only the top of the bridge deck in the DEM. The underwater bathymetry was merged with the DEM according to the cross-sectional drawings provided by the UK engineering consultancy company, the Halcrow Group Ltd. The detailed procedure of generating the DEM suitable for flood modelling is given by Tuckley (2010). The domain was discretised into 860 by 470 grid cells. The hydrological analysis gave the peak discharges at the upstream ends of the River Valency and the River Jordan to be 160 m^3/s and 19 m^3/s, respectively. The water level at the Celtic Sea boundary was specified to be 3.5 m. A constant Manning coefficient of 0.03 $s/m^{1/3}$ was set for the domain.

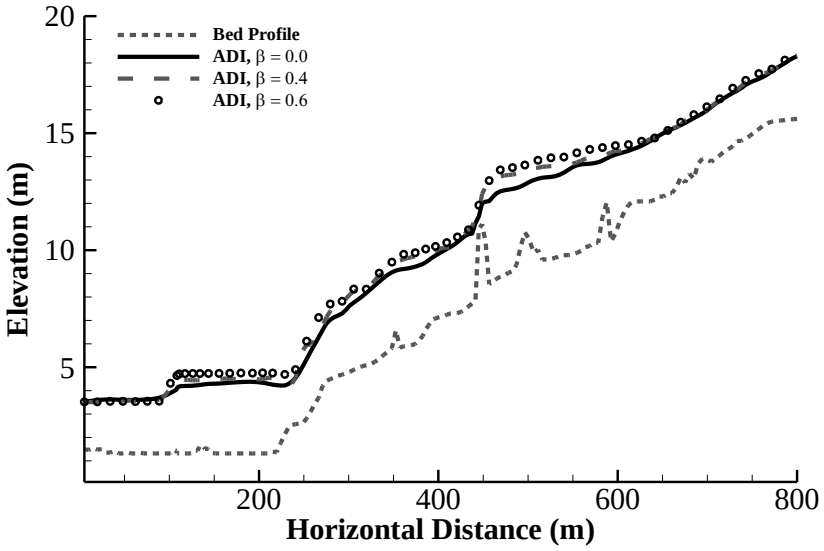

(a) Water surface profiles along the centerline of River Valency

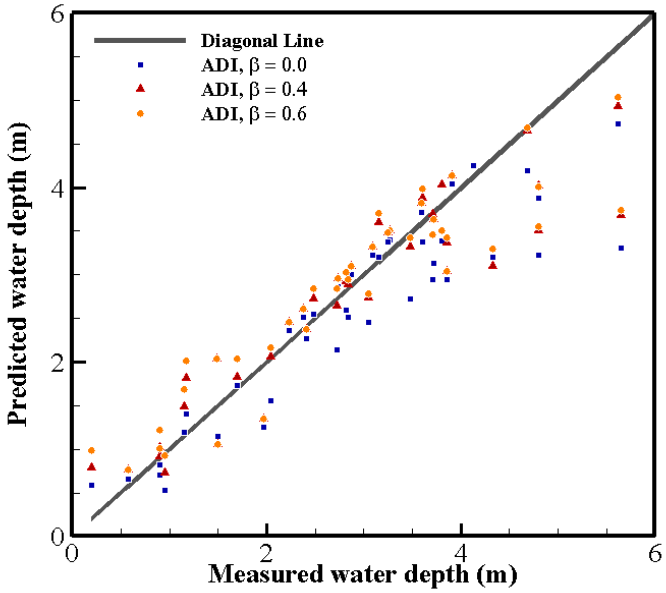

(b) Comparison between the modelled and surveyed water column depths

Figure 4.12 Water surface elevations in the Boscastle flood, 2004

4.2.2.2 Results and discussion

The two-hour flood evolution process was simulated for the urban flood case in Boscastle. For all the results to be shown, grid independence studies have been conducted to ensure that proper grid convergence is achieved. During this period, the flood went through the main channel and several tributaries and finally reached the steady flow state. Because the 2004 flood flow is rapid and contains steep variations, the ADI model cannot produce stable results without using a reduced value of β. Successful simulations were achieved with β values of 0.0, 0.4 and 0.6. At higher β values, the simulation terminated in the middle of the computation. The flow through the river is illustrated by plotting the water level and bed level variations along the river centreline, as shown in Figure 4.12 (a). It is clear that a larger β value results in a higher predicted water surface elevation. Such a trend coincides well with the 1-D case study in this section, confirming that, when modelling steady and frictional flow phenomena, a reduction in the value of β can effectively suppress the generation of unwanted oscillations in the numerical results of the ADI model. However, this is at the cost of reducing the accuracy of the numerical model, as the water elevation will be underpredicted. Figure 4.12 (b) presents the comparison between the modelled and surveyed water column depth. There are thirty-eight measured locations provided by HR Wallingford. These locations have been tested on each model for the maximum water surface elevation that they experienced throughout the flood duration. The diagonal line indicates any values for which the model is correct; any results to the left of this line are conservative and over-estimate the water level experienced; any values to the right of this line under-predict the actual water

level. In general, the ADI results with a larger β value generally agree better with the surveyed data.

4.3 Unsteady flow over frictional bed

The findings in Section 4.2 are seemingly opposite to those in the Section 4.1 because of different flow conditions. This implies that the Boussinesq coefficient should be adjusted either up or down in order to eliminate computational oscillations in the ADI models, depending on the flow situations. Except for the high-frequency oscillations, the ADI and TVD models predict similar overall trends in water depth and velocity variations, which provides reassurance as to the correctness of the present simulations.

4.3.1 Study site and data availability

The final case considered here is based on an actual flood that occurred in the city of Glasgow, Scotland, UK on 30 July 2002. In this case, the flow is unsteady, and the bed is uneven and frictional. The 2-D ADI model is applied to simulate the flood event over a 1.0 km × 0.4 km urban catchment. A 1 m resolution LiDAR survey was undertaken by Infoterra Ltd, which is a provider of geospatial products. The surveyed data were processed to leave only the bare earth information and then modified according to the Ordnance Survey Mastermap that defines the building locations, road network and land-use types. A single set of friction coefficients was used, with the Manning coefficient of roads and vegetation being 0.015 s/m$^{1/3}$ and 0.05 s/ m$^{1/3}$, respectively. Flooding at this site was caused by a burst pipe near the north-east corner, which can be seen in Figure 4.13 as Q_{IN}. The detailed information

and data on the area as well as the treatment of the boundary conditions for this case can be found in Hunter et al. (2008). In order to demonstrate the changes of water level clearly, four reference points are selected, representing the vicinity of the pipe burst, the main road, the minor road and the low-lying region, respectively. The exact locations of the reference points denoted G1, G2, G3 and G4 are marked in Figure 4.14, which is a contour map of the ground elevations.

(a) Geographic location of Glasgow (photo source: Google map)

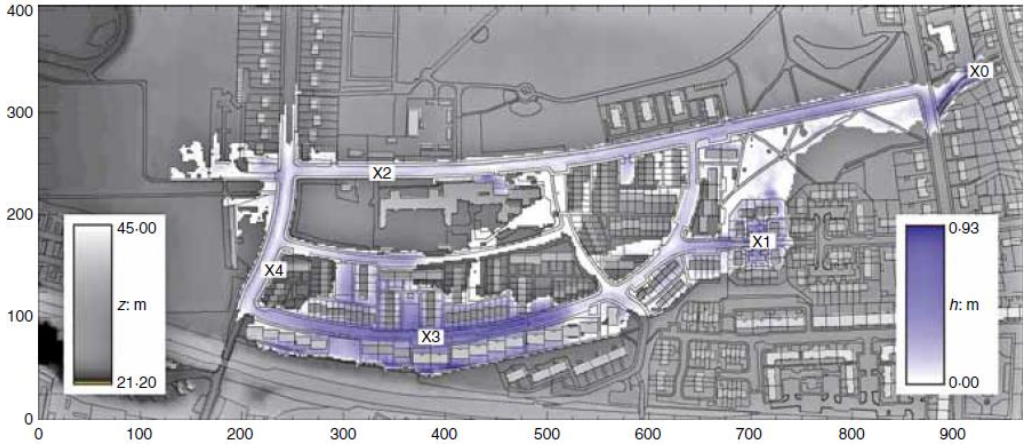

(b) Map of the study site with building and road topology (Hunter et al. 2008)

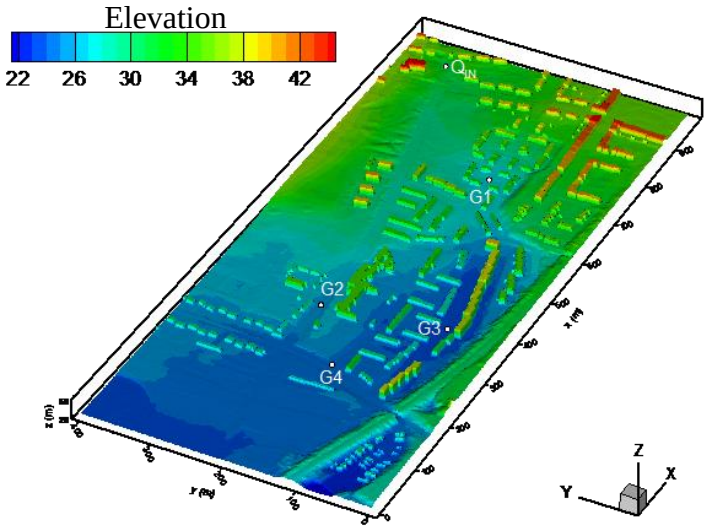

(c) Ground elevations of an urban area in Glasgow and the locations of inflow and gauging stations

Figure 4.13. Geographic information of computational domain in Glasgow

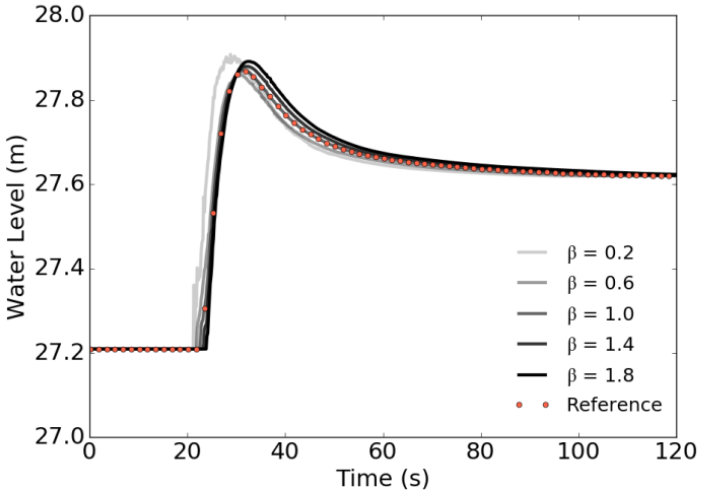

(a) Point G1

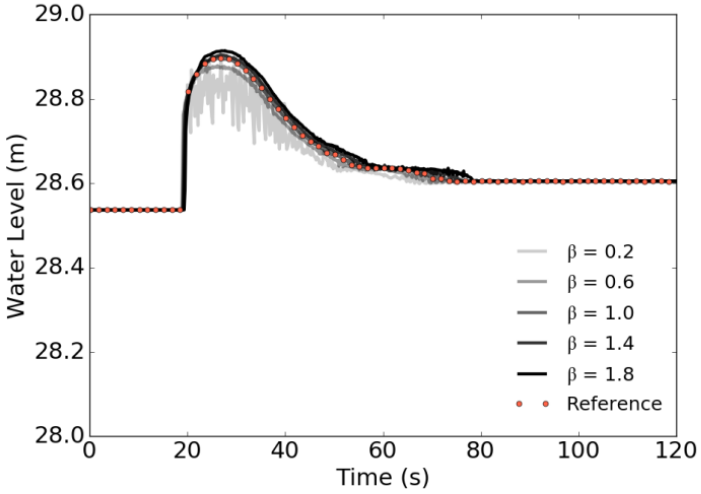

(b) Point G2

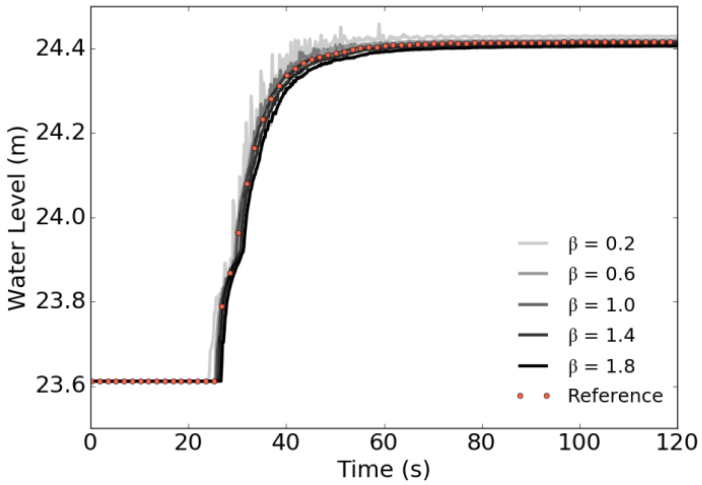

(c) Point G3

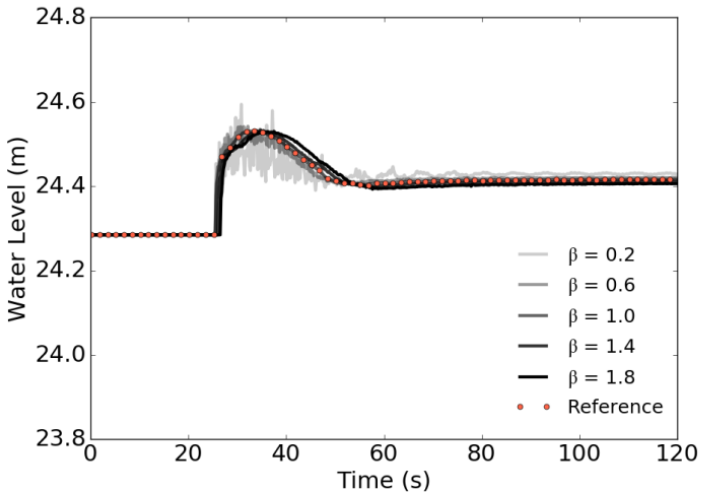

(d) Point G4

Figure 4.14 Water elevation variations at 4 gauges with β ranging from 0.2 to 1.8. (a) Point G1; (b) Point G2; (c) Point G3; (d) Point G4

4.3.2 Results and discussion

Figure 4.14 presents the time series of water elevations predicted by the ADI model at the four gauging points. To validate the present simulations, the results obtained by the shock-capturing numerical scheme in Hunter et al. (2008) are also plotted in Fig. 13 as references. Three conclusions can be drawn from observing this dataset.

Firstly, spurious oscillations are obvious when β is close to zero, especially at points G2 and G4 where shallow, high-velocity and convergent flow happens. In contrast, the curves with larger β are relatively smooth, indicating that a large β value may help mitigate the inherent instability of the ADI model in this case study. This finding corresponds well with that observed in the case studies of unsteady flow over frictionless beds. Secondly, a general pattern can be summarised in terms of the arrival time of flood waves. The smaller β value always predicts an earlier arrival of the flood wave, especially for the points G1 and G3, where water accumulates giving rise to large water depths in the course of the simulation. Although these differences in the arrival time are only of the order of 3 or 4 min, they can be deemed significant given the short duration of the flooding event. Thirdly, the peak flood depth is not sensitive to the value of β. Differences in the maximum predicted water elevation are only obvious for point G2, up to only 8 cm when the value of β ranges from 0.2 to 1.8. Hence, the variation in β for this test case does not significantly alter the water depth. The inundation extent is another important parameter when assessing the flood.

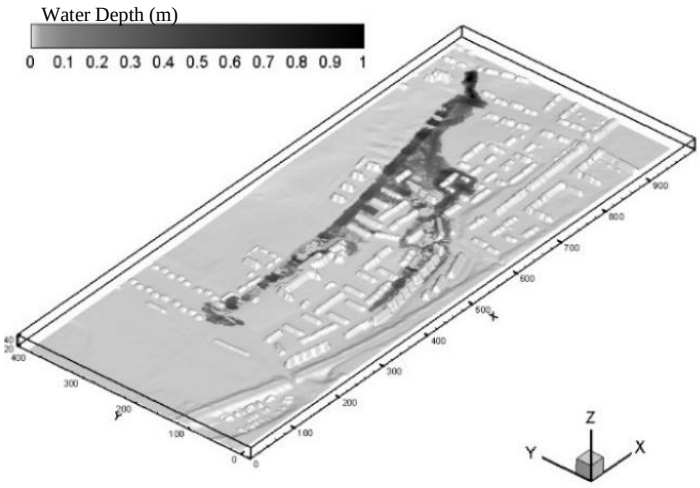

(a) $\beta = 0.2$

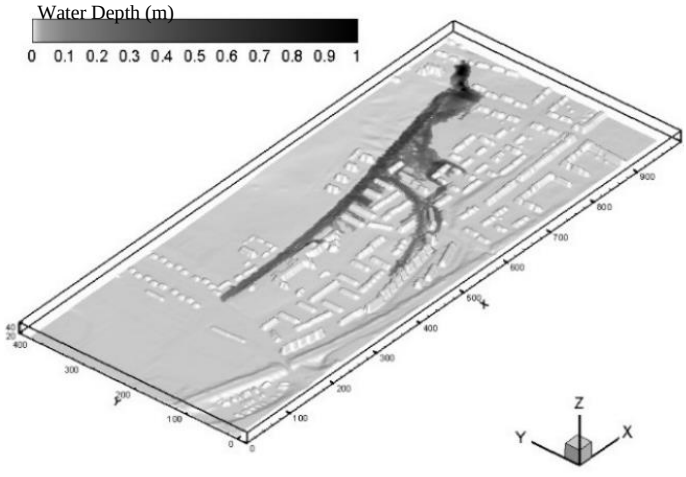

(b) $\beta = 2.0$

Figure 4.15 Inundation extent development predicted by the ADI model at 24 min. (a) $\beta = 0.2$; (b) $\beta = 2.0$

Figure 4.15 depicts the inundated areas of the unban catchment in the backdrop of the three-dimensional topography 24 min after the initiation of the flood. At this moment, the flood has spread through the main roads and streets, reaching the lower part of the region located at about x = 180 m. Water travels mainly along roads and streets, since they have a relatively small roughness value and a low ground level compared with the neighbouring land features. Some rather fragmented arrangements of the wet and dry patches are notable in Figure 4.15 (a), with a smaller value of β. It may therefore be said that even small numerical oscillations may have a large effect on shallow flow depths, thus resulting in a fragmented pattern of inundation. As β increases, these anomalies disappear and the inundation extent gradually decreases, as shown in Figure 4.15 (b). Such phenomena are correspondingly quantified in Fig. 4.15, where the impact of modifying β on the inundated area is shown in detail at 4 instants. It implies that the flood front propagation slows down and the flooded area gradually reduces as the value of β increases.

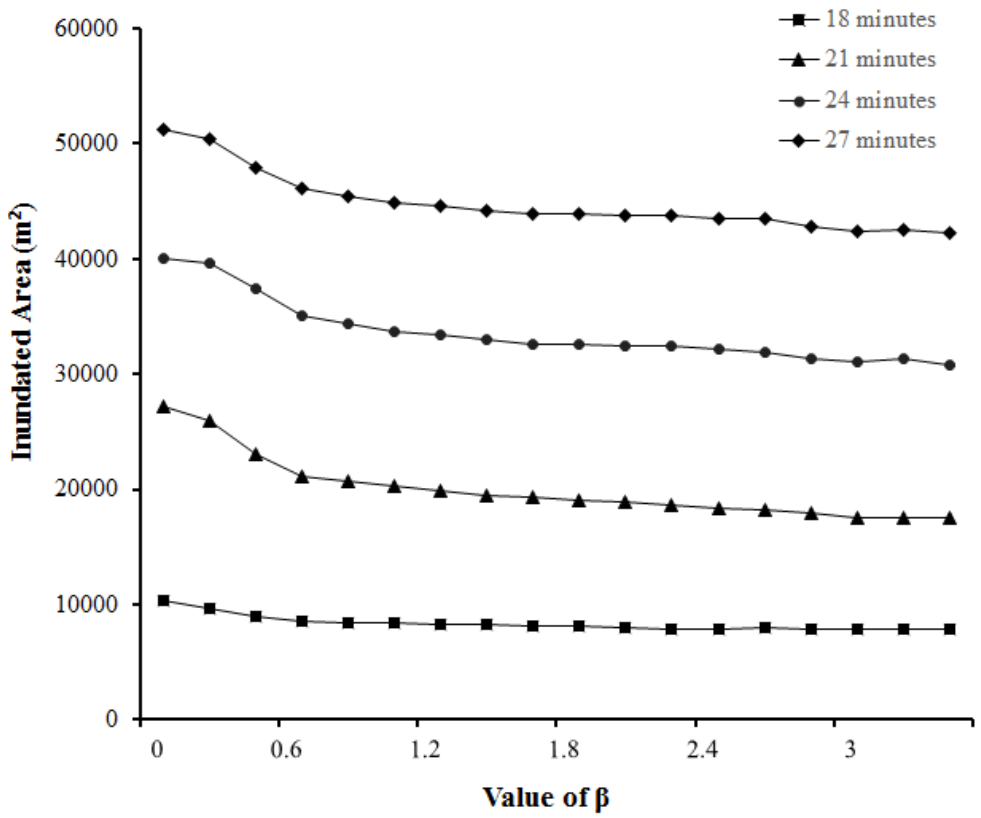

Figure 4.16 Sensitivity of inundated areas predicted by the ADI model

Over a frictionless bed, the inundated area is overpredicted for increased values of β. The reverse occurs when the bed friction is significant, as seen in Figures 4.15 and 4.16. For unsteady flow over a frictional bed, the fluid inertia, water surface gradient and bed friction are all potentially important factors. As an increase in β is accompanied by increased velocity and impact of bed friction, a larger water surface gradient will then be required to overcome the bed friction. With a fixed water level difference to drive the flow, a larger β value may counterintuitively lead to slower propagation of the flood front over a frictional bed.

4.4 Chapter summary

In this chapter, the numerical treatment is comprehensively examined to access the stability and accuracy of the ADI scheme with modified Boussinesq coefficients. While TVD-MacCormack model is in no doubt a more advanced method, the traditional ADI scheme is still widely used in many existing commercial software applications. Consequently, a detailed knowledge of the impacts of modifying the Boussineesq coefficients can be used to see whether ADI scheme can be improved in a simple way and is therefore useful in many practical industrial applications.

A comparison between the ADI and TVD-MacCormack models is first made concerning the 1-D and 2-D dam-break floods over frictionless and flat beds. The results suggest that using a large β value can enable the ADI models to overcome the inherent instability difficulty in simulating rapid dam-break flows. It is also found that increasing the value of β increases the propagation speed of flood waves when modelling unsteady flows over a frictionless bed. However, it tells a different story in the steady flows with a frictional bed. The results in these situations suggest that the amplitude of the spurious oscillations reduces with the decrease of the Boussinesq coefficient. The steady water surface elevation becomes lower with a smaller β value. Finally, the simulation of flash floods event over a real-world urban terrain is studied. The results indicate that the increase in the Boussinesq coefficient can significantly reduce the amplitude of the numerical oscillations in the ADI simulations. The inundated area gradually reduces as the coefficient increases. These results show the complicated relationship between the β coefficient and the computational results, suggesting that adjusting the value of β to stabilise the

ADI scheme is not an ideal approach as it compromises the accuracy. Note that apart from using different values for the Boussinesq coefficient, some other schemes exist in conjunction with the ADI scheme. For example, instead of using a constant value, a variable Boussinesq coefficient could also be used depending on the magnitude of local flow velocity gradients. Additionally, the Boussinesq coefficient may be even eliminated (equal to 1) if other stabilisation methods could be devised.

Chapter 5

Solute transport modelling

For the modelling of solute transport processes, obtaining the hydrodynamic features of the flow fields is a prerequisite. The hydrodynamic features, such as water elevations and velocity components, are regarded as the input conditions for the solute transport modelling. As mentioned in the chapter 2, many modern numerical methods have been established to model solute transport processes. Most of the research is based on Eulerian approaches to solve the standard advection-diffusion equation using finite-difference, finite-element or finite-volume techniques. However, these grid-based methods have proven to be deficient in addressing steep concentration gradients and tend to produce numerical diffusion. By contrast, the Lagrangian approach can usually yield an accurate estimation. Nowadays, thanks to the dramatic progress in the quality and speed of computers, the computational

price for the Lagrangian approach could be well paid. Compared with Euler methods, the Lagrangian methods can be regarded as an alternative to the simulation of complex phenomena, where high contamination gradients are involved. For the solute transport simulations, the Lagrangian methods are efficient when the contaminants occupy only a small part of the calculation domain. Therefore, the Lagrangian approach is more attractive for the water quality modelling. This chapter presents the governing equations of the solute transport processes and the Lagrangian random walk model is explained in detail.

5.1 Depth-averaged advection-diffusion equation

The governing equation of solute transportation in water bodies is the advection-diffusion equation (Gresho & Sani 1998). Advection is the transportation of a substance by a fluid due to the fluid's bulk motion. In this process, it is assumed that particles of the solute exactly follow the shallow flow. Diffusion is the process whereby solute transports from higher concentration to lower concentration in flow due to random movements. It is assumed that the diffusive substances would not affect the motion of flows. In other words, the flow field is independent of the existence of the diffusive materials. With these assumptions, the conservation of solute mass in the 2-D form is presented as:

$$\frac{\partial(sH)}{\partial t}+\frac{\partial(usH)}{\partial x}+\frac{\partial(vsH)}{\partial y}=\frac{\partial}{\partial x}\left(HD_{xx}\frac{\partial s}{\partial x}+HD_{xy}\frac{\partial s}{\partial y}\right)+\frac{\partial}{\partial y}\left(HD_{yx}\frac{\partial s}{\partial x}+HD_{yy}\frac{\partial s}{\partial y}\right)+q_s \quad [5.1]$$

where t is time; s is the depth-averaged concentration of the solute; H is the water depth; u and v represent the velocities along x and y directions respectively; q_s is the sources term of the governing equation, representing the increase ($q_s > 0$) or decrease ($q_s < 0$) in the total amount of the solute; D_{xx}, D_{xy}, D_{yx} and D_{yy} represent the dispersion-diffusion tensor of depth-averaged mixing in Cartesian coordinates. The relationship between the streamwise-transverse system and Cartesian coordinate can be expressed as:

$$D_{xx} = D_s \cos^2\theta + D_t \sin^2\theta \quad [5.2]$$

$$D_{xy} = D_{yx} = (D_s - D_t) \sin\theta \cos\theta \quad [5.3]$$

$$D_{yy} = D_s \sin^2\theta + D_t \cos^2\theta \quad [5.4]$$

$$\text{where } D_s = \varepsilon_s H u_*,\ D_t = \varepsilon_t H u_* \quad [5.5]$$

D_s and D_t are the streamwise and transverse diffusion coefficients; ε_s and ε_t are two dimensionless constants representing streamwise dispersion and transverse dispersion, respectively. $\theta = arctan(v/u)$ is the angle between the direction along the x-axis and the direction of the local flow. The shear velocity u_* is expressed as Equation [5.6] using Chézy coefficient C:

$$u_* = \frac{\sqrt{g}}{C} \cdot \sqrt{u^2 + v^2} \quad [5.6]$$

5.2 Depth-averaged random walk method

5.2.1 Equation reformation

In this paper, the depth-averaged advection-diffusion equation is recast in a new form that utilises a consistent particle-tracking algorithm. A new concentration variable, $S = sH$ is introduced. Then, the new form of the equation can be written as:

$$\frac{\partial S}{\partial t} + \frac{\partial (US)}{\partial x} + \frac{\partial (VS)}{\partial y} = \frac{\partial^2 (D_{xx} S)}{\partial x^2} + 2\frac{\partial^2 (D_{xy} S)}{\partial x \partial y} + \frac{\partial^2 (D_{yy} S)}{\partial y^2} \quad [5.7]$$

$$U = u + \frac{\partial D_{xx}}{\partial x} + \frac{\partial D_{xy}}{\partial y} + \frac{D_{xx}}{H}\frac{\partial H}{\partial x} + \frac{D_{xy}}{H}\frac{\partial H}{\partial y} \quad [5.8]$$

$$V = v + \frac{\partial D_{yy}}{\partial y} + \frac{\partial D_{xy}}{\partial x} + \frac{D_{yy}}{H}\frac{\partial H}{\partial y} + \frac{D_{xy}}{H}\frac{\partial H}{\partial x} \quad [5.9]$$

The source term q_s in the previous equation is neglected in the new form. S is considered as a probability density function. U and V in the Equations [5.8] and [5.9] represent the modified advective velocities. This depth-averaged random walk model is then performed by advection and diffusion transport process for each time step in the following content.

5.2.2 Advective process

Prior to the solution of the transport equation, the flow field should be solved first. For most shallow flow solvers, water depths and velocities are stored on discrete points in the computational domain. We assume that the

water depth, flow velocity and dispersion-diffusion tensor are stored on Cartesian grid. To reconstruct a continuous variation of the flow field over the computational domain, we adopt bilinear interpolation in space. Taking the velocity at a point $P\ (x,\ y)$ for example, the value is interpolated from the velocities at four nearby grid points $Q_{i,j}$, $Q_{i+1,j}$, $Q_{i,j+1}$, and $Q_{i+1,j+1}$, as illustrated in Figure 5.1.

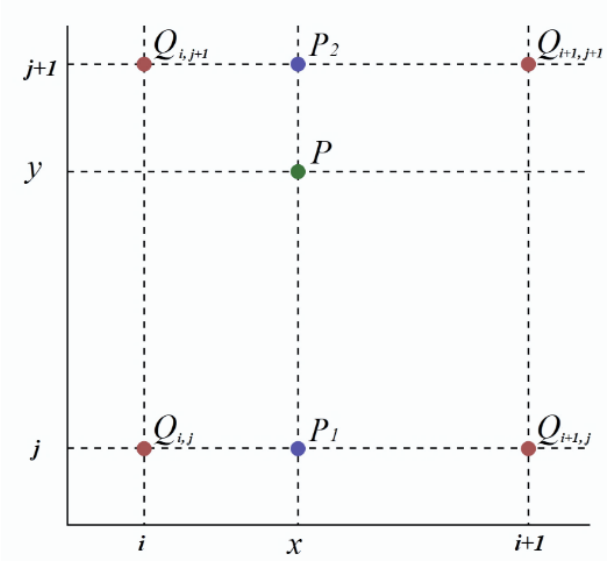

Figure 5.1. Bilinear interpolation

Three steps are involved in the spatial interpolation procedure. Firstly, we determine (U_{p1}, V_{p1}) on the southern side of the cell at a position aligned with $Q_{i,j}$ and $Q_{i+1,j}$ as follows:

$$U_{p1} = U_{i,j} + (U_{i+1,j} - U_{i,j})(\frac{x_p - x_{i,j}}{x_{i+1,j} - x_{i,j}}) \quad [5.10]$$

$$V_{p1} = V_{i,j} + (V_{i+1,j} - V_{i,j})(\frac{x_p - x_{i,j}}{x_{i+1,j} - x_{i,j}}) \quad [5.11]$$

Then, we determine (U_{p2}, V_{p2}) on the northern side of the cell at a position aligned with $Q_{i,j+1}$ and $Q_{i+1,j+1}$ as follows:

$$U_{p2} = U_{i,j+1} + (U_{i+1,j+1} - U_{i,j+1})(\frac{x_p - x_{i,j+1}}{x_{i+1,j+1} - x_{i,j+1}}) \quad [5.12]$$

$$V_{p2} = V_{i,j+1} + (V_{i+1,j+1} - V_{i,j+1})(\frac{x_p - x_{i,j+1}}{x_{i+1,j+1} - x_{i,j+1}}) \quad [5.13]$$

The third step involves the interpolation in the y direction, giving (U_p, V_p) as:

$$U_p = U_{p1} + (U_{p2} - U_{p1})(\frac{y_p - x_{i,j}}{y_{i+1,j+1} - y_{i,j}}) \quad [5.14]$$

$$V_p = V_{p1} + (V_{p2} - V_{p1})(\frac{y_p - x_{i,j}}{y_{i+1,j+1} - y_{i,j}}) \quad [5.15]$$

The new particle position after the advective transport process can be expressed by Equation [5.16] using the second-order iterative technique.

$$x^a = x^{old} + \bar{U}\Delta t,\ y^a = y^{old} + \bar{V}\Delta t \quad [5.16]$$

where $\bar{U}$ and $\bar{V}$ are the two velocity components used in calculating a particle's advective displacement in each time step. To increase the order of accuracy, they are taken to be the time-averaged velocity within each time step.

$$\bar{U} = \frac{1}{2}(U(x^{old}, y^{old}, t) + U(x^a, y^a, t + \Delta t) \quad [5.17]$$

$$\bar{V} = \frac{1}{2}(V(x^{old}, y^{old}, t) + V(x^a, y^a, t + \Delta t)) \quad [5.18]$$

5.2.3 Dispersion and diffusion process

Particles also undergo the dispersion and diffusion transport in each time step. The random streamwise and transverse velocities are calculated as follows.

$$U_s^d = r_s\sqrt{\frac{2D_s}{\Delta t}}, V_t^d = r_t\sqrt{\frac{2D_t}{\Delta t}} \quad [5.19]$$

where the subscripts *s* and *t* represent the streamwise and transverse directions, respectively. The superscript *d* represents the diffusion-related velocity components. The random numbers r_s and r_t are independent of each other and follow a normal distribution with a mean of zero and a standard deviation of unity. According to the principles of tensor transformation between coordinate systems, the diffusion-dispersion process corresponds to the extra velocity components in the original Cartesian coordinate system:

$$U_x^d = U_s^d \cos\theta - V_t^d \sin\theta \quad [5.20]$$

$$V_y^d = U_s^d \sin\theta + V_t^d \cos\theta \quad [5.21]$$

Finally, the new position of the particle can be calculated as:

$$x^{new} = x^a + U_x^d \Delta t \quad [5.22]$$

$$y^{new} = y^a + V_y^d \Delta t \quad [5.23]$$

5.2.4 Time advancement

When updating a particle's position and mass using the above method, only first order accuracy can be achieved. In the present implementation of the

random walk model, a second-order Runge-Kutta time integration method can be adopted. The time advancement from instant t to instant $t+\Delta t$ is carried out as follows:

$$x_p^{t+\Delta t} = x_p^t + \frac{1}{2}\Delta t(k_{11} + k_{12}) \quad [5.24]$$

$$y_p^{t+\Delta t} = y_p^t + \frac{1}{2}\Delta t(k_{21} + k_{22}) \quad [5.25]$$

$$m_p^{t+\Delta t} = m_p^t + \frac{1}{2}\Delta t(k_{31} + k_{32}) \quad [5.26]$$

$$k_{11} = \left(\frac{dx}{dt}\right)^t_{x_p,y_p},\ k_{21} = \left(\frac{dy}{dt}\right)^t_{x_p,y_p},\ k_{31} = \left(\frac{dm}{dt}\right)^t_{x_p,y_p} \quad [5.27]$$

$$k_{12} = \left(\frac{dx}{dt}\right)^{t+\Delta t}_{x_p+k_{11}\Delta t,y_p+k_{21}\Delta t} \quad [5.28]$$

$$k_{22} = \left(\frac{dy}{dt}\right)^{t+\Delta t}_{x_p+k_{11}\Delta t,y_p+k_{21}\Delta t} \quad [5.29]$$

$$k_{32} = \left(\frac{dm}{dt}\right)^{t+\Delta t}_{x_p+k_{11}\Delta t,y_p+k_{21}\Delta t} \quad [5.30]$$

This is a second-order accurate iterative scheme, meaning that the total accumulated error is on the order of $0(\Delta t^2)$.

5.2.5 Treatment of moving boundaries

The wetting and drying phenomena is common in environmental flows, especially in shallow waters with uneven bottoms. In the random walk model, a minimum water depth H_{min} is introduced, below which the bed is regarded

to be dry. The water depth at each particle's location is checked in each time step. If a particle is found to be on a dry bed, then the particle will be frozen to the position. The frozen particles are excluded in the advective and diffusive processes, but the reaction process is still considered on frozen particles. When the water depth is higher than H_{min}, the frozen particles are freed and then participate in the advective, diffusive and reactive processes.

5.3 Chapter summary

In this chapter, the governing equations of the solute transport are outlined. The 2-D advection-diffusion equations have been reformulated into the depth-averaged advection-diffusion equations. The depth-averaged model is then performed by advection and diffusion transport process for each time step. In the advective process, the bilinear interpolation is adopted in the random walk model as the input data for the flow field is solved by grid-based methods. In the diffusive process, the independent random numbers are introduced. The time advancement and the minimum water depth H_{min} for the moving boundaries treatment are explained in detail.

Chapter 5

Chapter 6

On the application of the depth-averaged random walk method to solute transport simulations

This chapter investigates the transport of conservative solutes in shallow water environment. The random walk model is applied to solve the depth-integrated advection-diffusion equation. Firstly, this model is verified by solving an instantaneous release problem in uniform flows. Analytical solutions are used as a reference. Extensive parametric studies have been carried out to investigate the sensitivity of the predictions to the computational parameters. Then, the random walk model is used to solve a solute oscillation problem along a hypothetical tidal estuary. The results of a TVD-MacCormack model are used as a reference. Finally, this chapter describes the applications of the random walk scheme to simulate the wind-driven chaotic mixing in a shallow circle lake. The results are compared with previous research from a qualitative point of view.

Chapter 6

6.1 Advection and diffusion transport in uniform flows

The instantaneous release problem in uniform flows is tested firstly using the random walk model. When the uniform flow only follows the x direction (v = 0, D_{xy} = 0, D_{xx} = D_s, D_{yy} = D_t), the analytical solution of this ideal test case can be expressed as:

$$S(x,y,t) = \frac{M}{4\pi t\sqrt{D_s D_t}} e^{-\frac{(x-x_0-ut)^2}{4D_s t} - \frac{(y-y_0)^2}{4D_t t}} \quad [6.1]$$

In this section, the total amount of solute material M = 233.06 kg is released suddenly at the initial location (x_0, y_0). As shown in Figure 6.1, the water depth is set to be H = 1 m, and the *Chézy* coefficient is 40 $m^{1/2}/s$ for the whole test area. The streamwise dispersion and transverse dispersion are typical values of ε_s = 13.0 and ε_t = 1.2 respectively for open channel flows (Falconer 1991). Two flow conditions are considered in this section. The first one is a uniform flow with u = 1 m/s along the x direction (θ = 0). The solute material is initially located at (x_0, y_0) = (0, 400 m). The second one is a uniform flow aligned diagonal direction (θ = 45°). The velocity is set to be u = v = $1/\sqrt{2}$ m/s. For computations in both scenarios, the particle numbers P is 2.33×10^6 and the time step is 1 s.

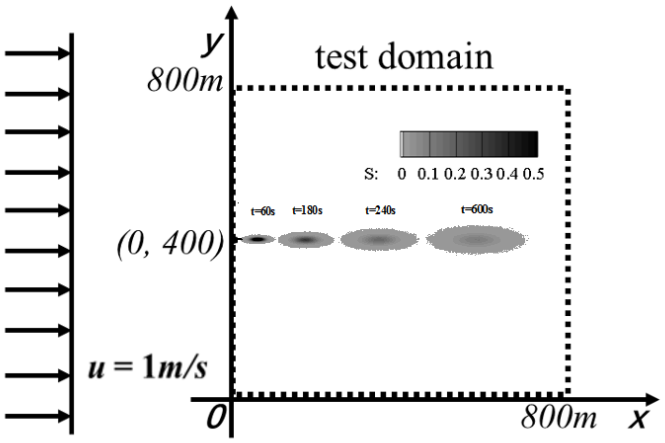

(a) x direction flow

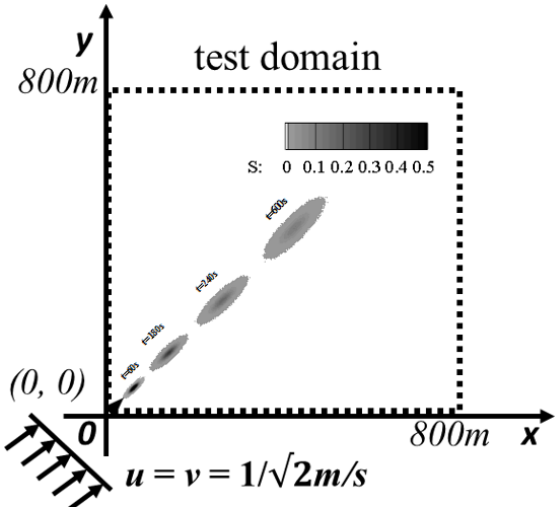

(b) diagonal direction flow

Figure 6.1 Instantaneous release problem in a uniform flow. (a) x direction flow; (b) diagonal direction flow

The development of concentration contours for flows in the x direction and diagonal direction are presented in Figures 6.1 (a) and (b) respectively. It is notable that the major axis of the elliptical patches is along their flow directions. The cloud of the solute experienced rapid elongation on its path.

The reason is that streamwise dispersion is ten times larger than the transverse dispersion. The results for the same test case obtained by the grid-based method, TVD-MacCormack, can be found in Liang et al. (2010).

6.1.1 Influence of time steps

The advantage of the random walk model includes high accuracy and small numerical diffusion. However, the expense that comes with this Lagrangian approach is its high computational cost. As seen in the scheme description, the amount of the computation depends on two factors: the size of the computational time steps the model applied, and the number of particles to present the pollutant cloud. Therefore, the choices of these two factors are crucial to the efficiency of the random walk model. The following part of this section is to discuss the influence of the two parameters on the random walk model when applied to the instantaneous release problem in uniform flows.

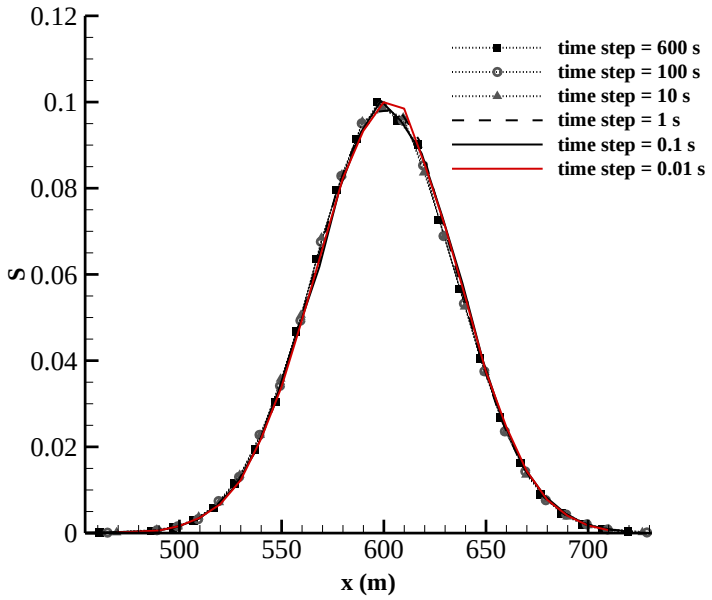

Figure 6.2 Concentration distributions at 600 s with changes in time steps (x direction flow)

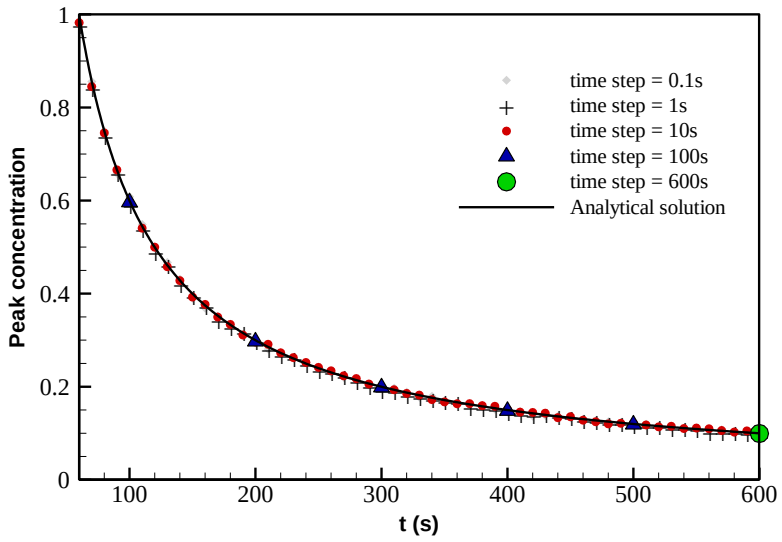

Figure 6.3 Development of peak concentrations with changes in time steps (x direction flow)

A great deal of research on time steps has been taken under the Euler scheme. The size of Δt is restricted by the CFL condition. Usually, the smaller the time step is, the more accurate and stable the simulation will be. However, it tells a different story for the random walk model. Figure 6.2 presents the longitudinal concentration profile at 600 s after the solute release. Regardless of the time step of 600 s or 0.01 s, the same concentration profile is predicted by the model. Variations of the peak concentration are not affected by the size of time steps as well, as seen in Figure 6.3.

This independent property of time steps can be derived through the iteration process. After n times iterations, the position of the particles at t time is expressed as:

$$x_1(t) = x_0 + \bar{U}n\Delta t + \sqrt{2D_s\Delta t} \cdot \sum_{i=1}^{n} r_i \quad [6.2]$$

$$y_1(t) = y_0 + \bar{V}n\Delta t + \sqrt{2D_t\Delta t} \cdot \sum_{j=1}^{n} r_j \quad [6.3]$$

If the time step changes to be $m\Delta t$, n/m times iterations are needed for the new time step. Then, the new position of the particles at t time is expressed as:

$$x_2(t) = x_0 + \bar{U}n\Delta t + \sqrt{2D_s\Delta t} \cdot \sqrt{m} \sum_{i=1}^{n/m} r_i \quad [6.4]$$

$$y_2(t) = y_0 + \bar{V}n\Delta t + \sqrt{2D_t\Delta t} \cdot \sqrt{m} \sum_{j=1}^{n/m} r_j \quad [6.5]$$

In the present model, the random numbers r_i follow a normal distribution with a mean of zero and a standard deviation of unity, as shown in Equation [6.6]. According to properties of a normal distribution (Bryc, Wlodzimierz 1995), $\sum_{i=1}^{n} r_i$ and $\sqrt{m} \sum_{j=1}^{n/m} r_j$ have the same expectation and deviation.

$$r_i \sim N(e, \sigma^2) \text{ , where } e = 0, \sigma^2 = 1 \quad [6.6]$$

$$\sum_{i=1}^{n} r_i \sim N(n\mu, n\sigma^2) \quad [6.7]$$

$$\sqrt{m} \cdot \sum_{j=1}^{\frac{n}{m}} r_j \sim N\left(\sqrt{m}\frac{n}{m}\mu, \frac{n}{m}\left(\sqrt{m}\sigma\right)^2\right) \quad [6.8]$$

Therefore, the results will all obey the distribution of $N(0, n)$ no matter what size of the time step is used. It can be concluded that the change of time steps does not affect the accuracy of the present model for the uniform flow with constant water depth.

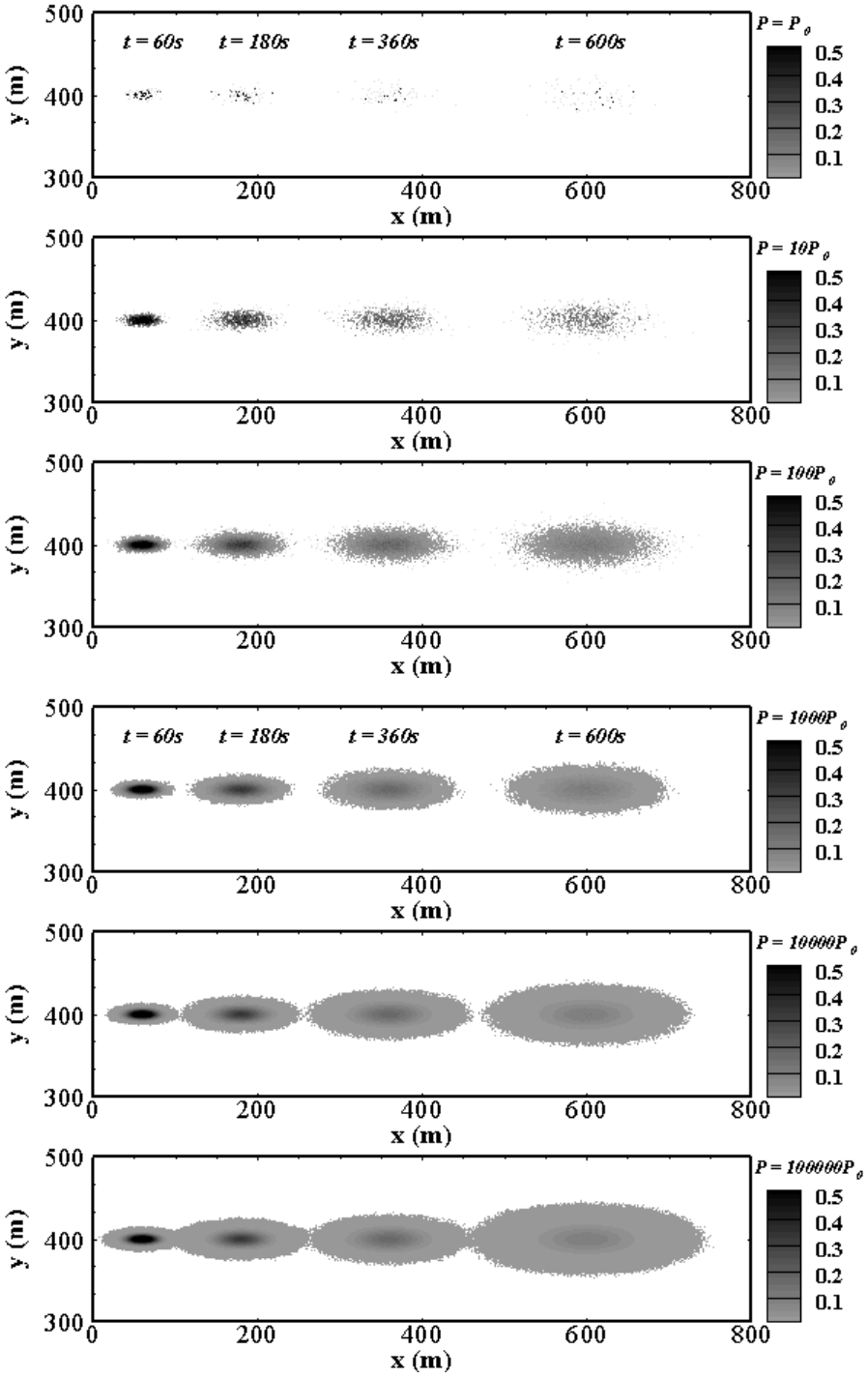

Figure 6.4 Evolution of the solute cloud in x direction uniform flows ($P_0 = 233$)

6.1.2 Influence of particle numbers

Figure 6.4 shows a qualitative illustration of the solute transport process predicted by the random walk model using different configurations of particle numbers. In general, the contour turns out to be more notable with the particle number increases. Larger particle numbers significantly improve the visual effect of the elliptical cloud for solute distribution. To get a quantitative analysis, the predicted results are compared with analytical solutions. Figure 6.5 shows variations of peak concentration with different particle numbers used in the simulation. The size of sampling bins is set to be a circle with a radius of one meter. It is notable that small particle numbers tend to produce numerical oscillations. On the contrary, by setting a more substantial number of particles in the model, the prediction approaches closer to the analytical solution. For example, when 2.33×10^7 particles simulated in the model, the peak concentration is identical with the analytical solution.

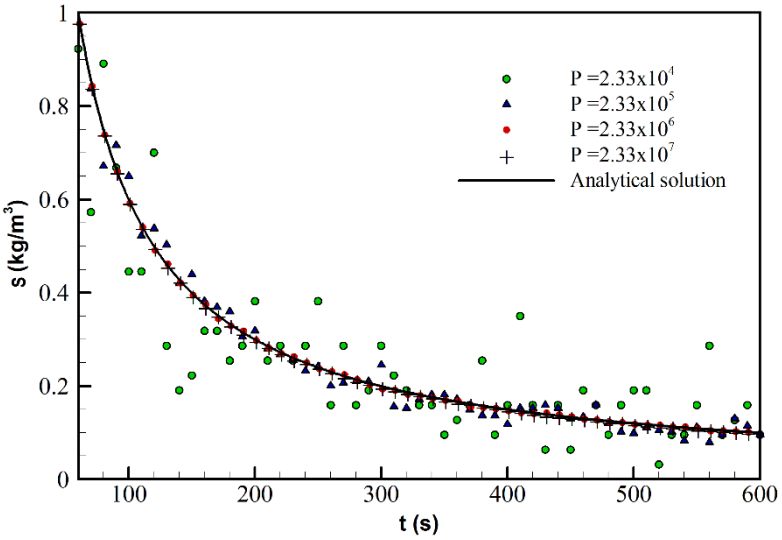

Figure 6.5 Variation of peak concentration for x direction flows

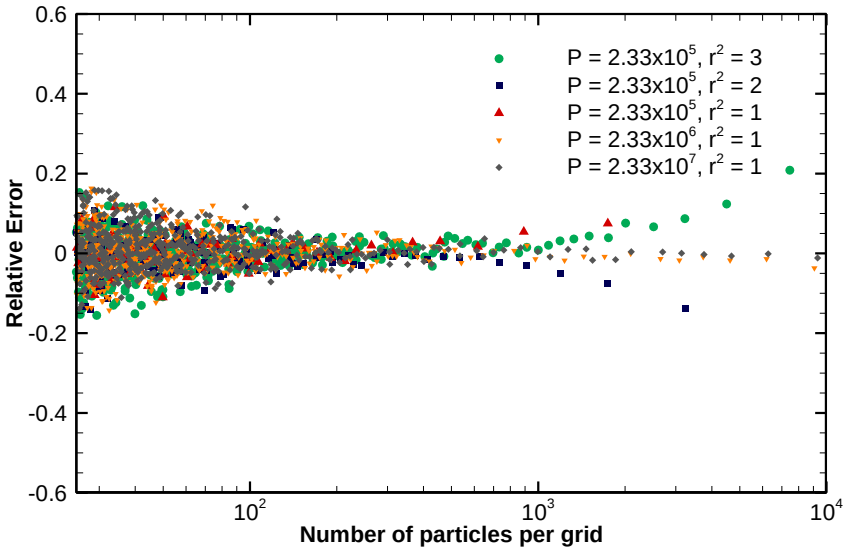

(a)

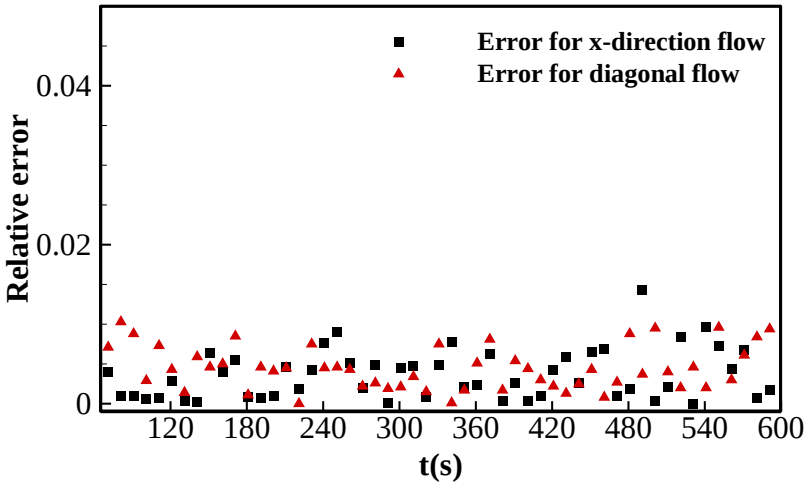

(b)

Figure 6.6 Relative errors of peak concentration (a) with the changes in particle numbers in each sampling bins; (b) with changes in time

The relative errors with different particle numbers different of bin sizes are compared in Figure 6.6 (a). The relative error is defined by dividing the difference between the predicted and the analytical peak concentration by the

analytical results. In the legend, r represents the radius of the bin. It is clear that with the growth of particle number put into the simulation, the error decreases significantly. The error for small particle numbers jumps beyond 18%, which is unacceptable in a strict simulation. When the number of particles in each sampling bins approaches 200 to 300, the relative error is reduced to less than 5%. This means that the particle should be guaranteed to be higher than hundreds per bin to show a reasonable result for the solute concentration. Also, it is worth to note that the error for both x direction and diagonal flows is always consistent with each other, as shown in Figure 6.6 (b). This means the model is not affected by the concentration gradient.

6.2 Solute oscillation along a 1-D tidal estuary

This section considers solute material which is being transported forward and backward in a hypothetical tidal estuary. As shown in Figure 6.7, the boundary condition for the left end is regarded as a sinusoidal tide, while the right side of this estuary is considered as a vertical wall. The total length of the estuary is 13,800 m, and the bed elevation changes from -5 m at the end of the seaward to 0 m at the right end. In this case, the tidal flow has an average water level of 0 m and amplitude of 2 m, rising from the average water level at the beginning of the simulation. Before the pollutant transport simulation, the predictions of the flow field were obtained by using TVD-MacCormack scheme to solve the SWEs. The discretized velocity field is then reconstructed into a continuous form using linear interpolation. The initial depth-averaged concentration s is set to be 100 kg/m^3 at the cell located at x = 10 km, while the concentration of the remaining fields is set to be zero.

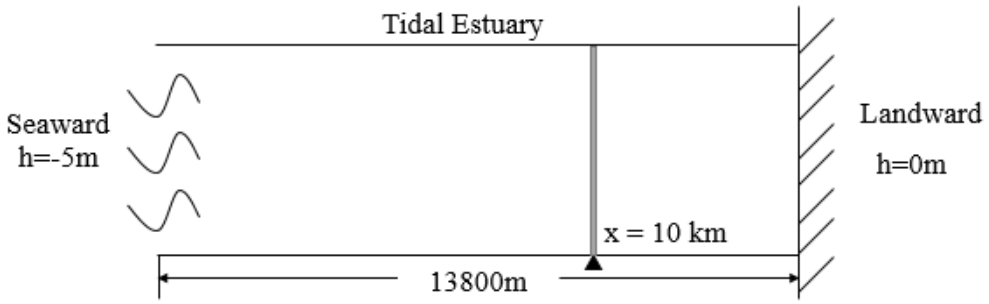

Figure 6.7 1-D hypothetical tidal estuary

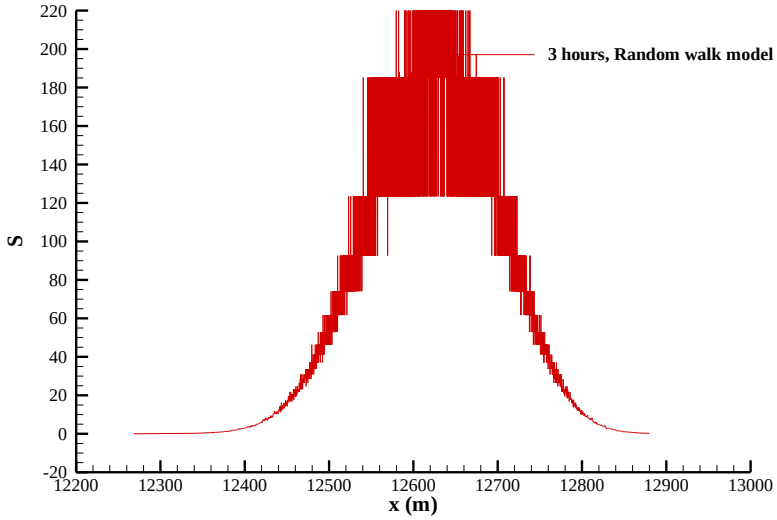

(a) Δb = 0.01 m

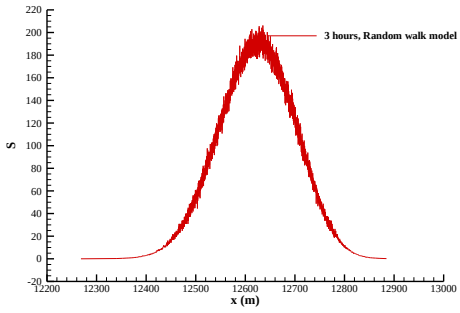

(b) Δb = 0.1 m

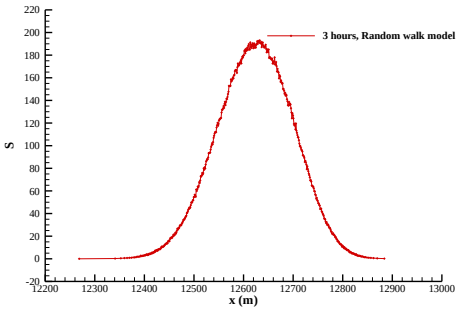

(c) Δb = 1 m

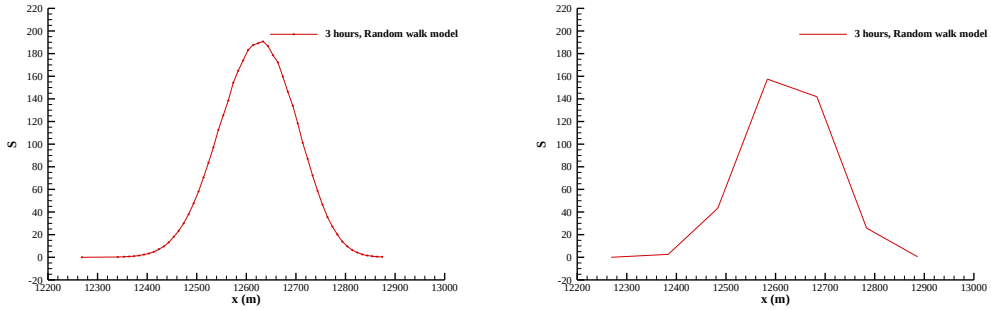

(d) Δb = 10 m (e) Δb = 100 m

Figure 6.8 Distribution of the concentration along the hypothetical estuary at 3 hours with changes in sampling size Δb. (a) Δb = 0.01 m; (b) Δb = 0.1 m; (c) Δb = 1 m; (d) Δb = 10 m; (e) Δb = 100 m

The sampling processes is required to convert the scatter of particles to the concentration profile. This sampling algorithm is crucial in the interpretation of the results of the random walk method and in the evaluation of the concentrations, which introduces some artificial diffusion. Traditionally, this concentration profile, i.e. histogram, uses a fixed length to separate different bins. However, this fixed setting may lose the accuracy at some local parts. Figure 6.8 compares concentration profiles along the estuary at 3 hours with different sizes of Δb. The Δb represents the minimum size of the sampling bins used in the random walk model. As illustrated in the Figure 6.8 (a), when the scale of sampling bins is below 1 m, obvious non-physical oscillations will be generated in concentration profiles. This is due to the limited numerical precision of computers. It is also deficient if the bin sizes are too large. As shown in Figure 6.8 (e), the accuracy of concentration is compromised when the sampling bins are more than ten percent of the occupied range. In this work, the length of the bin is chosen automatically by including 200 particles within

each bin along the hypothetical estuary. This dynamic determination of the bin size is found to avoid spurious fluctuations and achieve good comparisons with analytical and previous results. A series of smooth concentration profiles along the estuary at both high and low water levels is shown in Figure 6.9 to 6.13. When the solute cloud moves nearly to the landward position, the tidal flow generally decelerates because of the wall boundary.

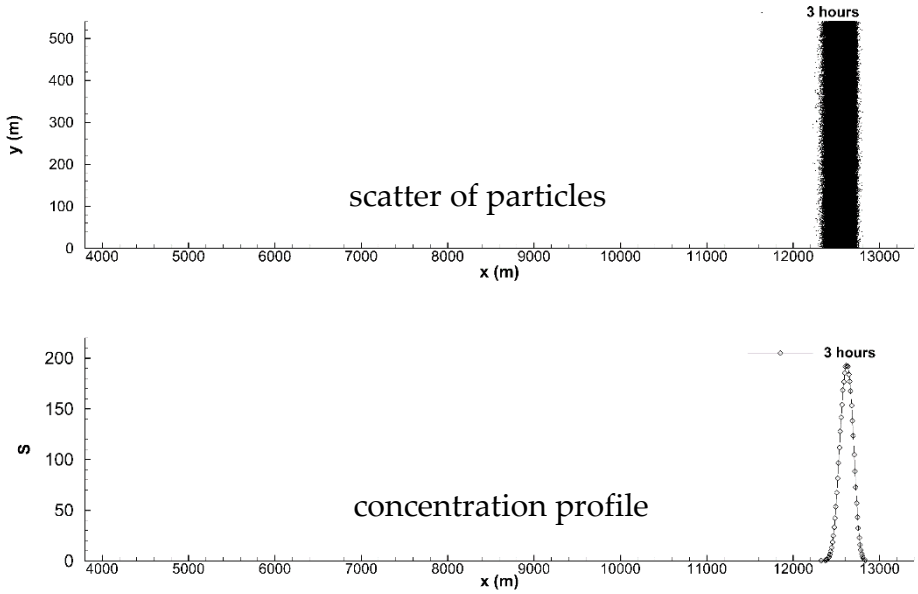

Figure 6.9 Distribution of solute particles and concentration along the 1-D hypothetical estuary at 3 hours

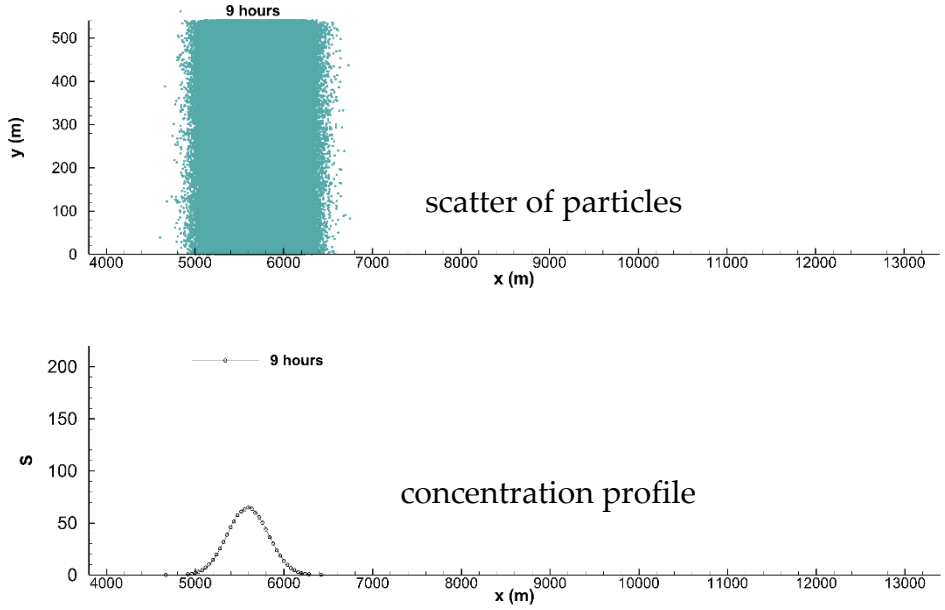

Figure 6.10 Distribution of solute particles and concentration along the 1-D hypothetical estuary at 9 hours

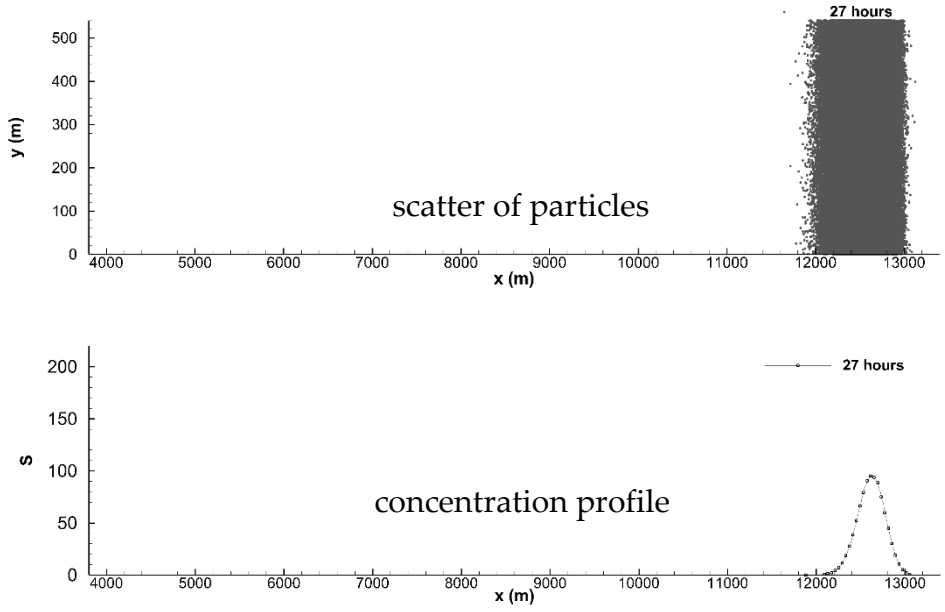

Figure 6.11 Distribution of solute particles and concentration along the 1-D hypothetical estuary at 27 hours

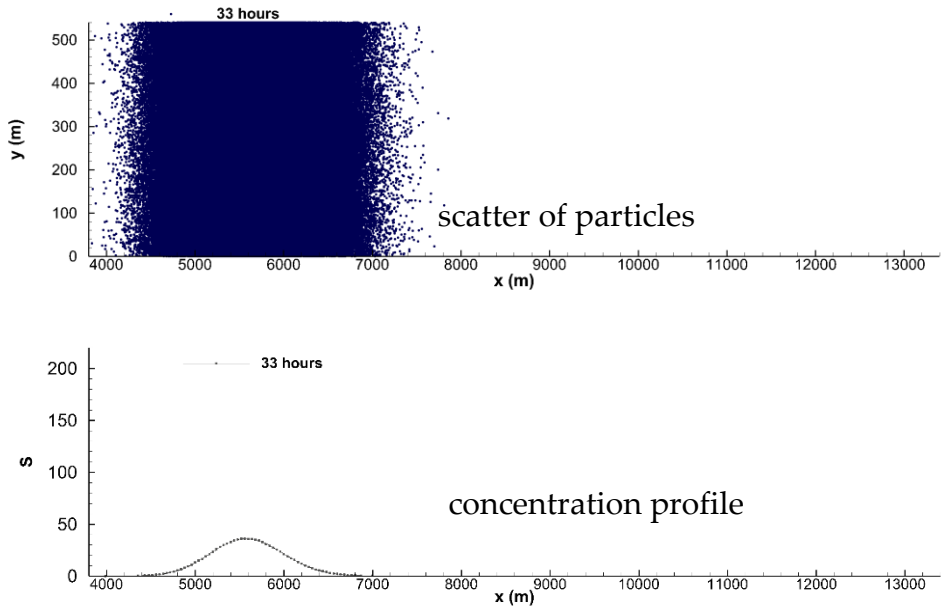

Figure 6.12 Distribution of solute particles and concentration along the 1-D hypothetical estuary at 33 hours

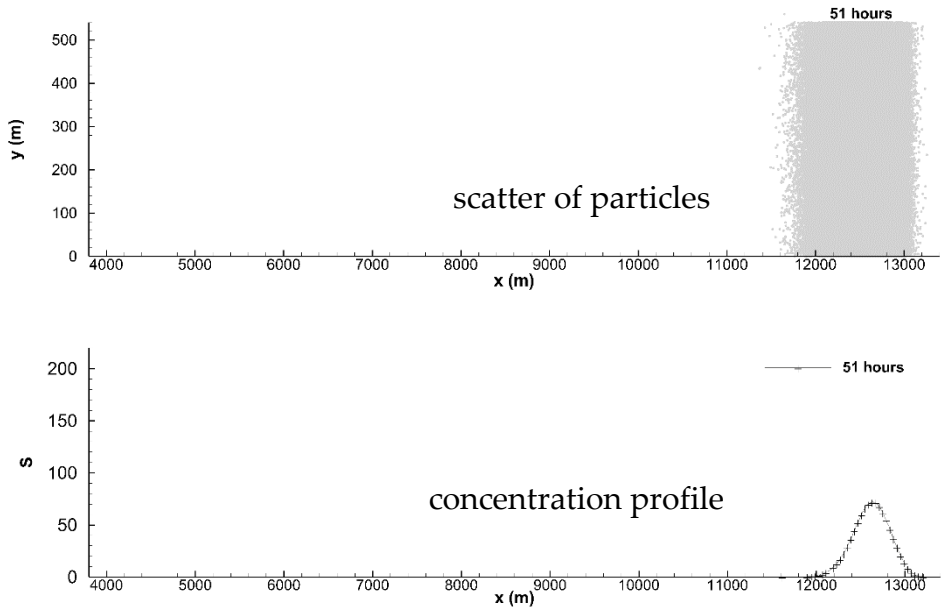

Figure 6.13 Distribution of solute particles and concentration along the 1-D hypothetical estuary at 51 hours

An illustration for the particles position and their distribution along time is given by Figure 6.9 to 6.13. A series of concentration distributions and the scatter of particles at high and low water are plotted with time. It is well presented that particles travel with wave flows and disperse in the longitudinal direction. The instantaneously released solute flows with the rising water to the closed wall under the influence of tidal currents, while the receding water is flowing to the open boundary. At the same time, the region of the solute is enlarging because of the effect of dispersion. For example, at the 3 hours, as shown in Figure 6.9, the solute reaches the landward side of the computational domain. Then these solute turns back towards the seaward side with the tidal currents. The range occupied by solutes expands from about 400 m at 3 hours to about 1200 m at 9 hours. It is notable that the horizontal range occupied by solutes at 27 hours is smaller than that at 9 hours and the peak concentration is even higher at 27 hours than at 9 hours. This is because that the water level is higher near the right-side wall and the tidal current generally decelerated when approaching the closed boundary. Note that S-axis is defined as sH (as seen in Chapter 5, Equation5.7), therefore does not represent the physical solute concentration. The apparent increase of S with time is due to the increase of H, rather than the increase of solute concentration, and it therefore does not violate the second law of thermodynamics.

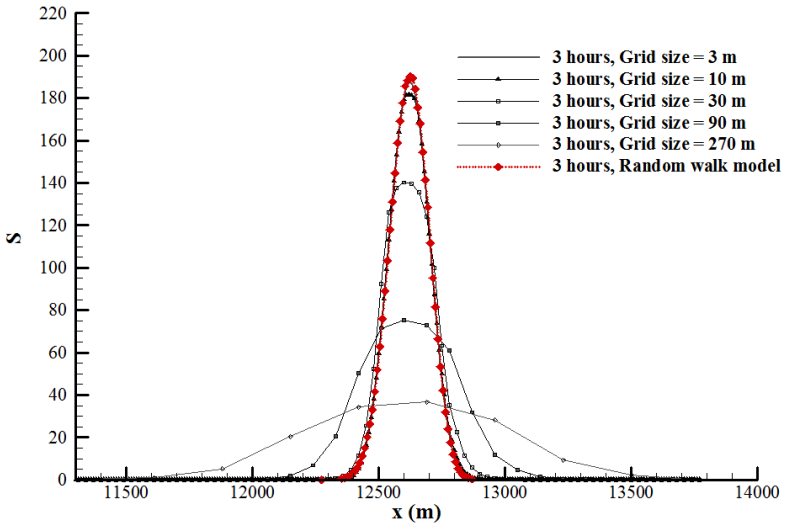

(a) 3 hours

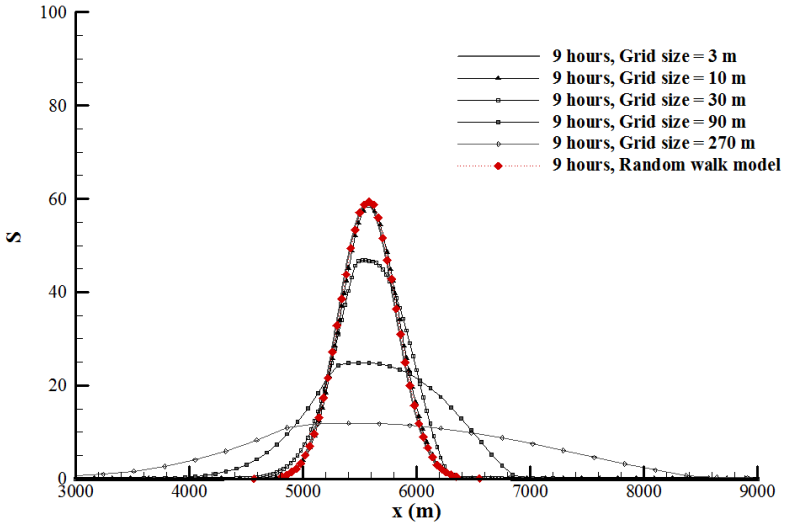

(b) 9 hours

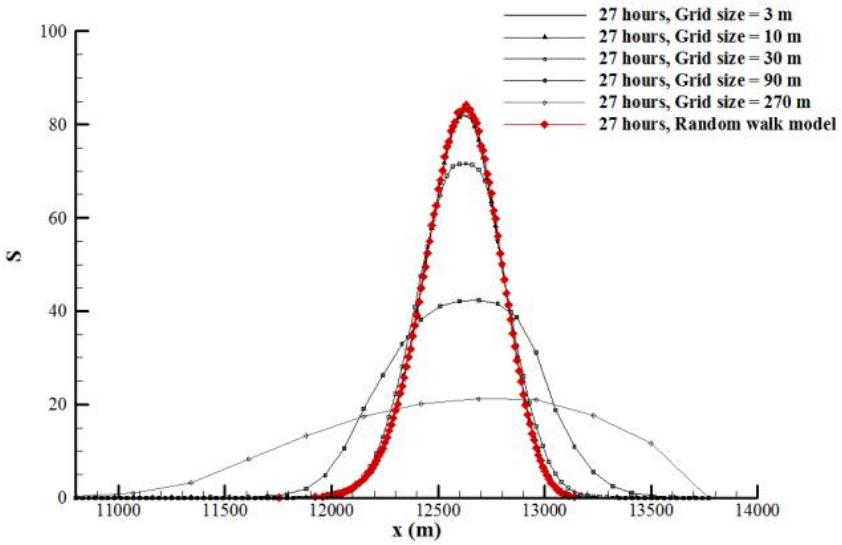

(c) 27 hours

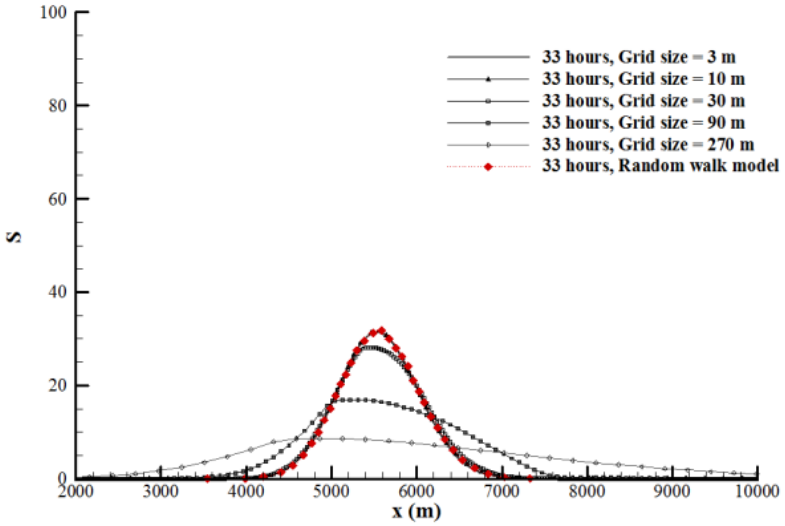

(d) 33 hours

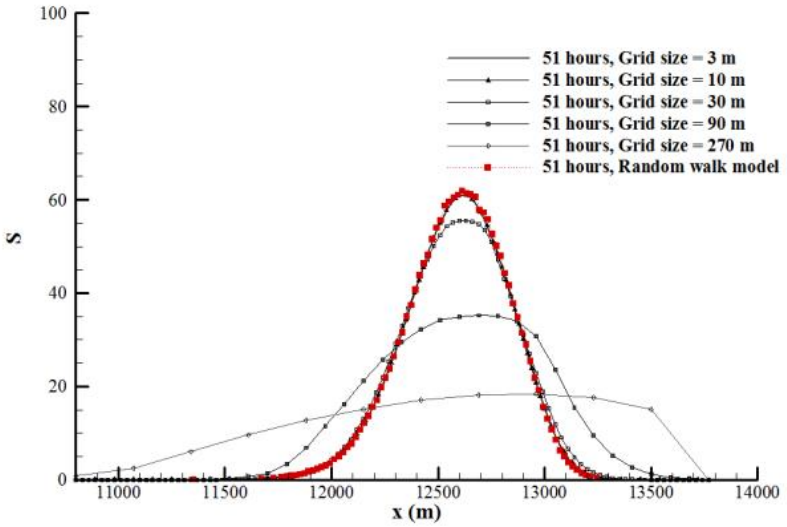

(e) 51 hours

Figure 6.14 Distribution of the concentration along the estuary with the changes in grid size. (a) 3 hours; (b) 9 hours; (c) 27 hours; (d) 33 hours; (e) 51 hours

The numerical solution of TVD-MacCormack model is used as a reference for this case. For such grid-based methods, solutions are usually sensitive to its grid size. The finer the grid is, the more accurate the simulation will be, although the more computationally expensive it might be. The numerical diffusion for the Eulerian model is more obvious at the beginning because of the sharp concentration gradient. Taking Figure 6.14 (a) as an example, it presents the concentration profile at 3 hours since the beginning. Several different cell sizes, from 3 m to 270 m, are used in the mesh method simulation. When the mesh size is increased to 270 m, the concentration distribution is too flat to demonstrate a proper concentration distribution. The results for the grid size of 3 m are nearly three times that of 90 m. On the

contrary, the random walk model is less diffusive. A narrower distribution and a higher peak concentration are predicted by the present model, and it is identical to the extreme of the concentration trend.

Influence of time steps for unsteady flow

The expense that comes with the random walk model is its high computational cost. The choice of time steps is crucial to the efficiency of numerical models. A great deal of research on time steps has been taken under the steady flow conditions. It was concluded that the change of time steps does not affect the accuracy of the present model for the uniform flow with constant water depth. However, it tells a different story for the unsteady flows. The following part of this section is to discuss the influence of this parameter on the random walk model when applied to the instantaneous release problem in unsteady flows.

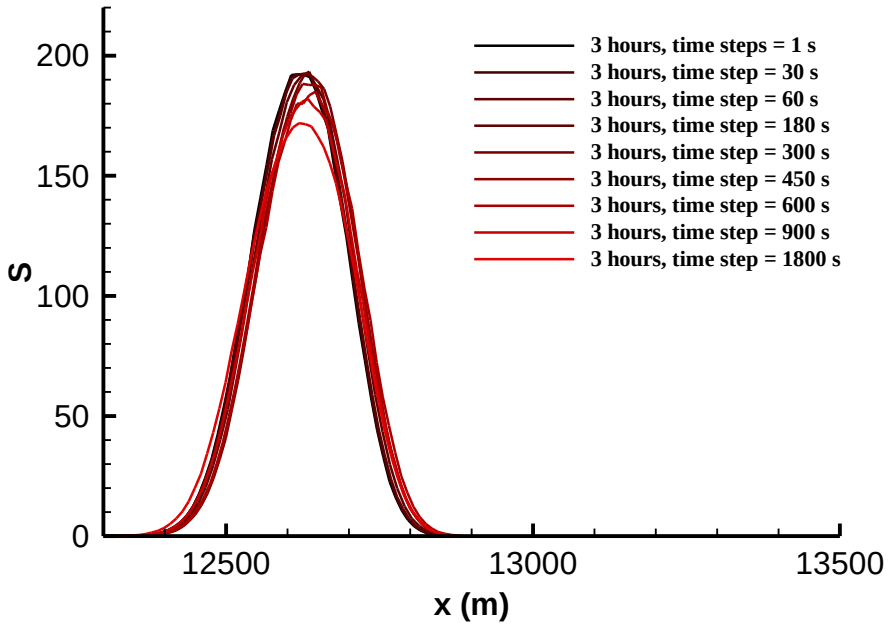

(a) 3 hours

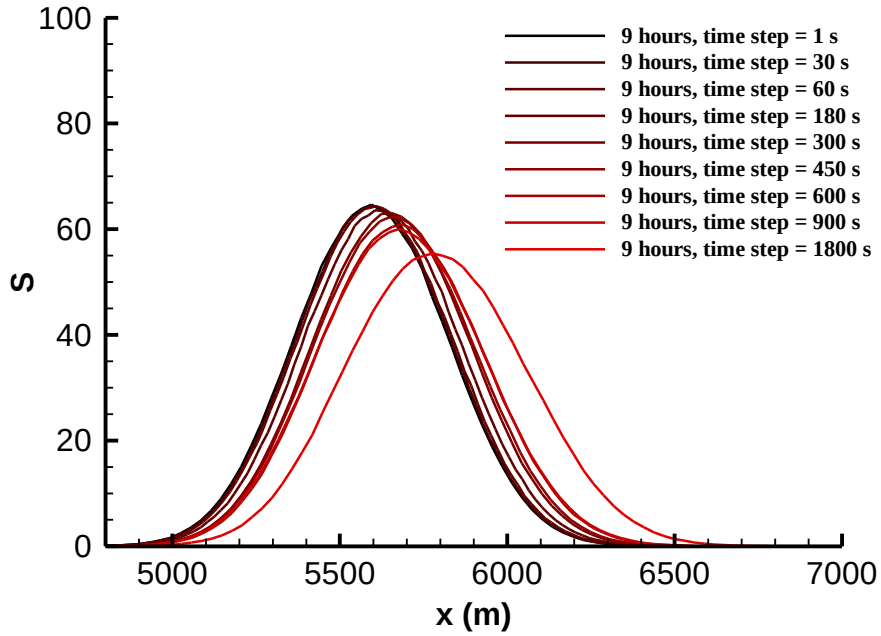

(b) 9 hours

Figure 6.15 Distribution of the concentration along the tidal estuary with changes in time steps

The Figure 6.15 presents the longitudinal concentration profile at 3 hours and 9 hours after the solute release in the tidal estuary. Several different time steps, from 1 s to 30 min, are used in the random walk simulation. When the time step is smaller than 30 s, the predicted concentrations are not affected by the choice of the time step. When the time step is increased to 30 min, the peak concentrations are under-predicted by the random walk model. This is more obvious in the 9 hours simulation. Therefore, in the current random walk model the time step should be less than 30 s to guarantee an accurate prediction.

6.3 Wind-driven chaotic mixing in a shallow circle lake

In this section, the random walk model is applied to simulate the particle motion due to wind-driven mixing in a shallow lake. The action of wind on the

bodies of water creates shear stress on the free surface, which drives the water flow in the water underneath. The wind shear stress is imposed on free surface. When integrated over the water depth, it appears as the last term in the Equations [3.2] and [3.3]. In this section, wind shear of constant magnitude is assumed to be uniformly distributed throughout the domain.

6.3.1 Kranenburg's model lake

As shown in Figure 6.16, the property of the circular lake is suggested by Kranenburg (1992). The velocity field is described by a stream function in the polar coordinate system:

$$\psi = Br(1 - \frac{r}{R})\, sin(\varphi - \theta) \quad [6.9]$$

$$B = \frac{ln\, Z}{4\kappa} u_* H_{mean} \quad [6.10]$$

$$Z = \frac{H_{mean}}{z_0} \quad [6.11]$$

The von Kármán constant κ is set to be 0.4; the mean water depth H_{mean} is 0.5 m and the radius of the lake R_0 is 120 m; z_0 is a roughness height of the bed, set to be 2.8 mm. The constant τ_w is 0.002 N/m^2. $u_* = \sqrt{\tau_w/\rho}$ is the friction velocity at the surface. The water depth H is described by a function of radial distance r from the basin centre as follows:

$$H = H_{mean}(\frac{1}{2} + \sqrt{\frac{1}{2} - \frac{1}{2}\frac{r}{R_0}}) \quad [6.12]$$

These physical parameters are set to be the same as those in Kranenburg (1992) for the comparison purpose.

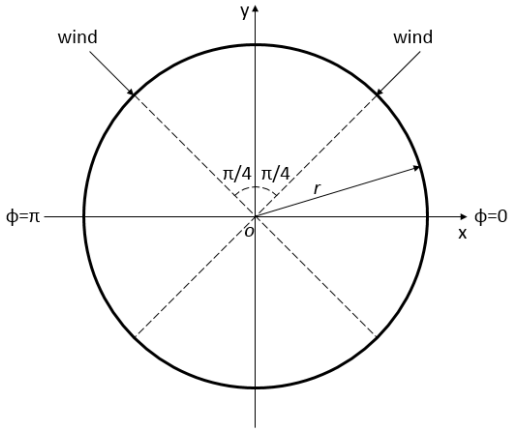

Figure 6.16 Aerial view of the model lake with a periodic sequence of storm events

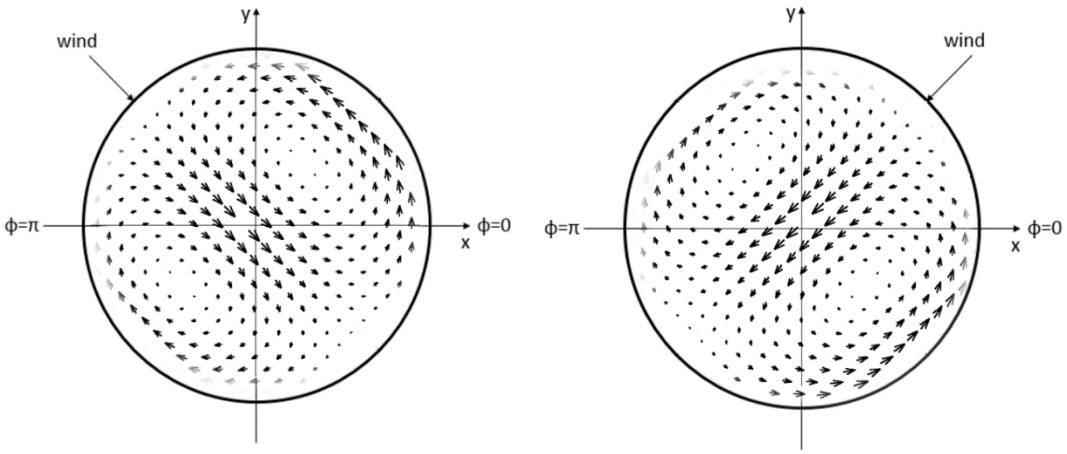

Figure 6.17 Velocity fields in the Kranenburg's model lake with single direction of the wind

Kranenburg (1992) found that the particle motion becomes chaotic when surface wind stress periodically changes its direction. Therefore, a sequence of periodic storm events is designed for this case. During the first and second halves of a period, the direction of the storm wind jumps back and forth between the northeast and northwest directions, respectively. It is assumed that the wind stress suddenly changes its direction in between the half intervals,

while its intensity is constant. At the same time, the Euler velocity field instantaneously adapts to wind conditions. The resulting flow field is governed by a dimensionless storm duration parameter μ as following:

$$\mu = \frac{ln\, Z}{8\kappa R_0} u_* t_s \qquad [6.13]$$

where t_s is the storm duration, i.e. half of the period T.

6.3.2 Influence of diffusion coefficient

For all the cases considered, Poincaré sections are used to illustrate the mixing properties. Poincaré sections represent a lower dimensional subspace within the state space of a dynamical system. They preserve many characteristics of periodic or quasiperiodic orbits of the original dynamical system and are therefore often used for studying the original system in a simpler way. Initially, independent particles along the x-axis were released at the $\phi = 0$ and $\phi = \pi$, as seen in Figure 6.16. The positions of these particles were traced and plotted on one diagram after each cycle (the end of each second storm). These particles are tracked for 500 periods in this case. The points on the Poincaré section represent the superposition of particle positions at the end of each cycle. For comparison purposes, the diffusive process is ignored to test the behaviour of the advection part in the random walk model. For small μ, as shown in Figure 6.18 (a), the elliptic periodic points are surrounded by two large islands of regular motion. The area of the chaotic region increases with the increase of μ, while the sizes of the period-one islands decrease. When μ is beyond 0.70, the elliptic points are no longer obvious, and only chaotic motion remains (for μ = 0.84). These findings are qualitatively similar to previous results of Kranenburg (1992), as shown in Figure 6.19.

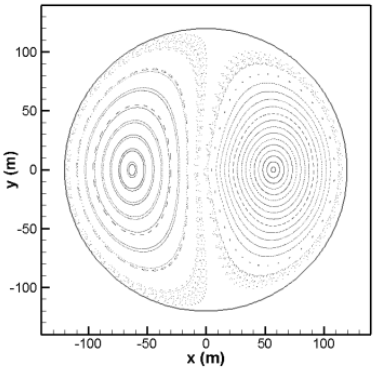

(a) μ = 0.14

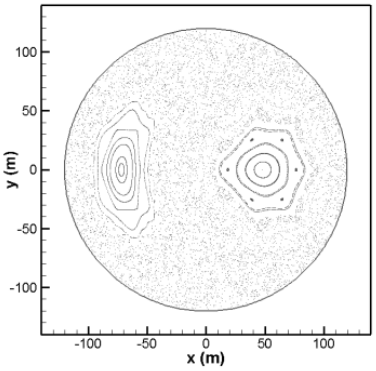

(b) μ = 0.28

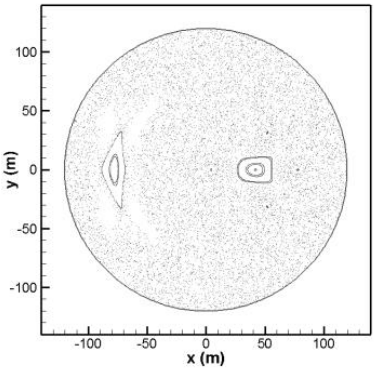

(c) μ = 0.42

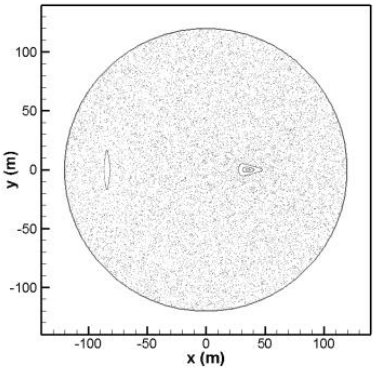

(d) μ = 0.56

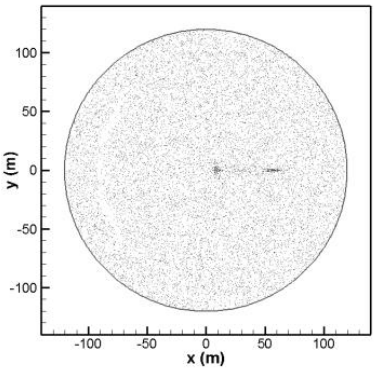

(e) μ = 0.70

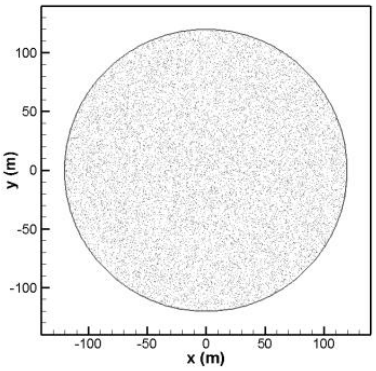

(f) μ = 0.84

Figure 6.18 Poincaré sections for wind periodically blowing from north-east and north-west with different μ (without diffusive process) (a) μ = 0.14; (b) μ = 0.28; (c) μ = 0.42; (d) μ = 0.56; (e) μ = 0.70; (f) μ = 0.84

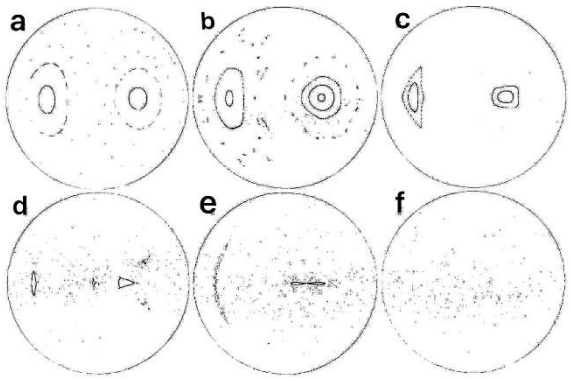

Figure 6.19 Kranenburg's Poincaré sections showing particle positions after each second storm with different μ (a) μ = 0.14; (b) μ = 0.28; (c) μ = 0.42; (d) μ = 0.56; (e) μ = 0.70; (f) μ = 0.84 (Kranenburg, 1992)

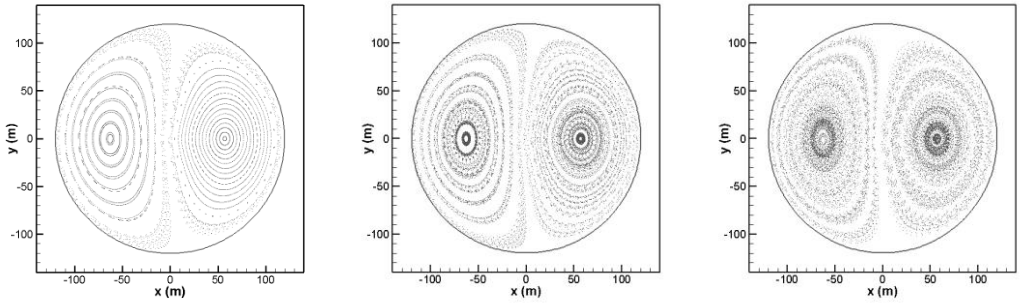

(a) ε_s = 0.0 (b) ε_s = 0.001 (c) ε_s = 0.01

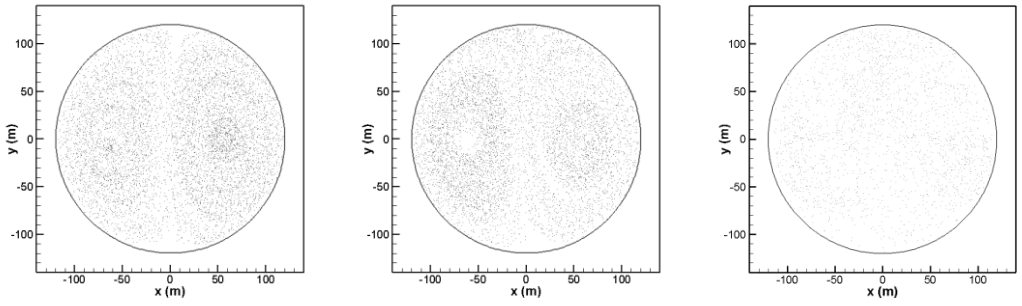

(d) ε_s = 0.1 (e) ε_s = 1 (f) ε_s = 10

Figure 6.20 Poincaré sections for both advection and diffusion processes for μ = 0.14 and with different ε_s: (a) ε_s = 0.0; (b) ε_s = 0.001; (c) ε_s = 0.01; (d) ε_s = 0.1; (e) ε_s = 1.0; (f) ε_s = 10

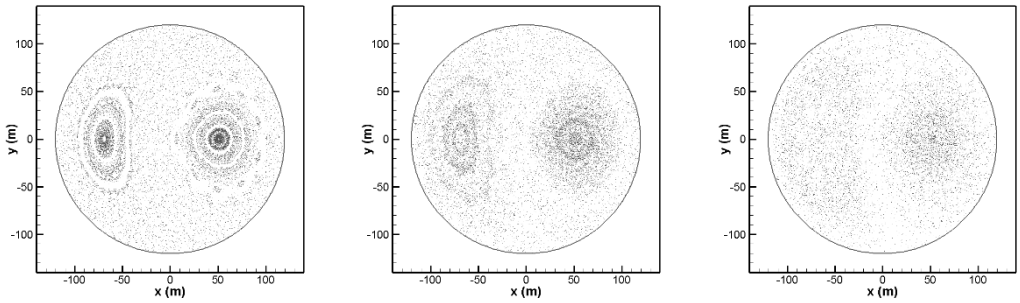

(a) ε_s = 0.001 (b) ε_s = 0.01 (c) ε_s = 0.1

Figure 6.21 Poincaré sections for both advection and diffusion processes for μ = 0.28 and with different ε_s: (a) ε_s = 0.001; (b) ε_s = 0.01; (c) ε_s = 0.1

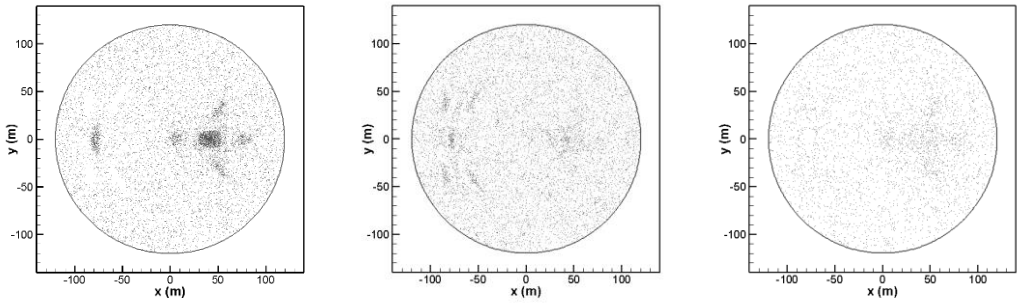

(a) ε_s = 0.001 (b) ε_s = 0.01 (c) ε_s = 0.1

Figure 6.22 Poincaré sections for both advection and diffusion processes for μ = 0.42 and with different ε_s: (a) ε_s = 0.001; (b) ε_s = 0.01; (c) ε_s = 0.1

Then, both advection and diffusion processes are considered as tracer particles and are also spread by turbulence and shear dispersion during each storm. Figure 6.20 depicts the impact of streamwise dispersion ε_s (the transverse dispersion ε_t is constant at 0 in this section.) on this chaotic mixing phenomenon. For ε_s equal to 0.001, it is still clear that the circular lake is divided into two large islands and positions of the elliptic periodic points are still obvious. With the increase of the streamwise dispersion, this pattern

becomes more and more blurred. It is worth to mention that, the growth of the streamwise dispersion will not change the position of elliptic periodic points, but it will amplify the erratic motion considerably.

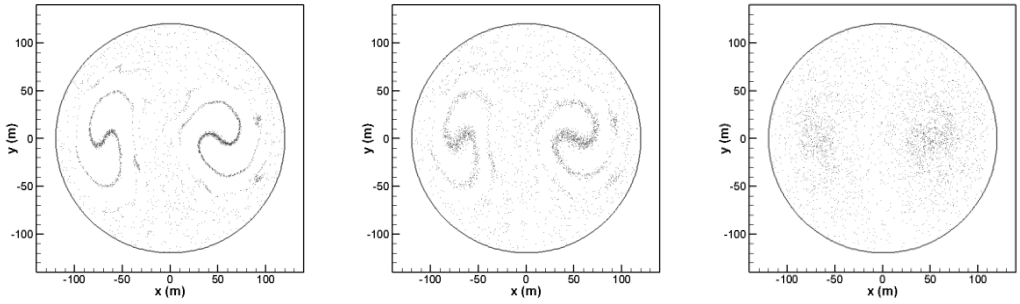

(a) $\varepsilon_s = 0.001$ (b) $\varepsilon_s = 0.01$ (c) $\varepsilon_s = 0.1$

Figure 6.23 Snapshots of the particle distribution in Kranenburg's model lake ($t = 32T$; $\mu = 0.28$)

For $\mu = 0.28$ and 0.42, the entire calculation domain is chaotic when the dispersion ε_s is only 0.1, as shown in Figures 6.21 and 6.22. This means that the increase in the duration of the periodic storm will exacerbate the impact of the diffusion coefficient, making it easier to achieve a chaotic state. Figure 6.23 shows the advection and diffusion behaviour of a line of 10,000 particles after 32 periods of the storm event. The line is initially positioned along the x-axis. Both whorl-type and tendrils structures coexist when μ is 0.28. With the increase of the dispersion parameter, elliptic and hyperbolic points all disappear, and particle motions reach the global chaotic state.

6.4 Chapter summary

In this chapter, the random walk model is applied to solve the depth-integrated advection-diffusion equation. First, this model is verified by solving

a classic instantaneous release problem in a uniform flow. It has been found that simulations are independent of the size of the time step. The particle number significantly influences the performance of the random walk model. Too few particles degrade the visual inspection and quantitative examination of the solute distribution. In uniform-flow applications, a relatively large time step will reduce the computation expense without compromising accuracy. Then, investigations are carried out regarding the oscillation of a pollutant cloud in a tide estuary. The sampling method is optimised to convert the particle distributions into concentration profiles. The random walk simulations display high accuracy, which can only be achieved by the method-based simulations with extremely fine resolutions. The mesh-based methods are shown to be highly sensitive to the grid resolution. Finally, the model is used to simulate the chaotic mixing process. The results for pure advection process are consistent with the findings reported in previous research. Because of the presence of turbulent diffusion and bottom friction in any real lake, the advection process is always accompanied by the longitudinal dispersion process. This study shows that the streamwise dispersion plays an important role in the material mixing pattern.

Chapter 6

Chapter 7

Random walk simulation of non-conservative pollutant transport in shallow water flows

Research work in the last chapter demonstrates that the random walk model is highly stable and nearly free of artificial diffusion in solving the solute transport problems in aquatic environments. This chapter further develops the random walk model to simulate more complex hydro-environmental phenomena that involve the transport of non-conservative materials. First, it presents three ideal test cases to examine the capability of the random walk model for addressing the continuous release of non-conservative materials. Then, the model is applied to simulate the BOD-DO balance along a hypothetical river, with the analytical solutions as references. Finally, the developed scheme is used to predict the development of BOD and DO

concentrations in the Thames Estuary, so as to examine the model's capability of handling the complex geometry with large tidal oscillations.

7.1 Reactive process

Most of the materials transported by the flow are not inert in the fluid, such as nitrogen, phosphorus, bacteria and dissolved oxygen. In order to predict the spatial and temporal development of these non-conservative substances, the sources term q_s is introduced in Equation [5.7]. It represents the increase ($q_s > 0$) or decrease ($q_s < 0$) of the total amount of the solute because of chemical or biochemical reactions, and it can also represent a tracer injection or abstraction. For a substance subject to chemical or biological transformation, its decay or growth usually follows the principle of the first-order reaction:

$$q_s = -KS \qquad [7.1]$$

where K is the first-order decay rate or reaction constant. In the random walk model, an initial value of the mass $m_p^0 = \frac{M_0}{N}$ is assigned to every particle, where M_0 is the the total amount of solute material at time zero and N is the total number of particles. For the first-order decay processes, the mass of each particle is simply reduced by a fixed proportion at each timestep. For example, the mass of particle P at time t is expressed as:

$$m_p^{t-\tau+\Delta t} = m_p^{t-\tau} + \Delta t(-K_r m_p^{t-\tau}) \qquad [7.2]$$

where τ in the superscript represents the time of the particle release so that the duration of this particle experiencing decay is $(t - \tau)$. For particles released at time zero, their value of τ is zero and they have experienced decay from time

zero to the considered instant t. If particles are not released into the domain at the same time, such as in the situation of a continuous source, different particles carry different masses, and the concentration can be calculated via the probability density function weighted by the particles' masses.

7.2 Model refinement and verification

7.2.1 Continuous source

The present 2-D random walk model was first applied to the continuous release problem. A continuous discharge is released from the location (x_0, y_0) = (0, 400 m). The flow is uniform with u_0 = 1 m/s along the x direction. The water depth is constant with H = 1 m and the Chézy coefficient is 40 $m^{1/2}/s$ over the whole test area. The constants for calculating the streamwise dispersion and transverse dispersion coefficients are set to be typical values of ε_s = 13.0 and ε_t = 1.2, respectively, for straight open channel flows. According to Equation [5.2] to [5.5], the mixing coefficients in this case are calculated to be $D_{xy} = D_{yx} = 0$, $D_{xx} = D_s = 1.020$ m^2/s, $D_{yy} = D_t = 0.094$ m^2/s.

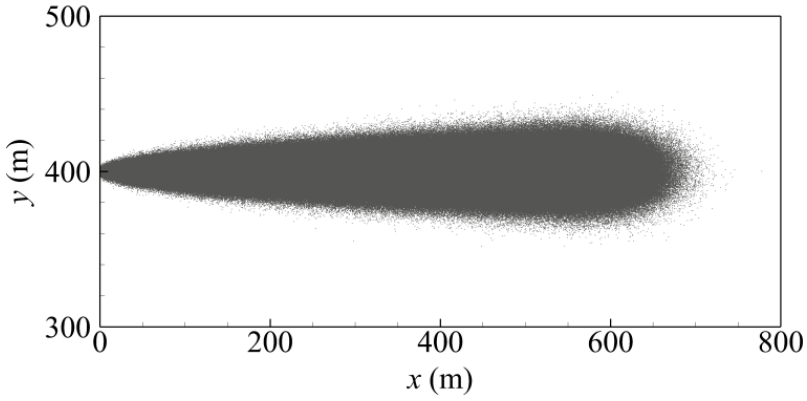

(a) Scatter of particles

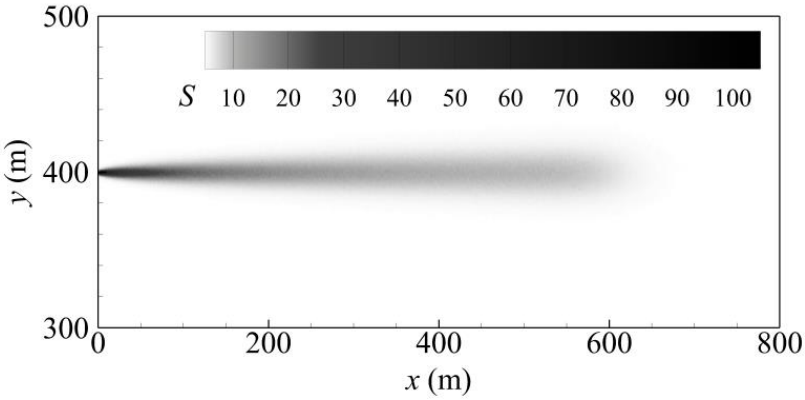

(b) Concentration distribution for the case of constant discharge rate

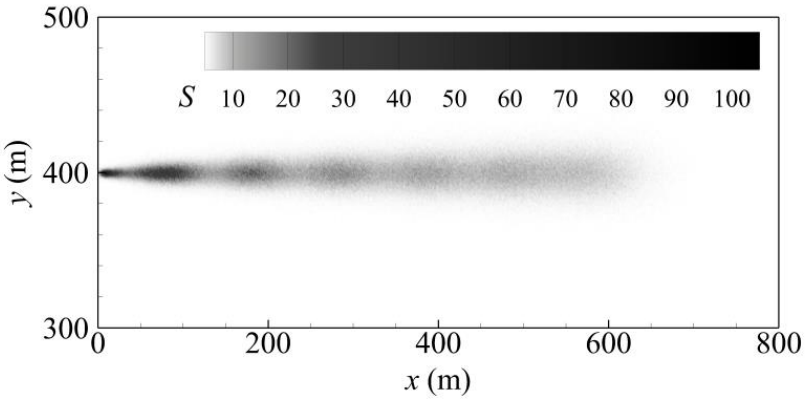

(c) Concentration distribution for the case of variable discharge rate

Figure 7.1 Continuous release problem in a uniform flow

Two pollutant discharge conditions are considered in this section. Firstly, the mass discharge rate $\dot{M}$ is constant at $\dot{M}_0 = 233.06\,\mathrm{kg/s}$. For this ideal case with uniform flow along the x direction and constant mass discharge rate $\dot{M}$, the analytical solution can be expressed as:

$$S(x,y) = \frac{\dot{M}_0}{\sqrt{4\pi D_{yy} x u_0}} e^{-\frac{u_0 y^2}{4 D_{yy} x}} \qquad [7.3]$$

Secondly, the time-varying mass discharge rate is applied to the model.

The mass discharge rate $\dot{M}$ is assumed to be a sinusoidal function of time, as seen in Equation [7.4].

$$\dot{M} = \dot{M}_0 \left(1 + \frac{1}{2}\sin\left(\frac{\pi t}{50}\right)\right) \qquad [7.4]$$

The time step is $\Delta t = 1\,\mathrm{s}$. The number of particles released to the computational domain is 10^3 per time step. Whether the mass discharge rate is constant or time-varying, the scatter of particles is the same, as illustrated in Figure 7.1 (a). The only difference is the mass associated to each particle. In the case of constant discharge rate, all the particles have the same mass. In the case of time-varying discharge rate, particles may carry different masses. The concentration contour 600 s after the start of the simulation is presented in Figures 7.1 (b,c). It is notable that the concentration generally decreases away from the source and the centreline of the pollutant cloud is in the flow direction. The contour of the concentration for the time-varying mass discharge rate depicts a certain degree of periodic oscillation along the flow.

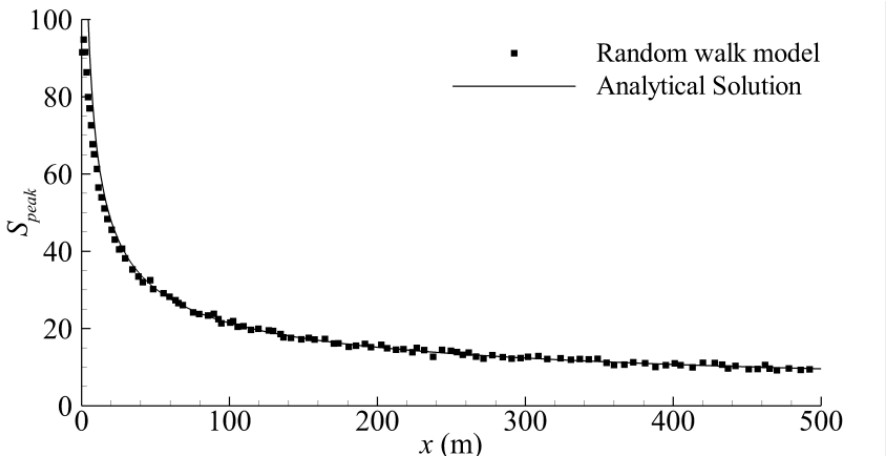

(a) Constant mass discharge

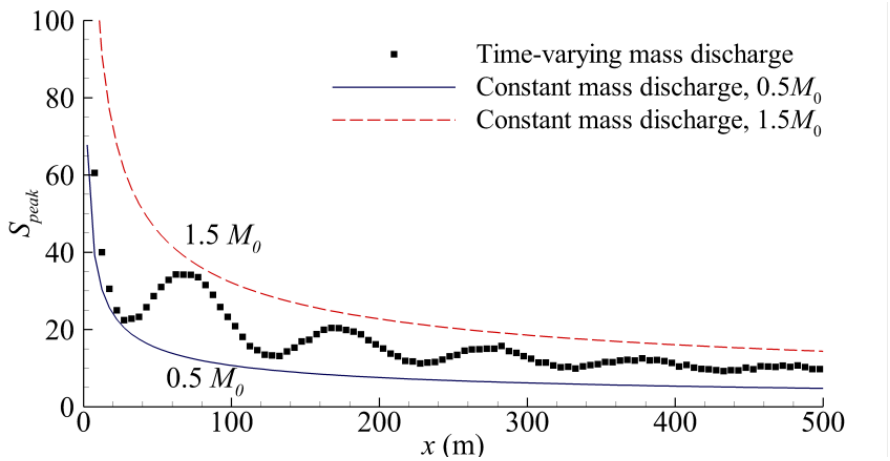

(b) Time-varying mass discharge

Figure 7.2 Profiles of concentrations along the x direction at y = 400 m

Figure 7.2 (a) shows the concentration along centreline of the pollutant cloud predicted by the random walk model, which is perfectly consistent with the analytical solution. When the discharge rate is not constant, then there is no analytical solution. The black square symbols in Figure 7.2 (b) represent the variation of concentrations along the centreline of the pollutant cloud predicted by the random walk model with time-varying mass discharge rate. Here, the time-averaged flow rate is the same as that in Figure 7.2 (a), but it varies from $0.5\dot{M}$ to $1.5\dot{M}$. The predicted results show an overall trend of decrease along the flow but are accompanied by periodic fluctuations. The predicted concentrations are bounded by the analytical solutions with constant mass discharge rates of $0.5\dot{M}$ and $1.5\dot{M}$, which are also plotted in Figure 7.2 (b) as solid and dashed lines, respectively.

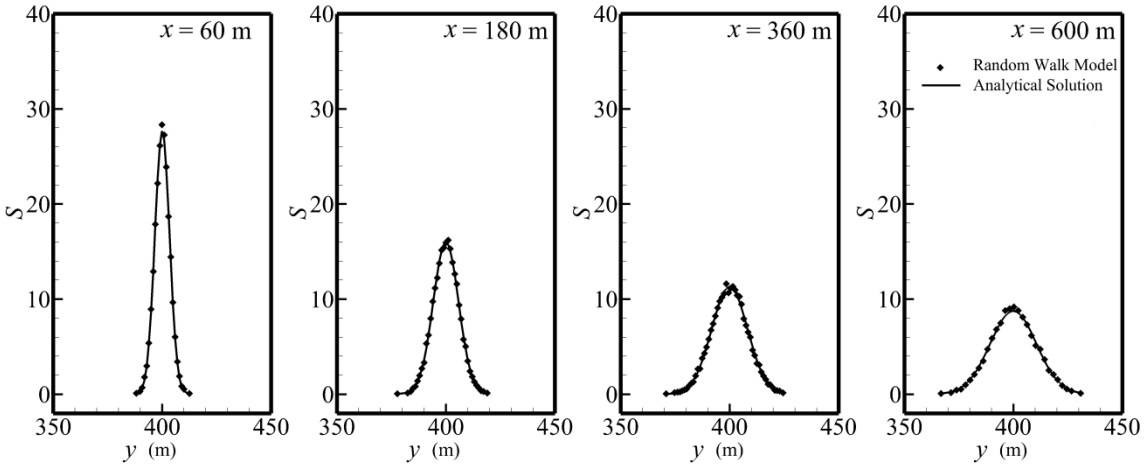

Figure 7.3 Cross-flow concentration distribution at four downstream sections at t = 600 s

As analytical solutions exist for case 1, quantitative comparisons are made between the predicted and theoretical concentration distributions in the cross-flow direction. Figure 7.3 illustrates the concentration profiles at four sections downstream of the source. The concentration distribution follows a Gaussian distribution in the cross-flow direction. The peak concentration gradually decreases while the distribution range increases with the location moving farther away from the discharge point. These results predicted by the random walk model, indicated by square symbols, agree well with the analytical solution, indicated by solid lines.

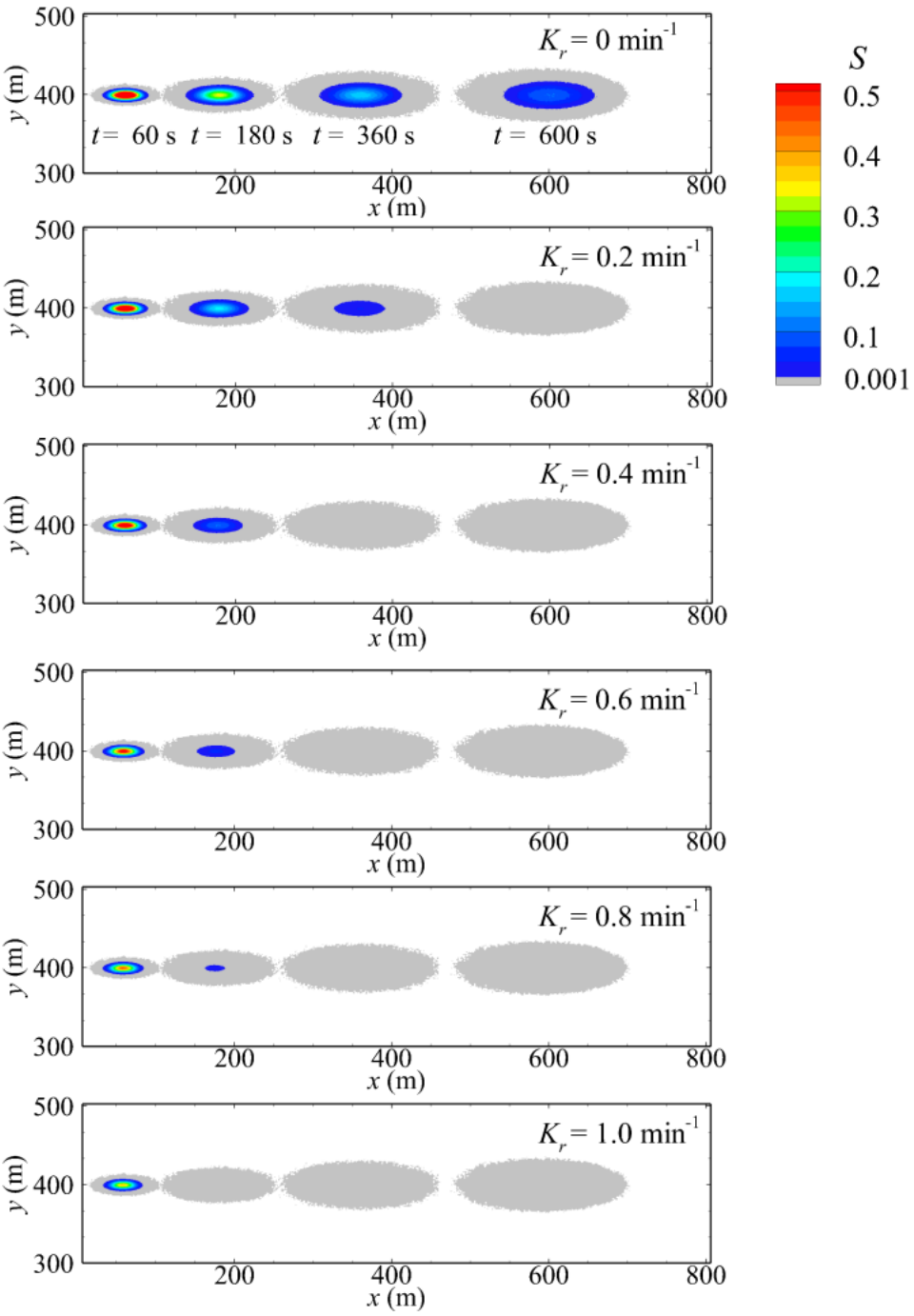

Figure 7.4 Evolution of the pollutant cloud at 30 s, 180 s, 360 s and 600 s

7.2.2 Mass decay

Another ideal test case with known analytical solutions is used in this section to verify the random walk prediction quantitatively. The flow is uniform with u_0 = 1 m/s along the x direction. The water depth H = 1 m, and the Chézy coefficient is 40 m$^{1/2}$/s over the whole test area. The values of ε_s and ε_t are set to be 13.0 and 1.2, respectively. Then, the mixing coefficients are calculated to be $D_{xy} = D_{yx} = 0$, $D_{xx} = D_s = 1.020$ m²/s, $D_{yy} = D_t = 0.094$ m²/s. In this case, the total amount of solute material of M = 233.06 kg is released suddenly at the origin. The material is assumed to be subject to biological decay, which can be expressed as the first-order reaction function, *i.e.* Chick's Law, as given in Equation [7.1]. Then, the analytical solution to this 2-D reaction case can be written as:

$$S(x,y,t) = \frac{M}{4\pi t\sqrt{D_{xx}D_{yy}}} e^{-\frac{(x-x_0-ut)^2}{4D_{xx}t}-\frac{(y-y_0)^2}{4D_{yy}t}-K_r t} \qquad [7.5]$$

The time step Δt of 1 s is adopted. The number of particles released to the computational domain is 2.33 × 10^6. As all the particles are released at t = 0, the value of τ in Equation [7.2] is zero. Each plot in Figure 7.4 corresponds to one decay rate, which includes the predicted concentration contours at four instants: t = 60 s, t = 180 s, t = 360 s and t = 600. A total of six decay rates are considered, *i.e.* K_r = 0 min^{-1}, 0.2 min^{-1}, 0.4 min^{-1}, 0.6 min^{-1}, 0.8 min^{-1} and 1.0 min^{-1}, hence the six plots. In general, these concentration contours are elliptical. Due to the much smaller level of transverse dispersion than that of streamwise dispersion, the solute clouds experienced rapid elongation along the flow direction. The grey colour is used to represent the non-zero solute

concentration that is lower than 0.001 units, indicating where the pollutant is nearly assimilated into the ambient water. In theory, the concentration should be non-zero everywhere in the domain. However, there is a minimum concentration that can be numerically resolved by the random walk method, which is determined by the number of particles deployed. No particles can reach the regions with concentrations smaller than the minimum value, and thus the concentration in these regions will be deemed to be zero in the random walk simulation. A qualitative comparison of the predictions with different decay rates highlights the effect of mass decay over time, which becomes more and more apparent as time progresses. The high-concentration area shrinks rapidly with time, especially with a high decay rate of the non-conservative solute. Taking $K_r = 0.2$ min^{-1} for example, the concentration everywhere in the domain falls below 0.001 units at t = 600 s. As the decay coefficient increases to $K_r = 1.0$ min^{-1}, it takes only 180 s for the concentration everywhere in the domain to fall below 0.001. The quantitative analysis is illustrated in Figure 7.5, which compares the theoretical and predicted maximum concentrations. The results generated by the random walk model, indicated by symbols, are in perfect agreement with analytical solutions, indicated by solid lines. When the solute is assumed to be conservative ($K_r = 0$), the combination of computational parameters produces a peak concentration of unity at t = 60 s. This peak concentration decreases more rapidly with the increase of the decay rate.

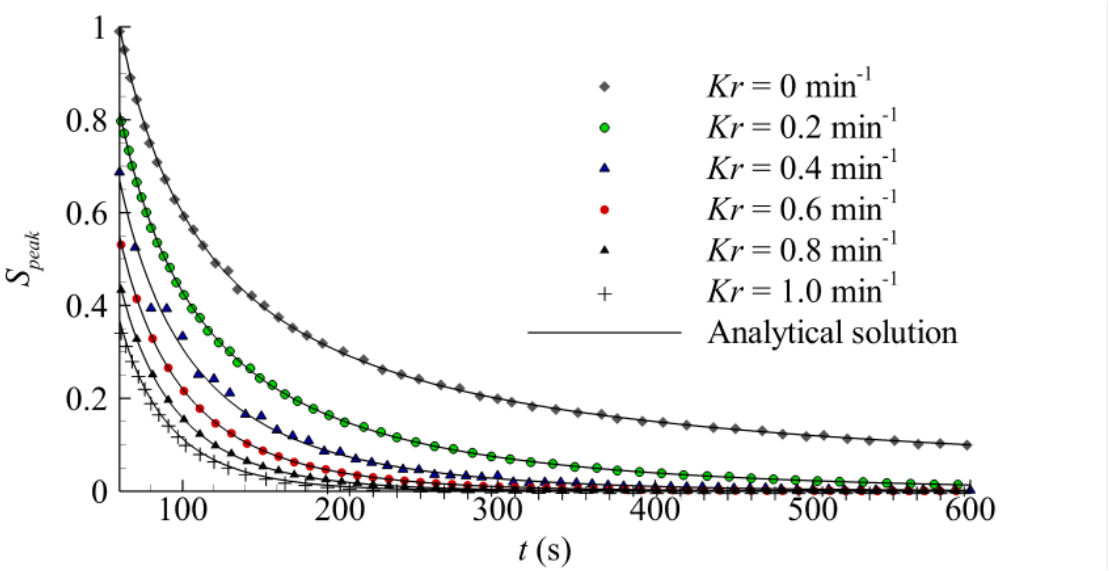

Figure 7.5 Time variations of the peak concentration of the pollutant cloud

7.2.3 BOD-DO model

In this section, the random walk model is applied to predict the variations of the BOD and DO concentrations in uniform flows. An aerial view of a narrow river is illustrated in Figure 7.6, together with the key parameters. In this case, the flow is uniform with u_0 = 0.25 m/s along the river. We use the x to designate the streamwise coordinate in this 1-D river model, so x direction may be curved rather than straight. The water depth is constant at H = 1 m. The traditional BOD-DO interaction model was established by Phelps and Streeter (1958). The concentration of the DO may increase due to re-oxygenation and photosynthesis at the free surface. Wastewater is assumed to be continuously discharged into the narrow river at a constant rate. The distribution of the solute is steady and can be assumed to be totally mixed over a cross-section.

Then, the relationship between the BOD and DO concentrations can be simplified as follows:

$$U\frac{dS_{BOD}}{dx} = -K_r S \quad [7.6]$$

$$U\frac{dS_{DO}}{dx} = K_a(S_{DOsat} - S_{DO}) - K_r S_{BOD} \quad [7.7]$$

The analytical solution to the Equations [7.6] to [7.7] can be expressed as:

$$S_{BOD} = S_{BOD0}e^{-K_r x/U} \quad [7.8]$$

$$S_{DO} = S_{DOsat} - S_{BOD0}\frac{K_r}{K_a - K_r}\left[e^{-\frac{K_r x}{U}} - e^{-\frac{K_a x}{U}}\right] - (S_{DOsat} - S_{DO0})e^{-K_a x/U} \quad [7.9]$$

where S_{DO0} and S_{BOD0} are DO and BOD concentrations, respectively, at origin x = 0; S_{DOsat} is the saturated DO concentration in water; K_r is the BOD deoxygenation rate and K_a is the re-oxygenation rate.

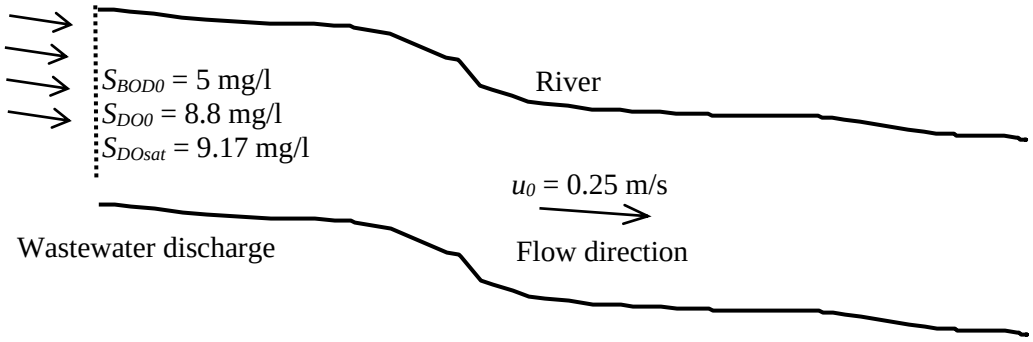

Figure 7.6 Continuous discharge of wastewater in the uniform flow

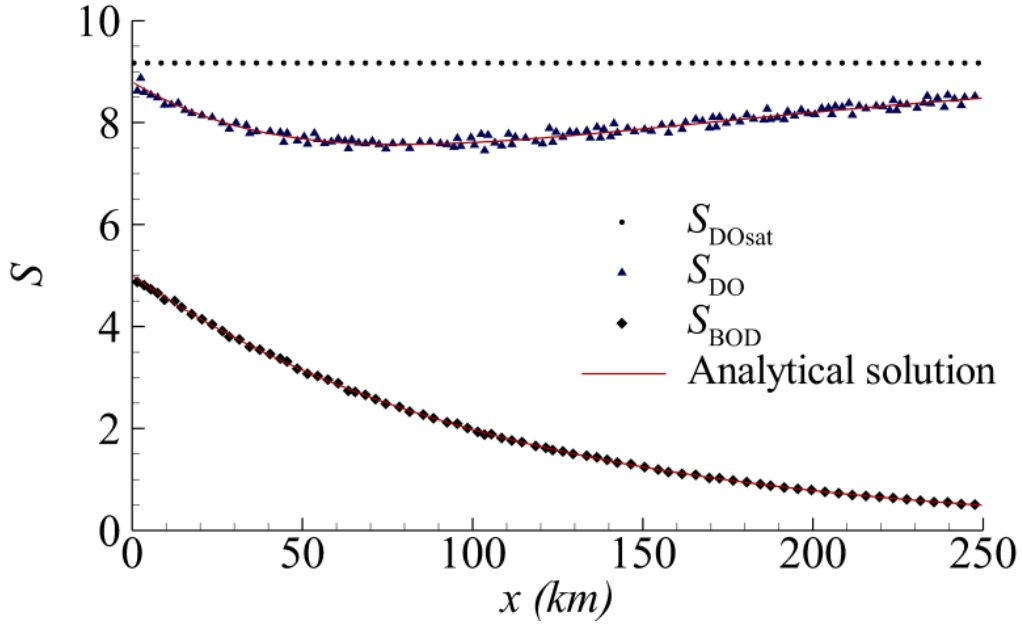

(a) Profile of BOD and DO concentrations

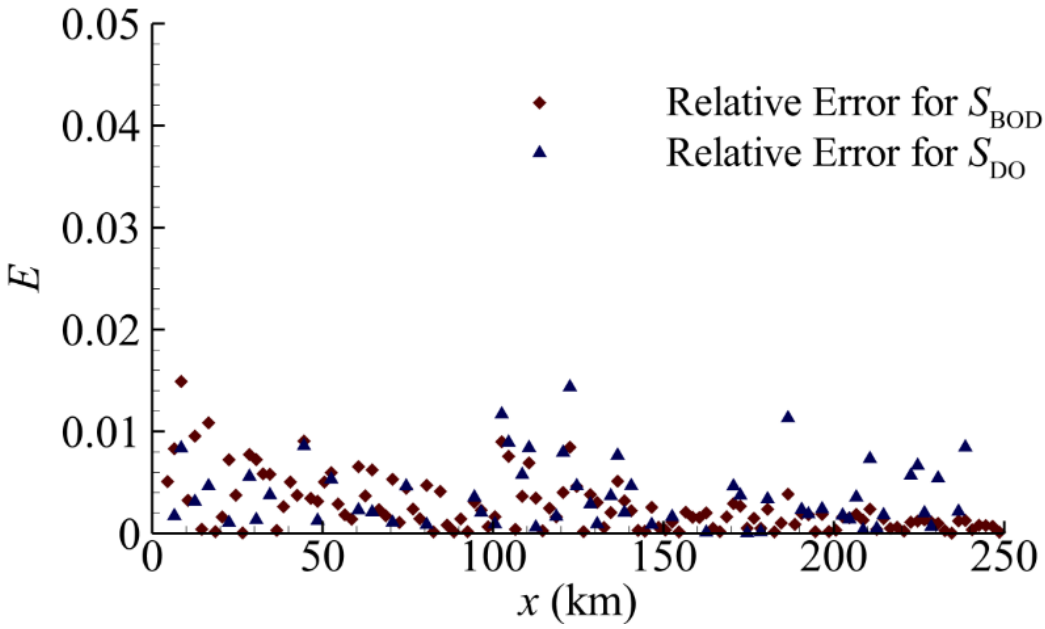

(b) Relative errors for BOD and DO predictions

Figure 7.7 Variations of BOD and DO concentrations and prediction errors along x direction

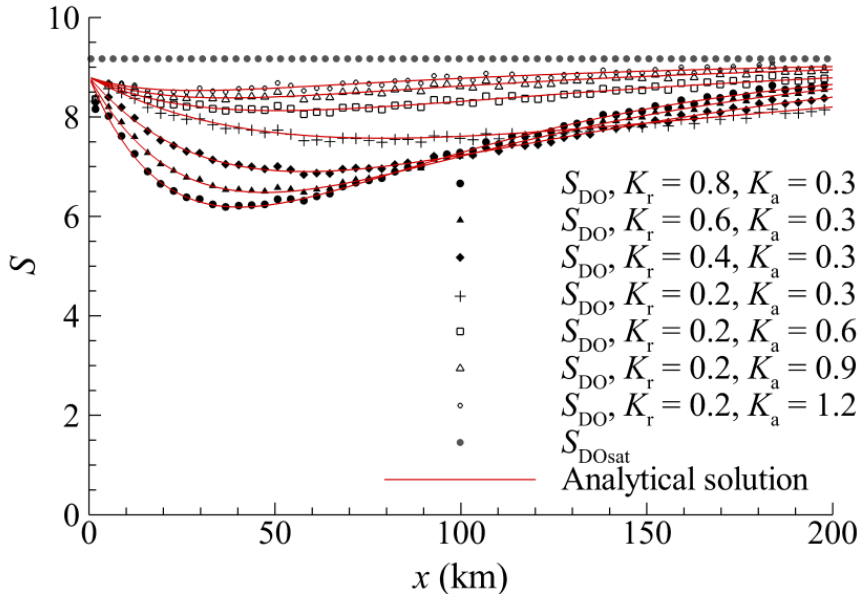

(a) Profiles of DO concentration

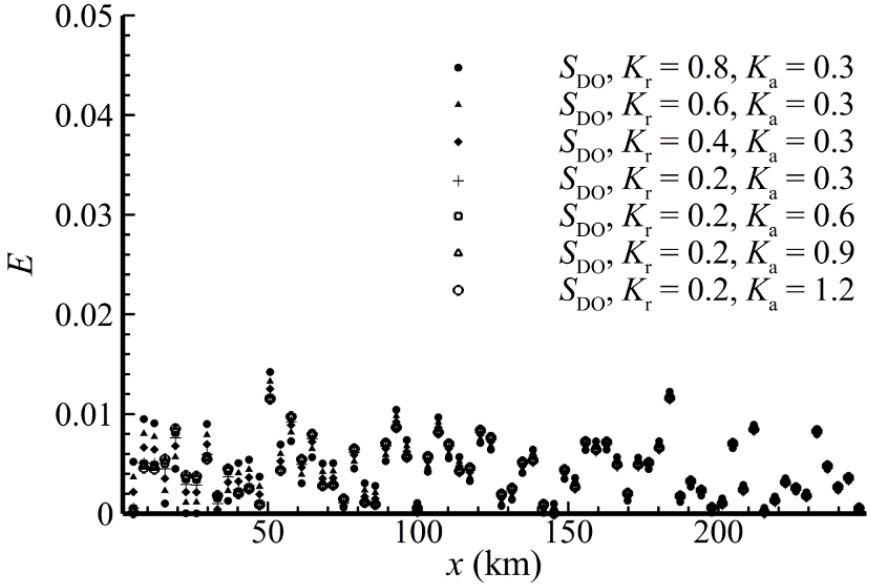

(b) Relative errors for DO predictions

Figure 7.8 Variations of DO concentration and prediction errors along x direction for different combinations of K_r and K_a

In random walk modelling, the original unsteady advection-diffusion-reaction equations are solved. Two sets of particles are used as BOD and DO indicators, respectively. In the simulation, K_r is set to be 0.2 per day while K_a is set to be 0.3 per day. The sewage effluent contains BOD of 5 mg/l and DO of 8.8 mg/l. The saturation concentration of oxygen in water at 20 ^{o}C is 9.17 mg/l. The time step is $\Delta t = 1$ s. The number of particles released to the computational domain is 10^3 per time step. Figure 7.7 (a) compares the numerical results of the random walk model, indicated by symbols, and the analytical solutions, indicated by solid lines, for the corresponding BOD decay curve and DO sag curve. It can be seen that the predicted results agree well with the analytical solutions. An error analysis is performed by calculating the relative error of each predicted concentration as follows:

$$E = \frac{|S_{predicted} - S_{analytical}|}{S_{analytical}} \qquad [7.10]$$

where E gives the relative difference between the predicted concentration $S_{predicted}$ and the analytical solution $S_{analytical}$. As seen in Figure 7.7 (b), the relative error of any predicted concentration, in comparison with the analytical value, is less than 1.6 % in all cases.

Figure 7.8 (a) illustrates the DO concentration profile with a series combination of BOD deoxygenation rate K_r and re-oxygenation rate K_a. As K_a increases, the DO distribution curve becomes flatter and approaches the value of S_{DOsat} more rapidly. On the contrary, the DO curve sags more and approaches the asymptotic value more slowly when the BOD deoxygenation rate K_r gets larger. It can be concluded that the BOD deoxygenation rate K_r has a greater influence on the DO concentration. Figure 7.8 (b) presents the error analysis for

the different combinations of the reaction constants. Again, all the relative errors are less than 1.6%. Overall, the numerical results predicted by the current random walk model agree well with the theoretical solutions.

7.3 Model application to Thames Estuary

In the previous section, the performance of the random walk model has been tested in three idealised examples. In this section, the validated random walk model is applied to predict the BOD-DO interaction in the Thames Estuary. The Thames Estuary is located in the southeast of the UK, where the River Thames meets the North Sea, as seen in Figure 7.9. The unsteady flow field has been obtained by solving the SWEs using the TVD-MacCormack scheme (Mingham et al. 2001, Liang et al. 2006 and 2010) on rectangular mesh. This method has been widely used for simulating hydro-environmental dynamics and is taken as a representative mesh-based method here.

Figure 7.9 Geographic location of River Thames (photo source: Google map)

Figure 7.10 presents a typical water depth distribution in the Thames Estuary. In terms of the fluvial inputs from upstream, only the River Thames and River Medway are considered in the simulation. A number of assumptions are adopted in this real-world example. The variations of the water level at the seaward boundaries are assumed to follow a sinusoidal function. The average sea level is assumed to be 0.05 m above the Newlyn Datum, and the tidal period is 12 h with amplitude of 3.02 m. Manning roughness values are specified according to the bed condition. The value for the normal seabed is 0.02 s/m$^{1/3}$, while the value for tidal floodplains covered with vegetation is 0.13 s/m$^{1/3}$. The computational mesh used by the shallow water solver consists of 1250 × 500 square elements of equal size with a side length of 80 m. The time variations of the velocities and water depths stored on this mesh are fed into the random walk model to drive the pollutant transport processes. The time step is set to be 1 s in the random walk model. Typical values of $\varepsilon_s = 13.0$ and $\varepsilon_t = 1.2$ are used again for the longitudinal dispersion and turbulent diffusion coefficients, respectively.

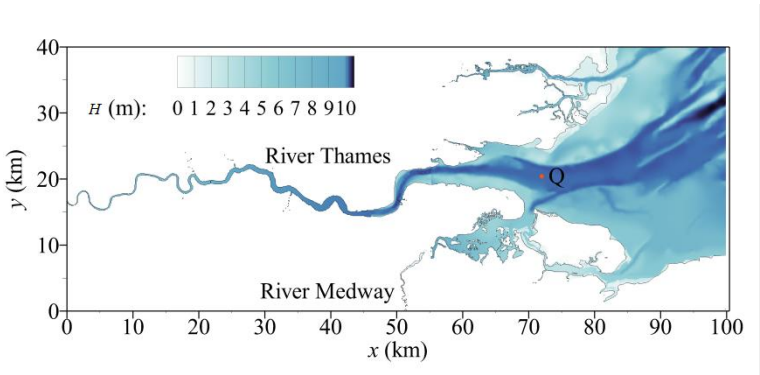

(a) 3 hours

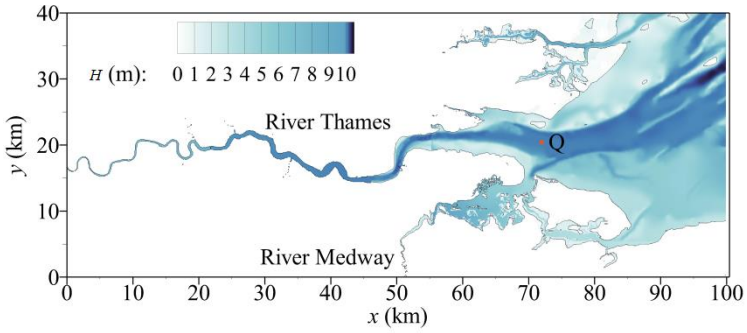

(b) 6 hours

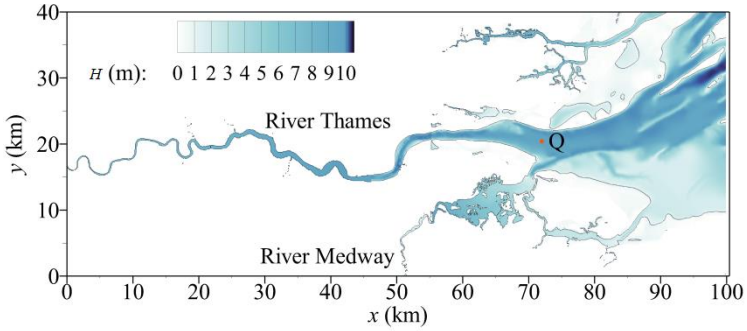

(c) 9 hours

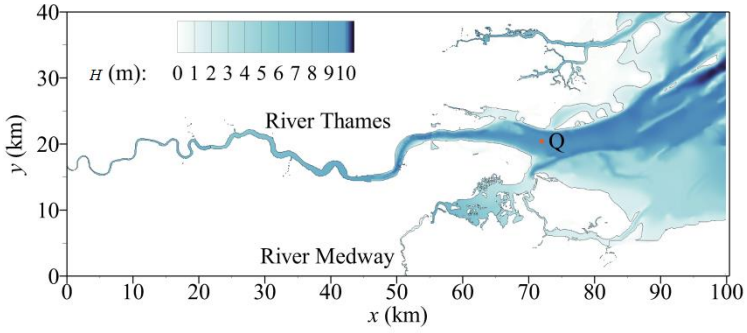

(d) 12 hours

Figure 7.10 Typical water depth distributions at 3 hours, 6 hours, 9 hours, and 12 hours in the Thames Estuary, superimposed with the discharge point Q

Two hypothetical release scenarios are considered. The first scenario is consistent with previous research in Liang et al. (2010) for comparison purpose. It is assumed that the waste effluent is suddenly discharged into the tidal flow from location Q (x_0, y_0) = (72 km, 20.4 km) within 10 min. The total number of particles released is 1.95×10^5. Only one non-conservative material is considered in this scenario. The variation of the total discharge rate Q_s with time is shown in Figure 7.11. In the mesh-based modelling, the discharge is introduced to a computational element and so it is equal to q_s times the area of the element. In the random walk method, no mesh is used, and the effluent is exactly located at point (x_0, y_0).

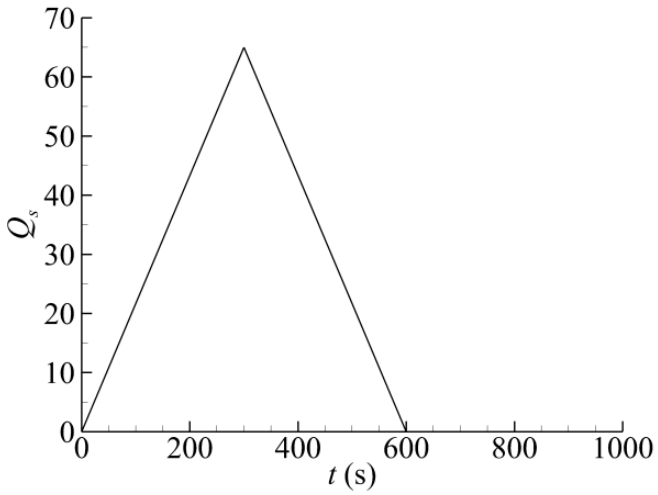

Figure 7.11 Total discharge rate Q_s at release point Q (x_0, y_0) = (72 km, 20.4 km)

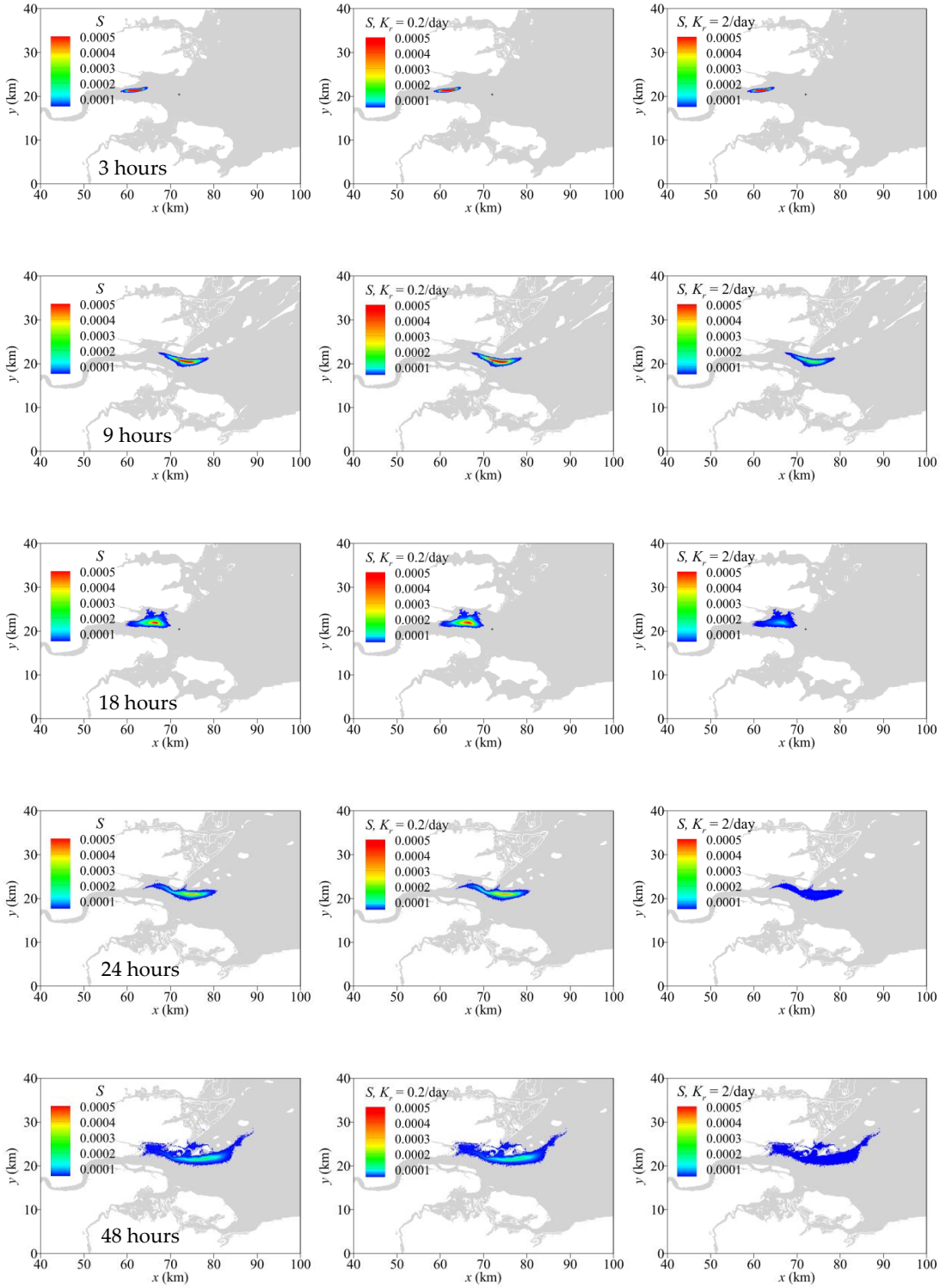

Figure 7.12 Snapshots of solute clouds in the Thames Estuary at 3 hours, 6 hours, 9 hours, 18 hours, 24 hours and 48 hours after the release

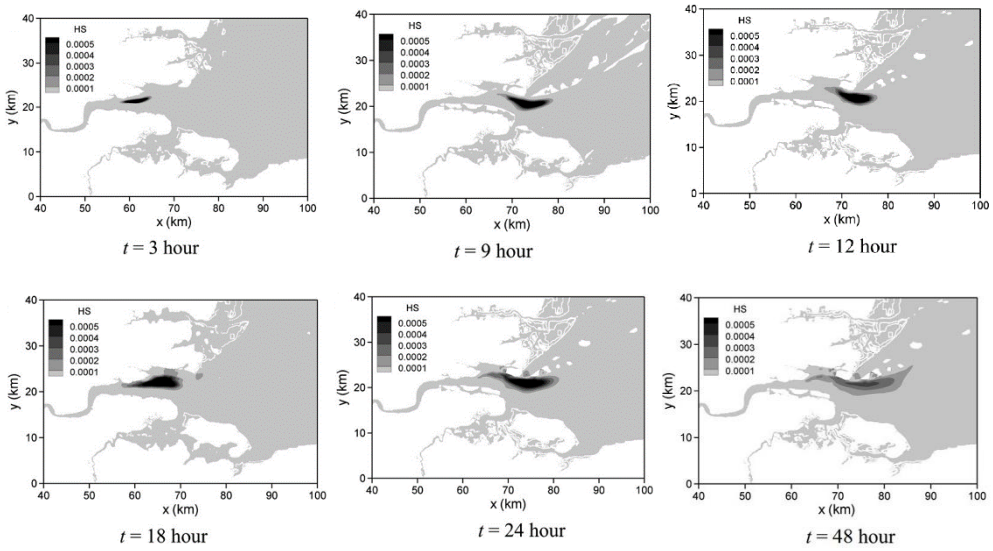

Figure 7.13 Pollutant concentration field for the Thames Estuary predicted by TVD-MacCormack method (Liang et al. 2010)

Figures 7.12 display a sequence of the concentration snapshots over the domain predicted by the 2-D random walk model. The grey colour represents the wet areas where the domain is occupied with water. As expected, the pollutant cloud oscillates back and forth with the tidal currents. In the first tidal cycle, the solute spreads over a broader area and becomes less concentrated as time progresses. The mesh-based TVD-MacCormack method had been applied to the same case in Liang et al. (2010), as shown in Figure 7.13. By comparison, the random walk model gives an even higher resolution of the concentration distribution, as the random walk method suffers no numerical diffusion. On the contrary, the mesh-based approaches suffer from numerical diffusion unless the computational mesh is very fine. As for the computational cost, it depends on the number of particles and the time step used in the random walk modelling. The current simulation time is around 8 hours on a Dell Optiplex 790 computer for 48 hours of the transport process. The substance released in

the tidal flow is assumed to be subject to biological transformation. The decay is expressed as the first-order reaction function, as shown in Equation [7.1]. In Figure 7.12, each graph shows the predicted concentration contours with one decay rate at one instant. It can be seen that the concentration of non-conservative solute decreases rapidly with the increase of the decay rate and with the increase of time. The good comparison between predictions using this model and those based Euler methods indicates that the current random walk model is capable of modelling the transport of non-conservative materials in real-world scenarios with unsteady flows over uneven bed elevations and irregular geometries.

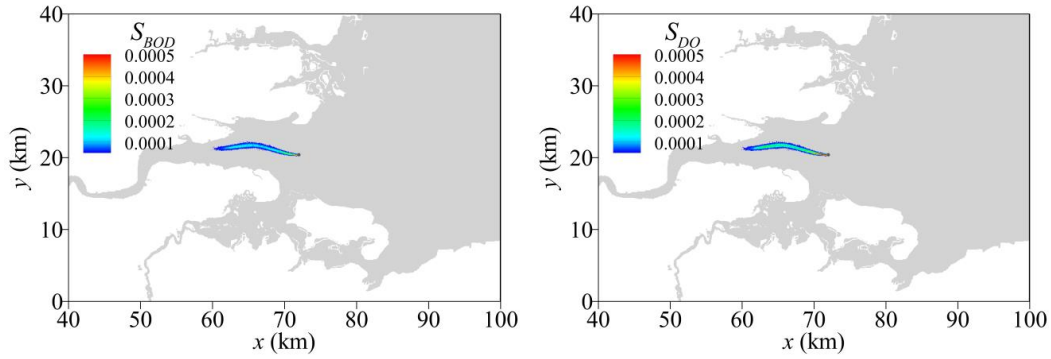

(a) t = 3 hours

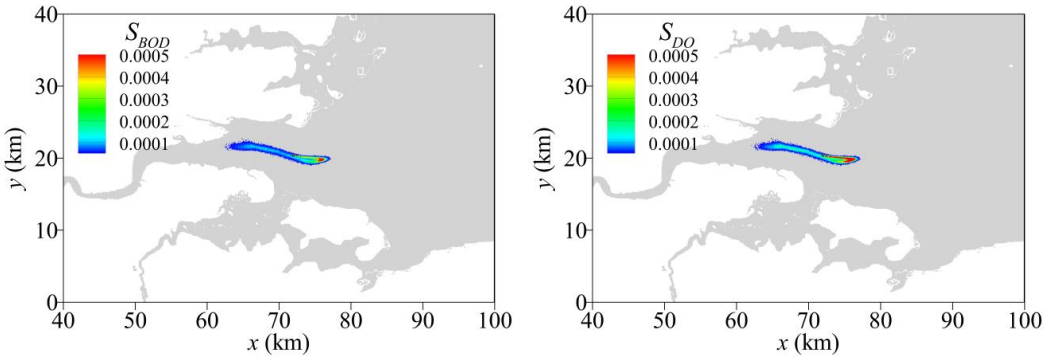

(b) t = 6 hours

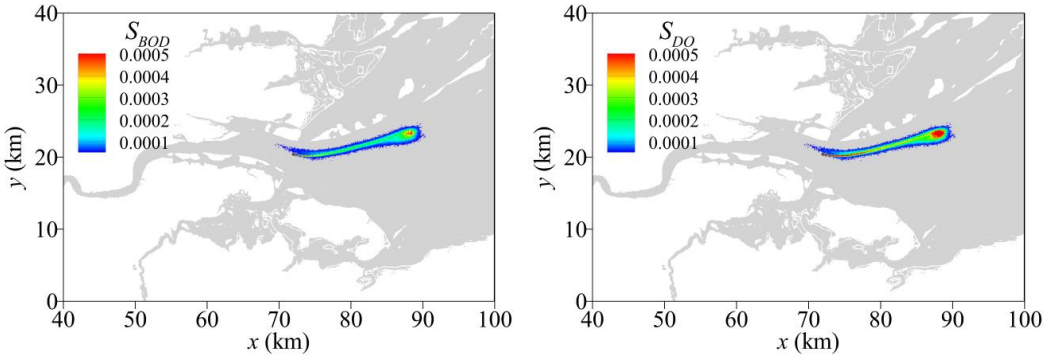

(c) t = 9 hours

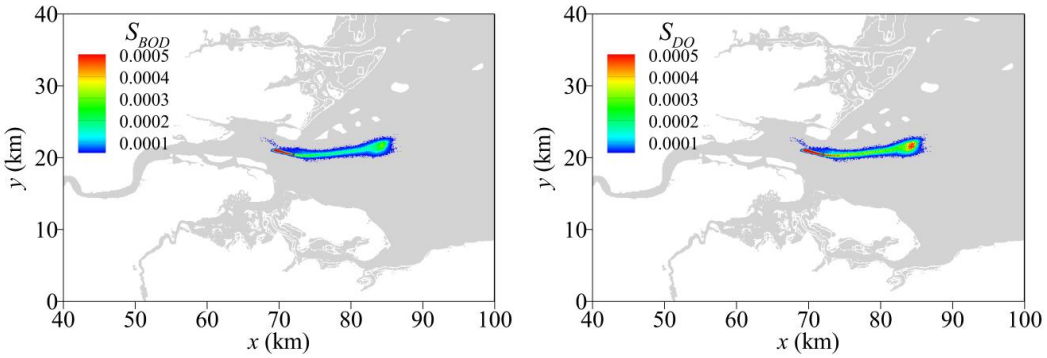

(d) t = 12 hours

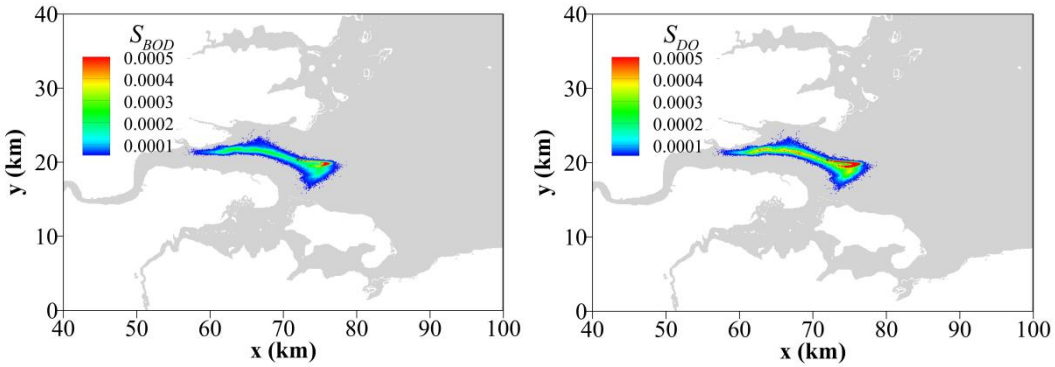

(e) t = 18 hours

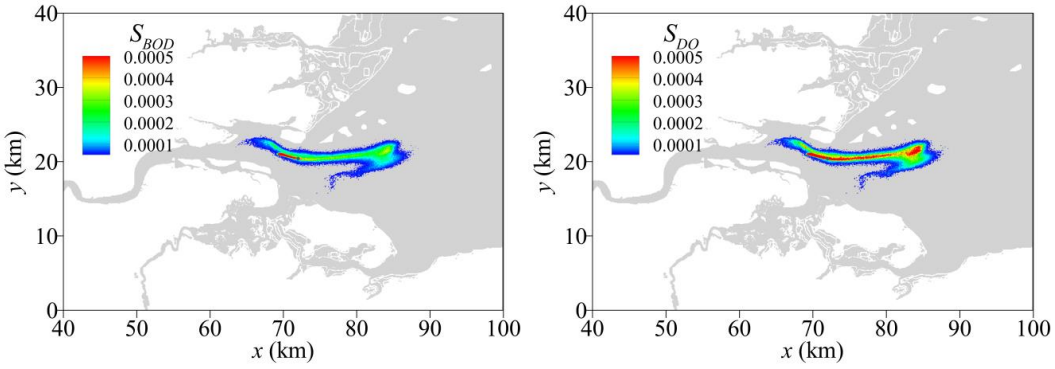

(f) t = 24 hours

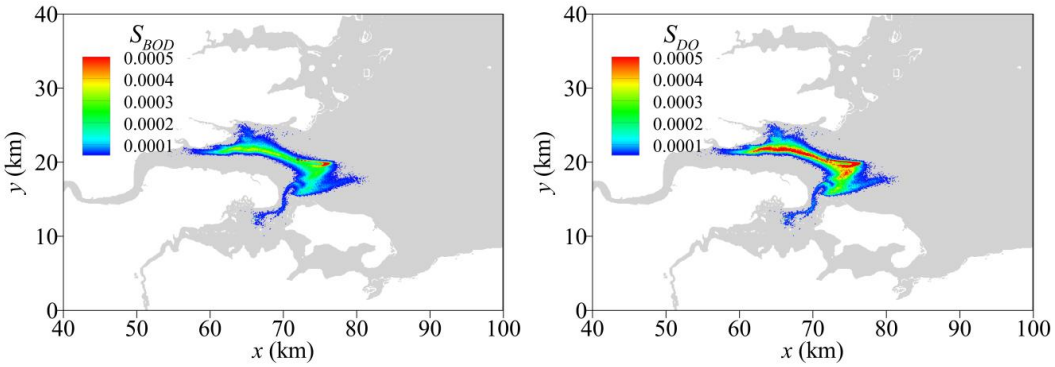

(g) t = 30 hours

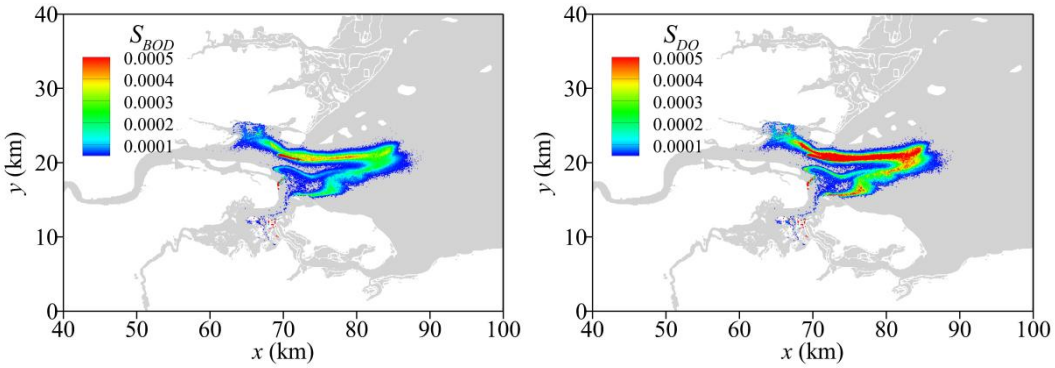

(h) t = 48 hours

Figure 7.14 Snapshots of the BOD (left) and DO (right) distributions in the Thames Estuary

The other release scenario considered is that the wastewater is continuously discharged into the Thames estuary. Both the BOD and DO concentrations are considered to examine the 2-D random walk model under this complicated tidal flow condition. In the simulation, K_r is set to be 0.2 per day while K_a is set to be 0.3 per day. The wastewater contains BOD of 5 mg/l and DO of 8.8 mg/l at the release point. The saturation concentration of oxygen in water at 20 ^{o}C is 9.17 mg/l. The number of particles released per time step is set to be 10^3. Figure 7.14 shows the snapshots of BOD and DO concentration fields at six instants. At t = 3 hours, the solute cloud spreads from the release point to the upper reaches of the River Thames. It is notable that the closer to the release point, the higher the concentration. The results at this instant are similar to the trend observed in Figure 7.1 (b). After a half tidal cycle, as seen in Figure 7.14 (b), the clouds make a sharp U-turn and move towards the North Sea. Such a behaviour is reasonable as flow field changes direction as the tide switches into the ebbing stage. As seen in Figure 7.14 (c) and (d), there are two locally high-concentration patches in the DO concentration contours at 9 and 12 hours, one at the release point and the other at the location (x, y) = (88 km, 23 km) where the pollutant returns from the North Sea during the second half of the tidal cycle. At t = 30 hours, Figure 7.14 (g) shows that the wastewater reaches the mouth of the River Medway. The solute cloud continues to oscillate back and forth with the tidal currents and spreads over a broader area as time progresses.

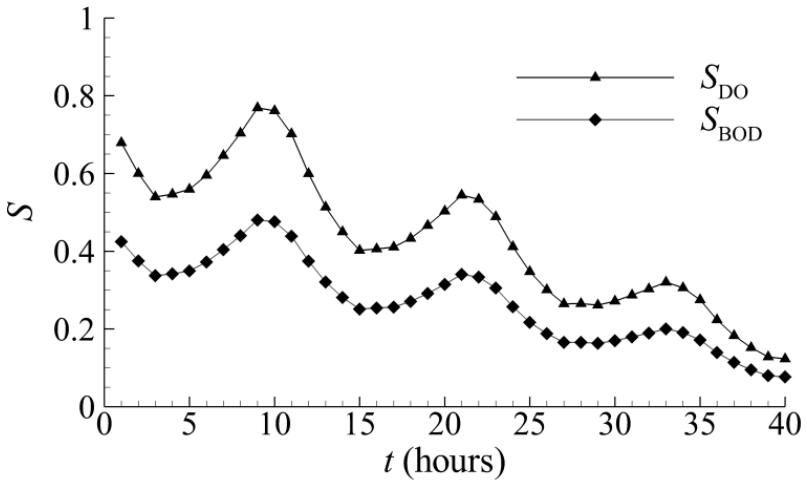

Figure 7.15 Time developments of the BOD and DO peak concentration in the Thames Estuary

In the previous discussion, the solute clouds oscillate back and forth with the tidal currents and become less concentrated as time progresses. Such phenomena are correspondingly evident in Figure 7.15. The temporal evolution of the maximum concentration is subject to periodic fluctuations, although an overall downward trend is evident. The period of 12 hours is consistent with the period of the tide flow.

7.4 Chapter summary

In this chapter, the depth-averaged random walk model is developed to investigate non-conservative solute transport processes in shallow water flows. Idealised cases are modelled to examine the capability of the present random walk method in addressing the instantaneous and continuous release of non-conservative substances in the simulations. The model was first applied to an

ideal continuous release problem. The influence of the decay rate on the predictions is also investigated in the second test case. Then, the model is applied to solve a hypothetical BOD-DO balance problem in a 1-D uniform flow. The numerical predictions of the solute advection, diffusion and reaction processes are in good agreement with analytical solutions. Finally, the validated random walk model is successfully applied to predict two scenarios in the Thames Estuary, including the short-duration and continuous release cases. For the case of short-duration release of a conservative material, the random walk predictions agree well with the conventional numerical results based on fine meshes. In the case of continuous discharge of wastewater into the Thames Estuary, the coupling of the BOD and DO is satisfactorily reproduced. The peak concentration of the degradable solute periodically fluctuates with time, with a period consistent with the specified tidal period.

Chapter 8

Conclusion and Future Work

A conclusion for this thesis is presented in the first part of the chapter. It lists main research work carried out in both hydrodynamic modelling and solute transport modelling parts. This is followed by the summary of main findings and relevant limitations of each part of this study. Suggestions on further improvement of the random walk model and future works are included.

8.1 Conclusion

This thesis is concerned with the numerical modelling of rapid flows, solute transport processes and biochemical reactions in shallow water environment. It starts with the review of previous modelling approaches in the general field of hydro-environmental modelling. This is followed by the

explanations of the governing equations employed for shallow flows and the mass transport processes.

In the hydrodynamic modelling part, the consequences of modifying the Boussinesq coefficient in modelling rapid flows have been assessed in a wide range of flow conditions. Firstly, comparison is made between the ADI and TVD-MacCormack models concerning 1-D and 2-D dam-break floods over frictionless and flat beds. In these cases, the results suggest that the amplitude of the spurious oscillations decreases with the increase of the Boussinesq coefficient. Hence, use of a large β value helps the ADI model to overcome its inherent instability when simulating rapidly varying dam-break flows. It is also found that increasing the value of β increases the propagation speed of flood waves when modelling unsteady flows over a frictionless bed. However, opposite results are observed for steady flows with a frictional bed. The results in these situations suggest that the amplitude of the spurious oscillations decreases with the decrease of the Boussinesq coefficient. Meanwhile, the steady water surface elevation is predicted to be lower with a smaller β value. Finally, the simulation of a flash flood over a complex urban terrain has been studied and the impact of the β coefficient on the solution of the ADI model is further examined for unsteady flow over a frictional bed. The results indicate that increase in the Boussinesq coefficient can significantly reduce the amplitude of the numerical oscillations in the ADI simulations. The inundated area gradually reduces as the coefficient increases. These results show the complicated relationship between the β value and the computational results, which depends on whether the flow is steady or unsteady and whether the bed

is frictionless or frictional. The findings provide guidelines for evaluating the accuracy of the flood modelling software based on ADI schemes.

In the solute transport modelling part, the performance of the depth-averaged random walk model is examined for 2-D solute transport modelling. Most previous numerical studies on the solute transport problems rely on the mesh-based methods, and various sophisticated high-order accurate schemes have been developed to enhance the numerical stability and reduce the artificial diffusion associated with the advective transport process. This thesis systematically studies the depth-averaged random walk scheme, which is a meshfree method with the merits of being highly robust. However, it is worth noting that the random walk method does have some drawbacks such as artificial diffusion when interpolating the particle tracking results to a grid and the unknown number of particles that must be determined by trial and error. Firstly, this model is verified by solving an instantaneous release problem in uniform flows. Analytical solutions are used as a reference. The results reveal several merits of this model, including high accuracy and small numerical diffusion. Extensive parametric studies have been carried out to investigate the sensitivity of the predictions to the computational parameters. It has been found that simulations for steady flows are independent of the size of the time step. The particle number significantly influences the performance of the random walk model. Too few particles not only degrade the visual inspection of solute distribution, but also produce unacceptable errors. Simulations with sufficient particle numbers can achieve good accuracy with little numerical dissipation. In applications, a relatively large time step will reduce the computation expense without compromising accuracy. Then, investigations

are carried out regarding the oscillation of a pollutant cloud in a 1-D tide estuary. Sampling processes have been optimised to acquire more accurate concentration profiles. The results demonstrate reasonable features of the temporal and spatial variations, which agree well with the previous results based on fine meshes. Finally, the random walk model is applied to simulate the chaotic mixing process in a circular lake. From a qualitative point of view, the results for pure advection process are consistent with the findings reported in previous research. Because of the bottom friction that is present in any real lake, the pure advection process is always accompanied by the longitudinal dispersion process. This study shows that diffusion plays an important role in the mixing. The well-structured chaotic mixing pattern produced by pure advection cannot be observed in reality. Grid-based methods have been proved to be sensitive to grid resolution. The results of the random walk model are free of numerical dispersion and display encouraging efficiency and accuracy in solving the solute transport problems in aquatic environments.

In the final part of the thesis, the random walk model has been extended to investigate complex hydro-environmental phenomena that involve the transport of non-conservative materials. Idealised cases are modelled to examine the capability of the present random walk method in addressing the instantaneous and continuous release of non-conservative substances in the simulations. The model was first applied to an ideal continuous release problem. The influence of the decay rate on the predictions is also investigated in the second test case. Then, the model is applied to solve a hypothetical BOD-DO balance problem in a 1-D uniform flow. The numerical predictions of the solute advection, diffusion and reaction processes are in good agreement with

analytical solutions. Finally, the validated random walk model is successfully applied to predict two scenarios in the Thames Estuary, including the short-duration and continuous release cases. For the case of short-duration release of a conservative material, the random walk predictions agree well with the conventional numerical results based on fine meshes. In the case of continuous discharge of wastewater into the Thames Estuary, the coupling of the BOD and DO is satisfactorily reproduced. The peak concentration of the degradable solute periodically fluctuates with time, with a period consistent with the specified tidal period. The model developed in this paper is shown to be capable of modelling continuous release of non-conservative pollutants and the interaction between pollutants.

8.2 Future work

In extending the research for further study, the following aspects are worthy of consideration:

- Numerical treatments combinations

In the rapid varying flow modelling, two widely adopted numerical treatments are available for stabilising the traditional scheme in simulating rapid flows. One is to introduce artificial diffusion, and the other one is to modify the Boussinesq coefficient. Previously, the effect of artificial viscosity on the computational results has been extensively studied. In this thesis, the impact of modifying the Boussinesq coefficient over a range of flow conditions has been comprehensively studied. However, the combined impact of the two numerical treatments is not well understood yet. The future work in this part

could focus on the comprehensive study on the combined numerical treatments.

- Multiple non-conservative substance interactions

In the solute transport modelling, only a maximum of two non-conservative pollutants are considered. In the future, we could extend the present random walk model to include more water quality indicators capable of conducting water quality analyses in more complicated real-world situations.

- High-order decay processes

In the solute transport modelling, only the first-order reaction is considered. The mass attached to each particle is simply reduced at each timestep. For higher order processes, the situation is more complex. For example, when a rate of decay depends on the concentration, the superposition no longer applies. Concentrations must first be calculated before the transformation or reaction can be applied. After the transformation or reaction, the overall concentrations must be redistributed into discrete particles. This opens the possibility of modelling more complicated interaction processes with high-order decay processes.

Bibliography

Ambrose Jr, R. B., Wool, T. A., Conolly, J. P., & Scahnz, R. W. (1988). A Hydrodynamic and Water Quality Model: Model Theory, Users Manual, and Programmers manual: WASP4 Environmental Research Laboratory, US EPA. EPA 600/3-87/039, Athens, GA.

Bates, P. D., Horritt, M., & Hervouet, J. M. (1998). Investigating two-dimensional, finite element predictions of floodplain inundation using fractal generated topography. Hydrological processes, 12(8), 1257-1277.

Bates, P. D., Horritt, M. S., & Fewtrell, T. J. (2010). A simple inertial formulation of the shallow water equations for efficient two-dimensional flood inundation modelling. Journal of Hydrology, 387(1-2), 33-45.

BBC (2020). Severe floods engulf eastern China. [Online; Accessed on 2020-8-28]. https://www.bbc.com/news/world-asia-china-53434767

Begnudelli, L., & Sanders, B. F. (2006). Unstructured grid finite-volume algorithm for shallow-water flow and scalar transport with wetting and drying. Journal of hydraulic engineering, 132(4), 371-384.

Benkhaldoun, F., Elmahi, I., & Seaı, M. (2007). Well-balanced finite volume schemes for pollutant transport by shallow water equations on unstructured meshes. Journal of computational physics, 226(1), 180-203.

Bidwell, V. J. (1971). Regression analysis of nonlinear catchment systems. Water Resources Research, 7(5), 1118-1126.

Brunner, G. W. (2002). Hec-ras (river analysis system). In North American Water and Environment Congress & Destructive Water (pp. 3782-3787). ASCE.

Bryc, W. (2012). The normal distribution: characterizations with applications (Vol. 100). Springer Science & Business Media.

Burguete, J., García-Navarro, P., & Murillo, J. (2006). Numerical boundary conditions for globally mass conservative methods to solve the shallow-water equations and applied to river flow. International journal for numerical methods in fluids, 51(6), 585-615.

Casulli, V. (1990). Semi-implicit finite difference methods for the two-dimensional shallow water equations. Journal of Computational Physics, 86(1), 56-74.

Castanedo, S., Medina, R., & Mendez, F. J. (2005). Models for the turbulent diffusion terms of shallow water equations. Journal of Hydraulic Engineering, 131(3), 217-223.

Cea, L., Puertas, J., & Vázquez-Cendón, M. E. (2007). Depth averaged modelling of turbulent shallow water flow with wet-dry fronts. Archives of Computational Methods in Engineering, 14(3), 303-341.

Chanson, H. (2005). Analytical solution of dam break wave with flow resistance: Application to tsunami surges. In 31st IAHR Congress 2005: Water Engineering for the Future, Choices and Challenges pp. 3341-3353. Chapra, S. C. (2008). Surface water-quality modeling. Waveland press.

Chiu, C. L., & Huang, J. T. (1970). Nonlinear time varying model of rainfall-runoff relation. Water Resources Research, 6(5), 1277-1286.

Costabile, P., Costanzo, C., & Macchione, F. (2012). Comparative analysis of overland flow models using finite volume schemes. Journal of hydroinformatics, 14(1), 122-135.

Crawford, N. H., & Linsley, R. K. (1966). Digital Simulation in Hydrology'Stanford Watershed Model 4.

DHI, M. P. B. (2018). MIKE powered by DHI. Retrieved from MIKE Powered by DHI: https://www. mikepoweredbydhi. com.

Dodds, W.K., Bouska, W.W., Eitzmann, J.L., Pilger, T.J., Pitts, K.L., Riley, A.J., Schloesser, J.T. and Thornbrugh, D.J. (2009). Eutrophication of US freshwaters: analysis of potential economic damages. 12-19

Falconer, R. A. (1986). A 2-D mathematical model study of the nitrate levels in an inland natural basin. In International conference on water quality modelling in the inland naturel environment pp. 325-344

Falconer, R. A. (1991). Review of modelling flow and pollutant transport processes in hydraulic basins. In Water pollution: Modelling, measuring and prediction Springer, Dordrecht. pp. 3-23

Falconer, R. A., Lin, B., Wu, Y., & Harries, E. (2001). DIVAST model: reference manual. Environmental Management Research Centre, Cardiff University.

Fraccarollo, L., & Toro, E. F. (1995). Experimental and numerical assessment of the shallow water model for two-dimensional dam-break type problems. Journal of hydraulic research, 33(6), 843-864.

Goldstein, S. (1938). Modern Developments in Fluid Dynamics, vol. 1. Oxford University Press, England.

Grenney, W. J., Teuscher, M. C., & Dixon, L. S. (1978). Characteristics of the solution algorithms for the QUAL II river model. Journal (Water Pollution Control Federation), 151-157.

Gresho, P. M., & Sani, R. L. (1998). Incompressible flow and the finite element method. Volume 1: Advection-diffusion and isothermal laminar flow.

Gupta, I., Dhage, S., Chandorkar, A. A., & Srivastav, A. (2004). Numerical modeling for Thane creek. Environmental Modelling & Software, 19(6), 571-579.

Hervouet, J. M. (2007). Hydrodynamics of free surface flows: modelling with the finite element method (Vol. 360). New York: Wiley.

Hinkelmann, R., Liang, Q., Aizinger, V., & Dawson, C. (2015). Robust shallow water models. International Journal Environmental Earth Sciences, Vol. 74, No. 11.

Hou, J., Liang, Q., Simons, F., & Hinkelmann, R. (2013). A 2D well-balanced shallow flow model for unstructured grids with novel slope source term treatment. Advances in Water Resources, 52, 107-131.

HR Wallingford. (2005). Flooding in Boscastle and North Cornwall, August 2004: Phase 2 Studies Report. Release 1.0. HR Wallingford Limited.

Hunt, B. (1999). Dispersion model for mountain streams. Journal of Hydraulic Engineering, 125(2), 99-105.

Hunter, J. R., Craig, P. D., & Phillips, H. E. (1993). On the use of random walk models with spatially variable diffusivity. Journal of Computational Physics, 106(2), 366-376.

Hunter, N.M., Bates, P.D., Neelz, S., Pender, G., Villanueva, I., Wright, N.G., Liang, D., Falconer, R.A., Lin, B., Waller, S., Crossley, A.J., Mason, D.C.,

(2008). Benchmarking 2D hydraulic models for urban flood simulations. Proc. Inst. Civ. Eng. Water Manage. 161 (1), 13–30.

Israelsson, P. H., Do Kim, Y., & Adams, E. E. (2006). A comparison of three Lagrangian approaches for extending near field mixing calculations. Environmental Modelling & Software, 21(12), 1631-1649.

Ivan Maddox (2014). Three Common Types of Flood Explained. The Risks of Hazard. [Online; Accessed on 2020-6-18] https://www.intermap.com/risks-of-hazard-blog/three-common-types-of-flood-explained

Jewell, T. K., & Adrian, D. D. (1981). Development of improved stormwater quality models. Journal of the Environmental Engineering Division, 107(5), 957-974.

Jha, R., Ojha, C. S., & Bhatia, K. K. (2007). Development of refined BOD and DO models for highly polluted Kali River in India. Journal of Environmental Engineering, 133(8), 839-852.

Kazemi, E., Nichols, A., Tait, S., & Shao, S. (2017). SPH modelling of depth-limited turbulent open channel flows over rough boundaries. International journal for numerical methods in fluids, 83(1), 3-27.

Koelmans, A. A., Van der Heijde, A., Knijff, L. M., & Aalderink, R. H. (2001). Integrated modelling of eutrophication and organic contaminant fate & effects in aquatic ecosystems. A review. Water Research, 35(15), 3517-3536.

Kranenburg, C. (1992). Wind-driven chaotic advection in a shallow model lake. Journal of hydraulic research, 30(1), 29-46.

Leendertse, J. J., & Gritton, E. C. (1971). A water-quality simulation model for well mixed estuaries and coastal seas: vol. II, Computation Procedures.

Liang, D., & Wu, X. (2014). A random walk simulation of scalar mixing in flows through submerged vegetations. Journal of Hydrodynamics, 26(3), 343-350.

Liang, D., Falconer, R. A., & Lin, B. (2006a). Comparison between TVD-MacCormack and ADI-type solvers of the shallow water equations. Advances in water resources, 29(12), 1833-1845.

Liang, D., Falconer, R. A., & Lin, B. (2006b). Improved numerical modelling of estuarine flows. In Proceedings of the institution of civil engineers-maritime engineering (Vol. 159, No. 1, pp. 25-35). Thomas Telford Ltd.

Liang, D., Falconer, R. A., & Lin, B. (2007). Linking one-and two-dimensional models for free surface flows. In Proceedings of the Institution of Civil Engineers-Water Management, 160: 145-151

Liang, D., Özgen, I., Hinkelmann, R., Xiao, Y., & Chen, J. M. (2015). Shallow water simulation of overland flows in idealised catchments. Environmental Earth Sciences, 74(11), 7307-7318.

Liang, D., Wang, X., Bockelmann-Evans, B. N., & Falconer, R. A. (2013). Study on nutrient distribution and interaction with sediments in a macro-tidal estuary. Advances in Water Resources, 52, 207-220.

Liang, D., Zhang, J., Li, T., & Xiao, Y. (2016). Refined seaward boundary conditions for modelling shallow water waves in semi-enclosed water bodies. Applied Ocean Research, 57, 64-77.

Lin, B., & Falconer, R. A. (1997). Three-dimensional layer-integrated modelling of estuarine flows with flooding and drying. Estuarine, coastal and shelf science, 44(6), 737-751.

Matta, E. (2018). Multi-dimensional flow and transport modeling of a surface water body in a semi-arid area: The case of the Ic-Mandantes Bay,

Northeast Brazil. Doctoral thesis, Faculty VI Planning Building Enbironment, TU Berlin, Germany.

Meselhe, E. A., & Holly Jr, F. M. (1997). Invalidity of Preissmann scheme for transcritical flow. Journal of Hydraulic Engineering, 123(7), 652-655.

Mingham, C. G., Causon, D. M., & Ingram, D. M. (2001, September). A TVD MacCormack scheme for transcritical flow. In Proceedings of the Institution of Civil Engineers-Water and Maritime Engineering , 148, no. 3 (2001), 167–175.

Murillo, J., Burguete, J., Brufau, P., & García-Navarro, P. (2005). Coupling between shallow water and solute flow equations: analysis and management of source terms in 2D. International journal for numerical methods in fluids, 49(3), 267-299.

Murillo, J., García-Navarro, P., Burguete, J., & Brufau, P. (2006). A conservative 2D model of inundation flow with solute transport over dry bed. International Journal for Numerical Methods in Fluids, 52(10), 1059-1092.

Pavan, S., Ata, R., & Hervouet, J. M. (2015). Finite volume schemes and residual distribution schemes for pollutant transport on unstructured grids. Environmental Earth Sciences, 74(11), 7337-7356.

Peaceman, D. W., & Rachford, Jr, H. H. (1955). The numerical solution of parabolic and elliptic differential equations. Journal of the Society for industrial and Applied Mathematics, 3(1), 28-41.

Phelps, E. B., & Streeter, H. W. (1958). A study of the pollution and natural purification of the Ohio River. US Department of Health, Education, & Welfare.

Pilgrim, D. H. (1976). Travel times and nonlinearity of flood runoff from tracer measurements on a small watershed. Water Resources Research, 12(3), 487-496.

Pu, J. H. (2016). Conceptual hydrodynamic-thermal mapping modelling for coral reefs at south Singapore sea. Applied Ocean Research, 55, 59-65.

Pu, J. H., Cheng, N. S., Tan, S. K., & Shao, S. (2012). Source term treatment of SWEs using surface gradient upwind method. Journal of hydraulic research, 50(2), 145-153.

Pu, J. H., Huang, Y., Shao, S., & Hussain, K. (2016). Three-Gorges Dam fine sediment pollutant transport: turbulence SPH model simulation of multi-fluid flows.

Rajar, R. (1997). The role of mathematical models, physical models and field measurements in water pollution problems (Vol. 20). WIT Press.

Reynolds, O. (1895). IV. On the dynamical theory of incompressible viscous fluids and the determination of the criterion. Philosophical transactions of the royal society of london.(a.), (186), 123-164.

Roseveare, N., & Trapmore, G. (2008). The sustainable regeneration of Boscastle. In BHS 10th National Hydrology Symposium, Exeter.

Schindler, D. W. (2006). Recent advances in the understanding and management of eutrophication. Limnology and oceanography, 51(1part2), 356-363.

Simons, F. (2020). A robust high-resolution hydrodynamic numerical model for surface water flow and transport processes within a flexible software framework. Doctoral thesis, Faculty VI Planning Building Environment, TU Berlin, Germany.

Sincock, A. M., & Lees, M. J. (2002). Extension of the QUASAR River-Water Quality Model to Unsteady Flow Conditions. Water and Environment Journal, 16(1), 12-17.

Song, L., Zhou, J., Guo, J., Zou, Q., & Liu, Y. (2011). A robust well-balanced finite volume model for shallow water flows with wetting and drying over irregular terrain. Advances in Water Resources, 34(7), 915-932.

Taylor, G. I. (1922). Diffusion by continuous movements. Proceedings of the london mathematical society, 2(1), 196-212.

Toro, E. F. (2001). Shock-capturing methods for free-surface shallow flows. John Wiley & Sons Ltd., Chichester, England.

Tseng, M. H. (2004). Improved treatment of source terms in TVD scheme for shallow water equations. Advances in water resources, 27(6), 617-629.

Tuckley, C. (2010). Study of a Flash Flood Event (MEng thesis). University of Cambridge, UK.

Vázquez, R. F., Feyen, L., Feyen, J., & Refsgaard, J. C. (2002). Effect of grid size on effective parameters and model performance of the MIKE-SHE code. Hydrological processes, 16(2), 355-372.

Waldman, S., Baston, S., Nemalidinne, R., Chatzirodou, A., Venugopal, V., & Side, J. (2017). Implementation of tidal turbines in MIKE 3 and Delft3D models of Pentland Firth & Orkney Waters. Ocean & Coastal Management, 147, 21-36.

Wang, J., Liang, D., Zhang, J., & Xiao, Y. (2016). Comparison between shallow water and Boussinesq models for predicting cascading dam-break flows. Natural Hazards, 83(1), 327-343.

Wang, Q., Li, S., Jia, P., Qi, C., & Ding, F. (2013). A review of surface water quality models. The Scientific World Journal, 2013.

WHO (2020). Water-related diseases. [Online; Accessed on 2020-06-09]. https://www.who.int/water_sanitation_health/diseases-risks/diseases/diarrhoea/en

World Bank (2017a). Water Resources Management. [Online; Accessed on 2020-5-17]. https://www.worldbank.org/en/topic/waterresourcesmanagement

World Bank (2017b). Water Supply. [Online; Accessed on 2020-5-17]. https://www.worldbank.org/en/topic/watersupply

Wu, X. F., & Liang, D. (2019). Study of pollutant transport in depth-averaged flows using random walk method. Journal of Hydrodynamics, 31(2), 303-316.

Wu, X. F., Yang, F., & Liang, D. F. (2018). Study of pollutant transport in environmental flows using depth-averaged random walk method. EPiC Series in Engineering, 3, 2342-2350.

Wu, X., Liang, D., & Zhang, G. (2019). Estimating the accuracy of the random walk simulation of mass transport processes. Water research, 162, 339-346.

Yang, F., Liang, D., & Xiao, Y. (2018). Influence of Boussinesq coefficient on depth-averaged modelling of rapid flows. Journal of Hydrology, 559, 909-919.

Yang, F., Liang, D., Wu, X., & Xiao, Y. (2020). On the application of the depth-averaged random walk method to solute transport simulations. Journal of Hydroinformatics, 22(1), 33-45.

Yuan, D. (2007). Development of an integrated hydro-environmental model and its application to a macro-tidal estuary. PhD thesis, Cardiff University.

Zeng, X., Gualtieri, C., Liu, H., & Shao, D. (2021). Environmental Hydraulics in the new millennium: Historical evolution and recent research trends. Water, 13(8), 1021.

Zhang, Z., & Chen, Q. (2007). Comparison of the Eulerian and Lagrangian methods for predicting particle transport in enclosed spaces. Atmospheric environment, 41(25), 5236-5248.

Zheng, X., Shao, S., Khayyer, A., Duan, W., Ma, Q., & Liao, K. (2017). Corrected first-order derivative ISPH in water wave simulations. Coastal Engineering Journal, 59(01), 1750010.

Zoppou, C. (2001). Review of urban storm water models. Environmental Modelling & Software, 16(3), 195-231.